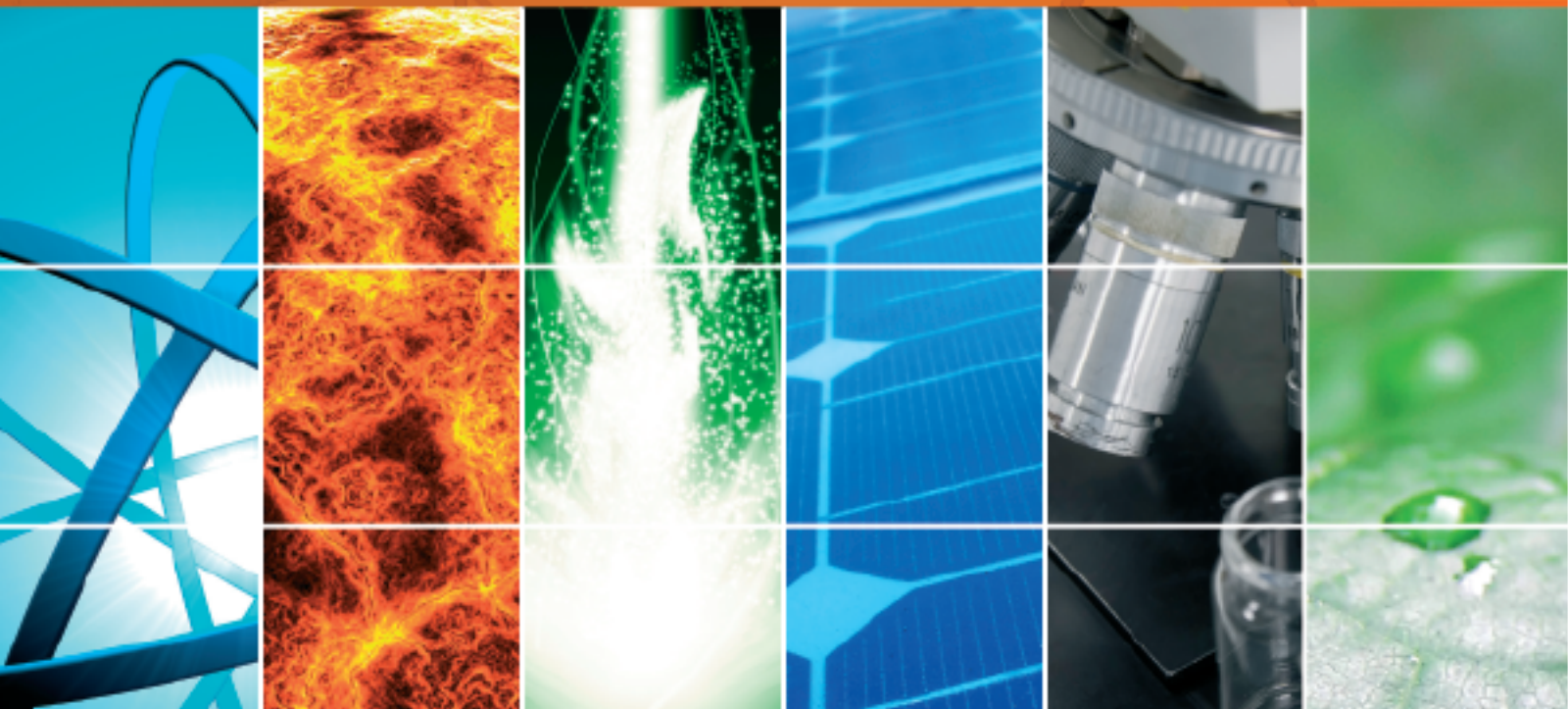


New Energy Materials and Device Application

Guest Editors: Sheng-Po Chang, Jun Zhu, Shyh-Jer Huang,
Hsin-Chieh Yu, Ting-Jen Hsueh, and Hsin-Ying Lee





New Energy Materials and Device Application

International Journal of Photoenergy

New Energy Materials and Device Application

Guest Editors: Sheng-Po Chang, Jun Zhu, Shyh-Jer Huang,
Hsin-Chieh Yu, Ting-Jen Hsueh, and Hsin-Ying Lee



Copyright © 2015 Hindawi Publishing Corporation. All rights reserved.

This is a special issue published in "International Journal of Photoenergy." All articles are open access articles distributed under the Creative Commons Attribution License, which permits unrestricted use, distribution, and reproduction in any medium, provided the original work is properly cited.

Editorial Board

- M. S. A. Abdel-Mottaleb, Egypt
Xavier Allonas, France
Nicolas Alonso-Vante, France
Wayne A. Anderson, USA
Yanhui Ao, China
Raja S. Ashraf, UK
Vincenzo Augugliaro, Italy
Detlef W. Bahnemann, Germany
Ignazio Renato Bellobono, Italy
Raghu N. Bhattacharya, USA
Thomas M. Brown, Italy
Stephan Buecheler, Switzerland
Gion Calzaferri, Switzerland
Chungheng Chen, China
Sung Oh Cho, Republic of Korea
Věra Cimrová, Czech Republic
Juan M. Coronado, Spain
Ying Dai, China
Dionysios D. Dionysiou, USA
Abderrazek Douhal, Spain
Mahmoud M. El-Nahass, Egypt
Polycarpos Falaras, Greece
Chris Ferekides, USA
Paolo Fornasiero, Italy
Hermenegildo García, Spain
Germà Garcia-Belmonte, Spain
Elisa Isabel Garcia-Lopez, Italy
Beverley Glass, Australia
Mohammed A. Gondal, KSA
Anthony M. Harriman, UK
Jr-Hau He, Taiwan
Shinya Higashimoto, Japan
Wing-Kei Ho, Hong Kong
Cheuk-Lam Ho, Hong Kong
Fuqiang Huang, China
Jürgen Hüpkes, Germany
Adel A. Ismail, Egypt
Chun-Sheng Jiang, USA
Misook Kang, Republic of Korea
Shahed Khan, USA
Sun-Jae Kim, Korea
Jong Hak Kim, Korea
Sungjee Kim, Korea
Fernando Langa, Spain
Cooper H. Langford, Canada
Tae-Woo Lee, Korea
Lecheng Lei, China
Zhaosheng Li, China
Xinjun Li, China
Stefan Lis, Poland
Vittorio Loddo, Italy
Gongxuan Lu, China
Dongge Ma, China
Nai Ki Mak, Hong Kong
Rajaram S. Mane, India
Dionissios Mantzavinos, Greece
Ugo Mazzucato, Italy
Sheng Meng, China
Jacek Miller, Poland
Claudio Minero, Italy
Thomas Moehl, Switzerland
Antoni Morawski, Poland
Franca Morazzoni, Italy
Fabrice Morlet-Savary, France
Mohammad Muneer, India
Kun Na, Korea
Ebinazar B. Namdas, Australia
Maria da Graça P. Neves, Portugal
Tebello Nyokong, South Africa
Tsuyoshi Ochiai, Japan
Kei Ohkubo, Japan
Haridas Pal, India
Leonidas Palilis, Greece
Leonardo Palmisano, Italy
Ravindra K. Pandey, USA
Hyunwoong Park, Korea
Thierry Pauporté, France
Pierre Pichat, France
Gianluca Li Puma, UK
Tijana Rajh, USA
Peter Robertson, UK
Avigdor Scherz, Israel
Elena Selli, Italy
Ganesh D. Sharma, India
Jinn Kong Sheu, Taiwan
Panagiotis Smirniotis, USA
Bhushan Sopori, USA
Zofia Stasicka, Poland
Elias Stathatos, Greece
Jegadesan Subbiah, Australia
Meenakshisundaram Swaminathan, India
Kazuhiro Takanabe, KSA
Mohamad-Ali Tehfe, Canada
K. R. Justin Thomas, India
Yang Tian, China
Nikolai V. Tkachenko, Finland
Ahmad Umar, KSA
Thomas Unold, Germany
Veronica Vaida, USA
Roel van De Krol, Germany
Mark van Der Auweraer, Belgium
Rienk Van Grondelle, Netherlands
Wilfried Van Sark, Netherlands
Sergey Varlamov, Australia
Sheng Wang, China
Mingkui Wang, China
Xuxu Wang, China
David Worrall, UK
Jeffrey C. S. Wu, Taiwan
Yanfa Yan, USA
Jiannian Yao, China
Minjoong Yoon, Korea
Hongtao Yu, USA
Ying Yu, China
Jiangbo Yu, USA
Klaas Zachariasse, Germany
Juan Antonio Zapien, Hong Kong
Tianyou Zhai, China
Yong Zhou, China
Guijiang Zhou, China
Rui Zhu, China

Contents

New Energy Materials and Device Application, Sheng-Po Chang, Jun Zhu, Shyh-Jer Huang, Hsin-Chieh Yu, Ting-Jen Hsueh, and Hsin-Ying Lee
Volume 2015, Article ID 657152, 1 page

Superior Photocurrent of Quantum Dot Sensitized Solar Cells Based on PbS : In/CdS Quantum Dots, Zongbo Huang and Xiaoping Zou
Volume 2015, Article ID 657871, 9 pages

Investigating the Effect of Piezoelectric Polarization on GaN-Based LEDs with Different Prestrain Layer by Temperature-Dependent Electroluminescence, C. K. Wang, Y. Z. Chiou, T. H. Chiang, and T. K. Lin
Volume 2015, Article ID 135321, 6 pages

Hydrothermal Growth of Quasi-Monocrystal ZnO Thin Films and Their Application in Ultraviolet Photodetectors, Yung-Chun Tu, Shui-Jinn Wang, Tseng-Hsing Lin, Chien-Hsiung Hung, Tsung-Che Tsai, Ru-Wen Wu, Kai-Ming Uang, and Tron-Min Chen
Volume 2015, Article ID 261372, 7 pages

Scalability of Phase Change Materials in Nanostructure Template, Wei Zhang, Biyun L. Jackson, Ke Sun, Jae Young Lee, Shyh-Jer Huang, Hsin-Chieh Yu, Sheng-Po Chang, Shoou-Jinn Chang, and Ya-Hong Xie
Volume 2015, Article ID 253296, 4 pages

An Accurate Thermoviscoelastic Rheological Model for Ethylene Vinyl Acetate Based on Fractional Calculus, Marco Paggi and Alberto Sapora
Volume 2015, Article ID 252740, 7 pages

Optical Properties of Indium Doped ZnO Nanowires, Tsung-Shine Ko, Sin-Liang Ou, Kuo-Sheng Kao, Tz-Min Yang, and Der-Yuh Lin
Volume 2015, Article ID 760376, 6 pages

Improving Crystalline Silicon Solar Cell Efficiency Using Graded-Refractive-Index SiON/ZnO Nanostructures, Yung-Chun Tu, Shui-Jinn Wang, Chien-Hung Wu, Kow-Ming Chang, Tseng-Hsing Lin, Chien-Hsiung Hung, and Jhen-Siang Wu
Volume 2015, Article ID 275697, 6 pages

Optoelectric Properties of GaInP p-i-n Solar Cells with Different i-Layer Thicknesses, Tsung-Shine Ko, Der-Yuh Lin, You-Chi He, Chen-Chia Kao, Bo-Yuan Hu, Ray-Hua Horng, Fan-Lei Wu, Chih-Hung Wu, and Yu-Li Tsai
Volume 2015, Article ID 703045, 7 pages

Plasmon-Enhanced Photoluminescence of an Amorphous Silicon Quantum Dot Light-Emitting Device by Localized Surface Plasmon Polaritons in Ag/SiO_x:a-Si QDs/Ag Sandwich Nanostructures, Tsung-Han Tsai, Ming-Yi Lin, Wing-Kit Choi, and Hoang Yan Lin
Volume 2015, Article ID 140617, 6 pages

Fabrication of Hybrid Organic Photovoltaic Devices Using Electrostatic Spray Method, Zhe-Wei Chiu, Yu-Jen Hsiao, Te-Hua Fang, and Liang-Wen Ji
Volume 2014, Article ID 861587, 5 pages

Using Pre-TMIn Treatment to Improve the Optical Properties of Green Light Emitting Diodes, Bing Xu, Hai Tao Dai, Shu Guo Wang, Fu-Chuan Chu, Chou-Hsiung Huang, Sheng-Fu Yu, Jun Liang Zhao, Xiao Wei Sun, and Ray-Ming Lin
Volume 2014, Article ID 952567, 6 pages

Editorial

New Energy Materials and Device Application

**Sheng-Po Chang,¹ Jun Zhu,² Shyh-Jer Huang,^{3,4} Hsin-Chieh Yu,⁴
Ting-Jen Hsueh,⁵ and Hsin-Ying Lee⁶**

¹*Department of Electrical Engineering and Institute of Microelectronics, Center for Micro/Nano Science and Technology and Advanced Optoelectronic Technology Center, National Cheng Kung University, Tainan 701, Taiwan*

²*College of Physics Science and Technology, Yangzhou University, Yangzhou, Jiangsu 225009, China*

³*Department of Electrical Engineering, University of California, Los Angeles, CA 90095, USA*

⁴*Advanced Optoelectronic Technology Center, National Cheng Kung University, Tainan 701, Taiwan*

⁵*National Nano Device Laboratories, Southern Taiwan Science Park, Tainan 701, Taiwan*

⁶*Department of Photonics, National Cheng Kung University, Tainan 701, Taiwan*

Correspondence should be addressed to Sheng-Po Chang; changsp@mail.ncku.edu.tw

Received 26 May 2015; Accepted 27 May 2015

Copyright © 2015 Sheng-Po Chang et al. This is an open access article distributed under the Creative Commons Attribution License, which permits unrestricted use, distribution, and reproduction in any medium, provided the original work is properly cited.

In the 21st century, aggravating energy and environmental problems such as pollution, fossil fuel depletion, and global warming are ringing the alarm bell to human society. Therefore, clean and renewable energy materials as well as their devices are urgently demanded, which are the key and foundation to realize the transformation and utilization of new energy. The developments of energy storage and conversion techniques strongly depend on the achievements of material science.

Based on the modern instruments of making and analyzing novel materials for green energy and rapid accumulation of knowledge about them, researchers nowadays stand at a point that could be rich in huge opportunities to exterminate the energy and environmental problems. Indeed, we have seen a lot of progress in utilization of green energy, such as photovoltaic devices, bioenergy, and wind-driven power. Besides using green energy, the light-emitting devices also rock the lighting market by their capability of saving energy. However, the achievements are still far below the demands, and colleagues are making efforts in these fields.

This special issue selects 11 papers about energy materials, organic photovoltaic device, photodetector, thin-film solar cells, light-emitting device, and other energy saving and high energy efficiency related topics. This special issue enables

interdisciplinary collaboration between science and engineering technologists in the academic and industrial fields. The objective is to provide an opportunity for interdisciplinary researchers to share their latest research achievements and let the potential readers learn some insightful concepts in energy related research. We hope this research progress can inspire more advanced ideas for the future development of energy technology.

*Sheng-Po Chang
Jun Zhu
Shyh-Jer Huang
Hsin-Chieh Yu
Ting-Jen Hsueh
Hsin-Ying Lee*

Research Article

Superior Photocurrent of Quantum Dot Sensitized Solar Cells Based on PbS:In/CdS Quantum Dots

Zongbo Huang and Xiaoping Zou

Research Center for Sensor Technology, Beijing Key Laboratory for Sensor, Ministry of Education Key Laboratory for Modern Measurement and Control Technology, School of Applied Sciences, Beijing Information Science and Technology University, Jianxiangqiao Campus, Beijing 100101, China

Correspondence should be addressed to Xiaoping Zou; xpzou2005@gmail.com

Received 6 May 2014; Revised 17 July 2014; Accepted 25 July 2014

Academic Editor: Hsin-Ying Lee

Copyright © 2015 Z. Huang and X. Zou. This is an open access article distributed under the Creative Commons Attribution License, which permits unrestricted use, distribution, and reproduction in any medium, provided the original work is properly cited.

PbS:In and CdS quantum dots (QDs) are sequentially assembled onto a nanocrystalline TiO₂ film to prepare a PbS:In/CdS cosensitized photoelectrode for QD sensitized solar cells (QDSCs). The results show that PbS:In/CdS QDs have exhibited a significant effect in the light harvest and performance of the QDSC. In the cascade structure of the electrode, the reorganization of energy levels between PbS and TiO₂ forms a stepwise structure of band-edge levels which is advantageous to the electron injection into TiO₂. Energy conversion efficiency of 2.3% is achieved with the doped electrode, under the illumination of one sun (AM1.5, 100 mW cm⁻²). Besides, a remarkable short circuit current density (up to 23 mA·cm⁻²) is achieved in the resulting PbS:In/CdS quantum dot sensitized solar cell, and the related mechanism is discussed.

1. Introduction

One of the current challenges for high performance sensitized solar cells is the limited light absorption range from the visible to the near-infrared (NIR) region for the solar spectrum [1]. Generally, molecular dyes can only absorb light photons within a more or less broadband corresponding to their molecular transitions; thus the absorption region of dye sensitized solar cells (DSCs) is limited [2]. On the other hand, semiconductor materials can absorb all photons with energies higher than their band gap, E_g . The quantum dot sensitized solar cells (QDSCs) are attracting increasing attention as they show promising potential for the development of next generation solar cells with high photocurrent [3–5].

Recently, various quantum dots (QDs), such as CdS, CdSe, PbS, PbSe, and InP, have been attempted to fabricate QDSCs [6–10]. PbS ($E_g = 0.41$ eV) [11], specifically, has attracted increasing interest in sensitizers for achieving superior photocurrent solar cells. Recent work by Zhou et al. has demonstrated a high photocurrent density (J_{SC} , nearly 20 mA·cm⁻²) in the PbS/CdS cosensitized solar cells [12]. However, compared to that of TiO₂, the conduction band

(CB) of PbS is located at lower energy [13]. The situation is not conducive to electronic transmission from PbS to TiO₂. Thus, optimization of the structure for photoanode is highly required to improve the electron injection in PbS QDSCs [14].

High performance deep red and NIR emitters are much needed for developing desirable probes for *in vivo* diagnostics and optical devices application [15–17]. Synthesis of doped semiconductor nanocrystal QDs [18–20] has recently become an active subject in the field of nanomaterials because of their unique optical, electronic, and physical properties [21]. Various advantages have been achieved by doping with optically active transition metal ions (such as Cu, In, Mn, and Mg) [22, 23] because the electrical and optical properties of QDs could be effectively improved. In addition, the photophysical properties of semiconductor nanocrystals could also be adjusted by different types and concentrations of dopants [24]. The dopant creates electronic states in the midgap region of the QD, thus altering the charge separation and recombination dynamics. Currently, other efforts to design In-doped ZnSe, Mn-doped ZnSe, and In-doped-InP QDs have brought a bright perspective for developing highly efficient and color-tunable emitters in the red and NIR window [19, 25, 26].

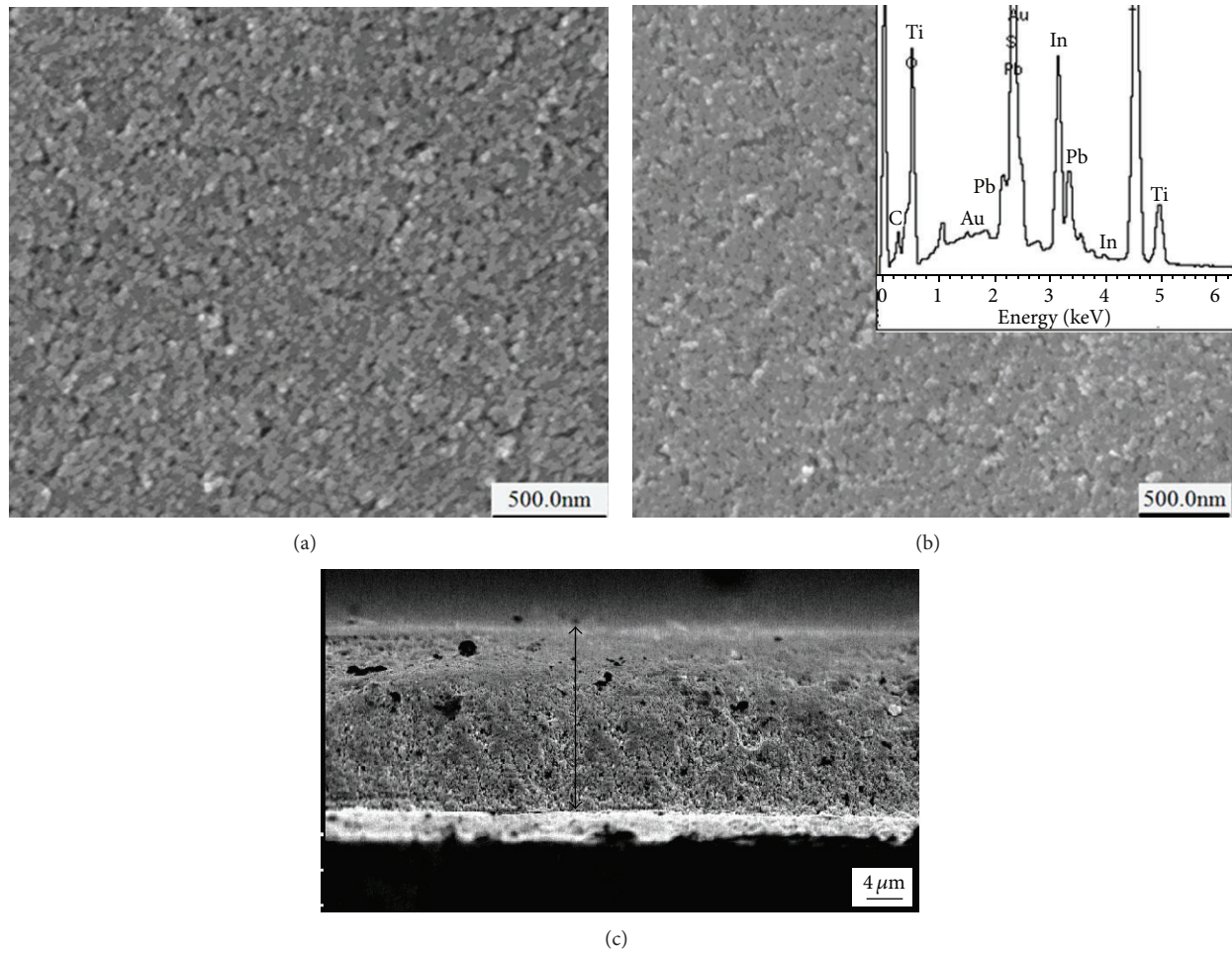


FIGURE 2: SEM images of the top view for the nanocrystalline TiO_2 film (a) and TiO_2 deposited by PbS:In film (b); the cross-section view of the TiO_2 deposited by PbS:In film (c); the inset in parts (b) shows the corresponding EDS spectra.

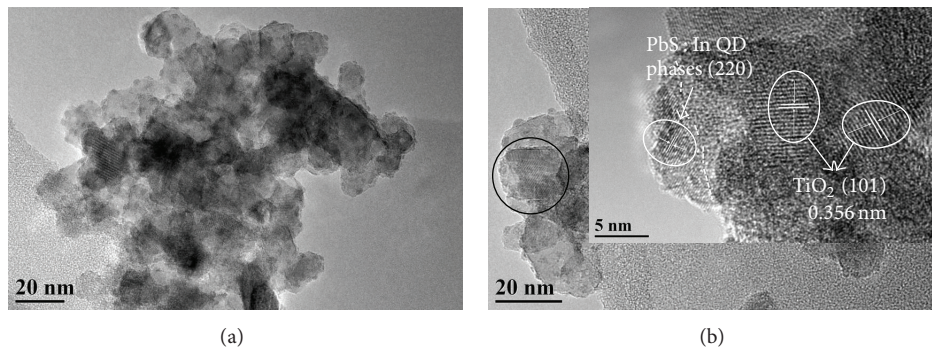


FIGURE 3: (a) and (b) are low-magnification HRTEM images of the PbS:In film. The inset in parts (b) shows the corresponding high-magnification HRTEM image.

lead to the change of the crystalline structure of PbS, which indicates the formation of In in the as-prepared samples.

Figure 5(a) shows the UV-vis absorption spectra of PbS:In QDs look red-shifted compared to the pristine PbS, especially in visible region. Optical band gap of the QDs is estimated from UV-vis absorption spectra using Kubelka-Munk equation [32] and Tauc plot [33] (Figure 5(b)). The optical band gap of PbS:In QD increases from 1.0 eV to 1.4 eV

as the doping concentration increases from 0 to 1:1. However, the threshold for the PbS doped with In (PbS:In = 1:1, 5:1) in the NIR region in inset of Figure 5(a) is moved to shorter wavelength than the pristine PbS, which is consistent with the increase in band gap.

Furthermore, the PbS:In QD adsorbed TiO_2 of low binding energy was observed by ultraviolet photoelectron spectroscopy (UPS) spectra. Secondary cut-off is fitted to

TABLE 1: Parameters of photovoltaic performance of the QDSCs with different concentrations of PbS: In.

Sample	$J_{SC}/\text{mA cm}^{-2}$	V_{OC}/V	FF	η (%)
Pb: In = 1:1	5.07	0.39	0.36	0.71
Pb: In = 5:1	16.94	0.44	0.22	1.64
Pb: In = 10:1	19.11	0.42	0.27	2.17
Pb: In = 20:1	15.31	0.41	0.22	1.38

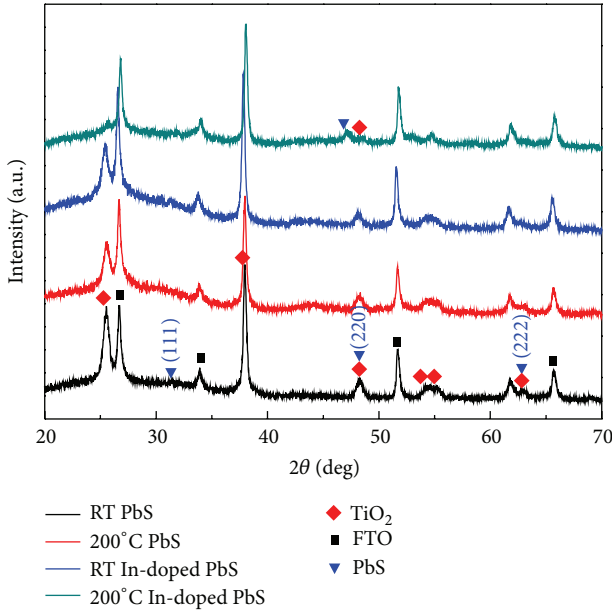


FIGURE 4: The XRD patterns of PbS and PbS:In films at room temperature and 200°C.

energy of He I light source (21.2 eV), where measurement of low energy region corresponds to potential energy of valence band maximum (VBM) from the vacuum level, as shown in Figure 5(c). The position of conduction band minimum (CBM) can be calculated based on VBM and optical band gap energy. Band-edge alignment is demonstrated in Figure 5(d), where CBM of the QDs moves upward as the concentration decreases from 0 to 10:1 and moves downgrade as the concentration decreases from 10:1 to 20:1. It is indicated that CBM is slightly altered by In concentration. So it is likely to shape a stepwise structure of between PbS and TiO_2 band-edge levels which is advantageous to the electron injection into TiO_2 , as shown in Figure 5(e).

The J - V characteristics with different In-doped concentrations for 2 SILAR cycles of PbS:In and 4 SILAR cycles of CdS solar cell are shown in Figure 6. The short circuit current density (J_{SC}), the open circuit voltage (V_{OC}), the fill factor (FF), and the power conversion efficiency (η %) are shown in Table 1, respectively. Obviously, the best performance of the doped solar cell is achieved based on the (Pb:In) concentration ratio (10:1). An inductively coupled plasma optical emission spectroscopy (ICP-OES) was performed to determine the actual In-doped concentration. The results suggest the concentration was 1.6% in the PbS film. Either higher or lower In-doped concentration might damage the

performance of QDSCs. The optimal concentration was found to be 10:1 to form a cascade structure for the electronic transmission. The implication of experimental data suggested that V_{OC} enhanced the increase of the doping concentration.

Similarly, the doped system with different SILAR cycles of CdS is completed. The normalized absorption spectra of these electrodes are shown in Figure 7(a). Absorption around 550 nm was found in the diffusion reflectance absorbance spectra of PbS:In/CdS deposited film, demonstrating enhanced ability for capturing incident photons with the increasing of the CdS layer. The J - V characteristics well correspond to the diffusion reflectance absorbance spectra shown in Figure 7(b). The 6 SILAR cycles of short circuit current density ($\sim 23.42 \text{ mA}\cdot\text{cm}^{-2}$) are higher than other cycles. The highest efficiency (2.36%) is obtained with the 6 SILAR cycles of CdS layer (Table 2). The addition of SILAR cycle of CdS can reduce the recombination and enhancement V_{OC} in the cell is observed in Table 2.

For the comparative study, two different types of semiconductor photoanodes were prepared: (i) 2 SILAR cycles of undoped PbS and 6 SILAR cycles of CdS and (ii) 2 SILAR cycles of PbS:In (Pb:In = 10:1) and 6 SILAR cycles of CdS. The normalized absorption spectra of these electrodes are shown in Figure 8(a). Absorption around 1200 nm was observed in the absorption spectra of PbS:In/CdS deposited film, demonstrating enhanced ability for capturing incident photons.

Figure 8(b) shows incident photon-to-electron conversion efficiency (IPCE) spectra of the doped and undoped QDSCs at different incident light wavelengths. Compared to the PbS/CdS ones, much more increment in overall photocurrent response, specifically in the NIR region, was found in the PbS:In/CdS electrodes, showing maximum IPCE greater than 70%. Light scattering layer increases further IPCE at longer wavelength (IPCE of 40% at 800 nm and 10% at 1200 nm). The broad absorption in the visible and higher photoconversion efficiency highlights the importance of In doping of the metal chalcogenide films. Very recently, the highest short circuit current density with a maximum EQE (74.6% at 470 nm) of PbS:Hg QD sensitized solar cell was demonstrated to change it [28]. We can refer it to some references [34–39]. It is indicated that short circuit photocurrent density has a stronger relevance with working electrode absorb light range than value of IPCE.

The J - V characteristics of these two QDSCs are presented in Figure 8(c). Surprisingly, PbS:In/CdS films that exhibited a significant increment close to 50% (from $15.73 \text{ mA}\cdot\text{cm}^{-2}$ to $23.01 \text{ mA}\cdot\text{cm}^{-2}$) in the photocurrent are shown in Table 3, compared to the corresponding undoped films. Similarly, the open circuit voltage was found to dramatically increase from 0.35 V to 0.39 V after doping. Although the fill factor still remained at very low level, the increase in the short circuit current and the open circuit voltage with In-doped system leads to the enhancement in the overall power conversion efficiency, suggesting higher efficiency of 2.30% based on the undoped one (1.38%).

The enhanced performance of PbS:In/CdS films is mainly attributed to the CBM and VBM realignment by In

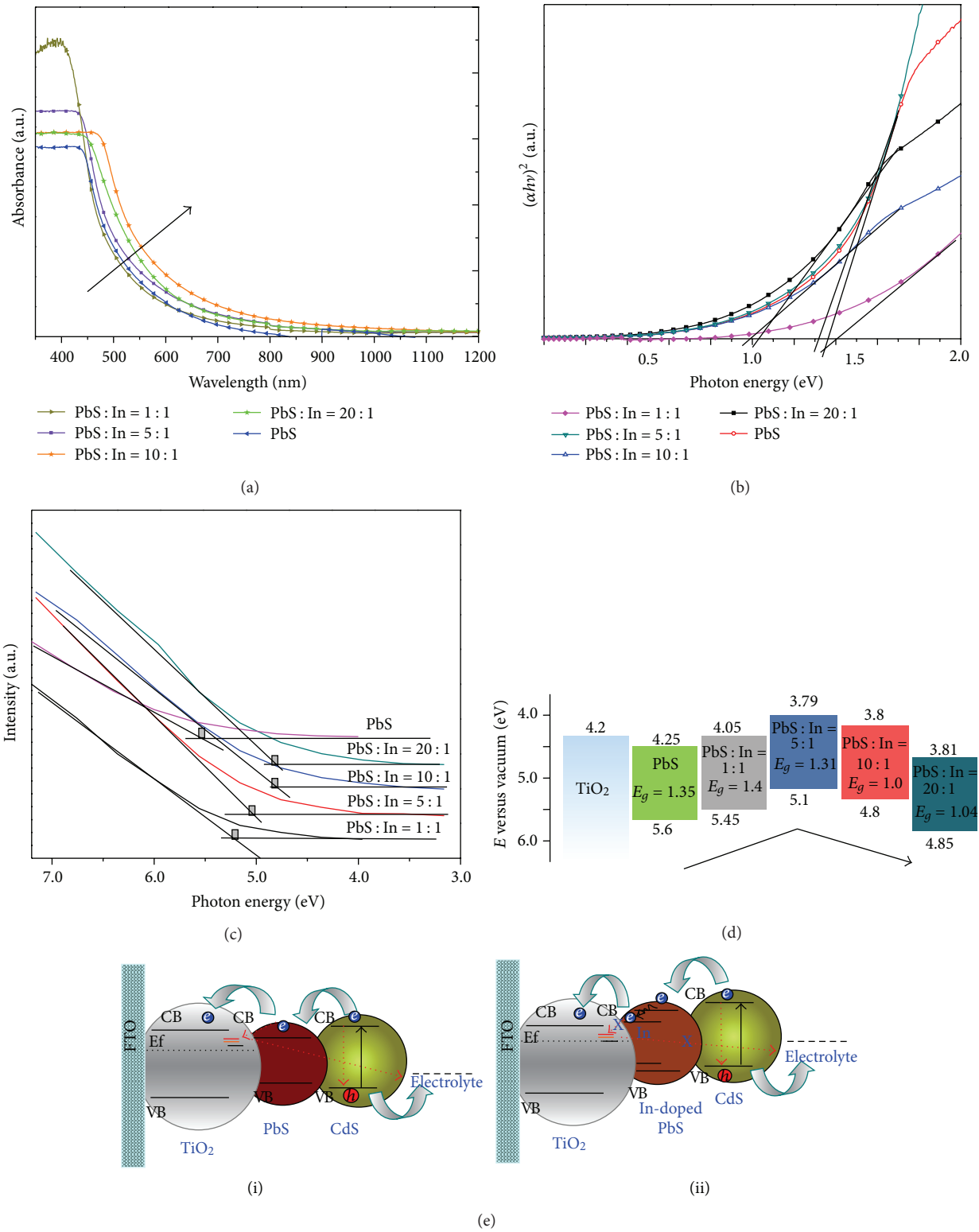


FIGURE 5: (a) UV-vis absorption spectra of PbS:In QD (PbS:In = 0, 1:1, 5:1, 10:1, and 20:1) adsorbed TiO₂ and (b) Tauc plot calculated by using Kubelka-Munk equation from UV-vis absorption; (c) UPS spectra of PbS:In QD (PbS:In = 0, 1:1, 5:1, 10:1, and 20:1) adsorbed TiO₂ and extrapolation of low binding energy region. (d) Band-edge alignment diagram for PbS and PbS:In QDs. (e) Schematic illustration of the electron and hole transfer model for undoped PbS/CdS (i) and PbS:In/CdS (ii).

TABLE 2: Parameters of photovoltaic performance of the QDSCs with different SILAR cycles of CdS.

Sample	$J_{SC}/\text{mA}\cdot\text{cm}^{-2}$	V_{OC}/V	FF	η (%)
(Pb : In = 10 : 1) PbS : In(2)/CdS(4)	19.41	0.42	0.22	1.95
(Pb : In = 10 : 1) PbS : In(2)/CdS(6)	23.42	0.44	0.23	2.36
(Pb : In = 10 : 1) PbS : In(2)/CdS(8)	20.21	0.46	0.23	2.18

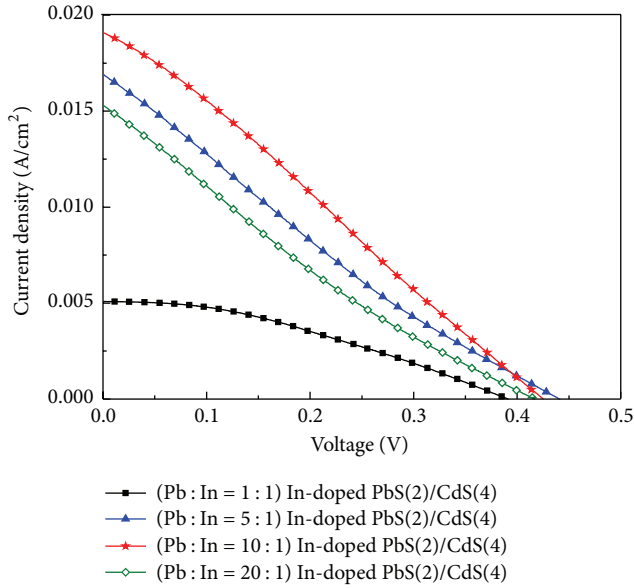
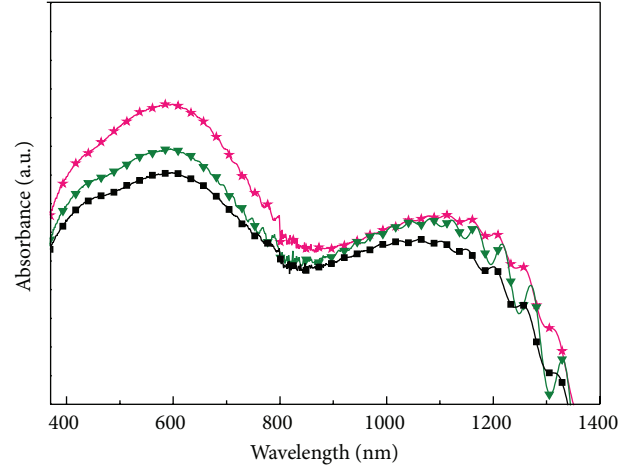
FIGURE 6: The J - V characteristics with different concentrations of PbS:In sensitized solar cell: Pb:In = 1:1 (■), Pb:In = 5:1 (▲), Pb:In = 10:1 (★), and Pb:In = 20:1 (◇).

TABLE 3: Parameters of photovoltaic performance of PbS/CdS and PbS : In/CdS QDSCs.

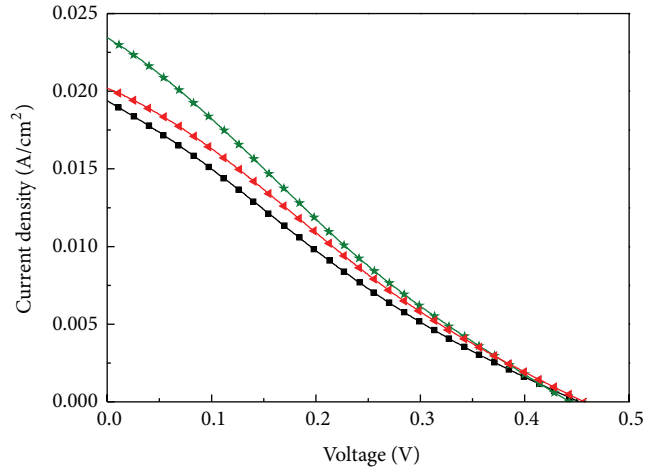
Sample	$J_{SC}/\text{mA}\cdot\text{cm}^{-2}$	V_{OC}/V	FF	η (%)
PbS/CdS	15.73	0.35	0.25	1.38
PbS : In/CdS	23.01	0.40	0.26	2.30

doping, which effectively separate the electrons and holes into QD layers. The cascade structure of $\text{TiO}_2/\text{PbS}:\text{In}/\text{CdS}$ is similar to that of Hg- and Cu-doped system [26, 28], as shown in Figure 5(e)(ii). The transmission path is advantageous to the accumulation of more electrons for increasing photovoltage and short circuit current density of QDSCs. Besides, the energy gap of PbS is maintained, which benefits multiexciton generation.

Through the impedance measurement we can also confirm the above conclusions. Impedance measurement of the QDSCs based on $\text{TiO}_2/\text{PbS}/\text{CdS}$ and $\text{TiO}_2/\text{PbS}:\text{In}/\text{CdS}$ photoelectrodes is presented in Figure 8(d). Equivalent circuit in the insert has been suggested in another sentence [37–39] to model the impedance spectrum (IS) of QDSCs. According to the equivalent circuit, two semicircles should be obtained in each IS. The recombination resistance (R_{rec} , a charge-transfer resistance related to recombination of electrons at the $\text{TiO}_2/\text{electrolyte}$ interface) of the doped system is much



(a)



(b)

FIGURE 7: The diffusion reflectance absorbance spectra (a) and J - V characteristics (b) with different working electrodes based on SILAR cycles of CdS layer: CdS(4) (■), CdS(6) (▼), and CdS(8) (★).

higher than undoped system. Besides, R_{rec} is inversely proportional to both the recombination rate and the density of electrons in TiO_2 , which could partially account for the longer electron lifetime and higher photocurrent in $\text{TiO}_2/\text{PbS}:\text{In}/\text{CdS}$ photoelectrode.

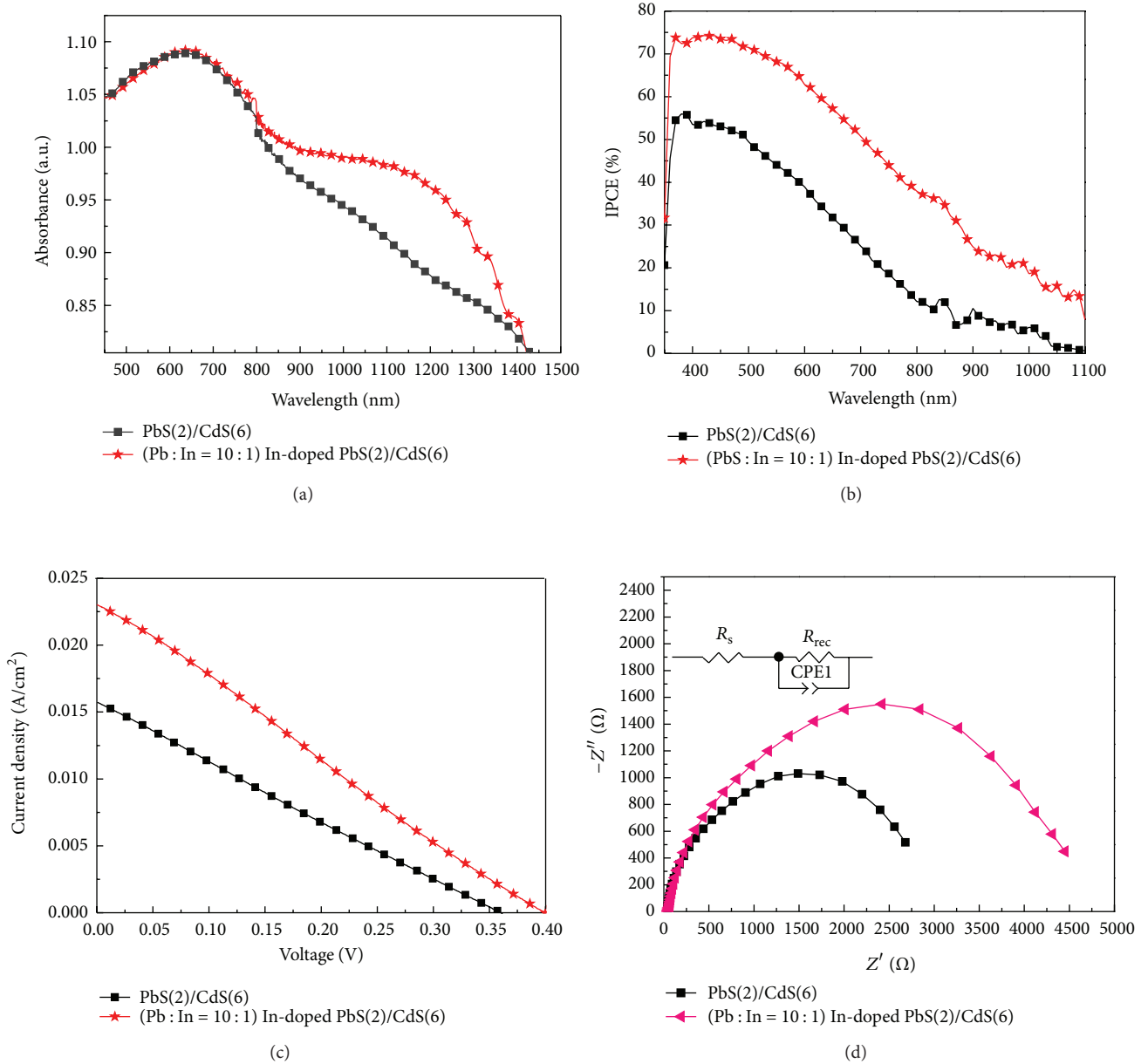


FIGURE 8: (a) Diffusion reflectance absorbance spectra of semiconductor films deposited on mesoporous TiO_2 films: PbS/CdS (■), PbS:In/CdS (★). (b) IPCE spectra for PbS/CdS (■), PbS:In/CdS (★). (c) J - V characteristics of different working electrodes measured under AM 1.5 global filter of 100 mW cm^{-2} sunlight: undoped PbS/CdS (■), PbS:In/CdS (★). (d) Impedance measurement of QDSCs: undoped PbS/CdS (■), PbS:In/CdS (▲) at an applied negative bias, $V_{\text{appl}} = -0.4 \text{ V}$, under dark conditions. The working electrodes areas were both at 0.09 cm^2 .

However, there are still several factors limiting the power conversion efficiency in QDSCs. (i) The Pt counterelectrode has poorer performance in the improvement of the fill factor for the QDSCs, comparing to other counterelectrodes [39, 40]. (ii) Good photoanode and bad counterelectrode do not match each other, against electrolytic oxidation reduction [28]. (iii) Difficulties have been also found in the SILAR method for controlling the QD size and size distribution, optimizing QD sensitized electrode structure, high coverage, and band alignment of QDs, thus slowing electron injection into TiO_2 and hole transfer into sulfide redox couples. The high charge recombination is severe factor in achieving

higher efficiency of QDSCs [41]. However, the *in situ* electrochemistry deposition method has been found to be an effective approach to ensure high surface coverage of TiO_2 and direct attachment between QDs and TiO_2 matrix [42], demonstrating a platform for fabricating high performance solar cells via doping systems.

4. Conclusions

In summary, SILAR method was used to fabricate PbS:In QDSCs. A superior short circuit current density up to 23 mA cm^{-2} was achieved in the resulting cells with doped

QDs, mainly attributed to the separation of electrons and holes and charge transfer improvement. The results demonstrate a promising potential method for fabricating high performance QDSCs.

Conflict of Interests

The authors declare that there is no conflict of interests regarding the publication of this paper.

Acknowledgments

This work was partially supported by Key Project of Beijing Natural Science Foundation (3131001), Key Project of Natural Science Foundation of China (91233201 and 61376057), Key Project of Beijing Education Committee Science & Technology Plan (KZ201211232040), State 863 Plan of MOST of China (2011AA050527), Beijing National Laboratory for Molecular Sciences (BNLMS2012-21), State Key Laboratory of Solid State Microstructures of Nanjing University (M27019), State Key Laboratory for New Ceramic and Fine Processing of Tsinghua University (KF1210), Key Laboratory for Renewable Energy and Gas Hydrate of Chinese Academy of Sciences (y207kal001), Beijing Key Laboratory for Sensors of BISTU (KF20141077207 and KF20141077208), and Beijing Key Laboratory for photoelectrical measurement of BISTU (GDKF2013005).

References

- [1] A. Braga, S. Giménez, I. Concina, A. Vomiero, and I. Mora-Seró, "Panchromatic sensitized solar cells based on metal sulfide quantum dots grown directly on nanostructured TiO₂ electrodes," *Journal of Physical Chemistry Letters*, vol. 2, no. 5, pp. 454–460, 2011.
- [2] B. O'Regan and M. Grätzel, "A low-cost, high-efficiency solar cell based on dye-sensitized colloidal TiO₂ films," *Nature*, vol. 353, pp. 737–740, 1991.
- [3] F. Hetsch, X. Xu, H. Wang, S. V. Kershaw, and A. L. Rogach, "Semiconductor nanocrystal quantum dots as solar cell components and photosensitizers: material, charge transfer, and separation aspects of some device topologies," *The Journal of Physical Chemistry Letters*, vol. 2, no. 15, pp. 1879–1887, 2011.
- [4] X. Yu, J. Zhu, Y. Zhang, J. Weng, L. Hu, and S. Dai, "SnSe₂ quantum dot sensitized solar cells prepared employing molecular metal chalcogenide as precursors," *Chemical Communications*, vol. 48, no. 27, pp. 3324–3326, 2012.
- [5] Z. Yang, C. Y. Chen, and H. T. Roy, "The abrupt change of electric field breaks the originally established dynamic equilibrium between the Ti oxidation and dissolution of TiO₂," *Chemical Communications*, vol. 47, pp. 9561–9571, 2011.
- [6] L. M. Peter, D. J. Riley, E. J. Tull, and K. G. U. Wijayantha, "Photosensitization of nanocrystalline TiO₂ by self-assembled layers of CdS quantum dots," *Chemical Communications*, no. 10, pp. 1030–1031, 2002.
- [7] I. Robel, V. Subramanian, M. Kuno, and P. V. Kamat, "Quantum dot solar cells. Harvesting light energy with CdSe nanocrystals molecularly linked to mesoscopic TiO₂ films," *Journal of the American Chemical Society*, vol. 128, no. 7, pp. 2385–2393, 2006.
- [8] R. Plass, P. Serge, J. Krüger, and M. Grätzel, "Quantum dot sensitization of organic-inorganic hybrid solar cells," *The Journal of Physical Chemistry B*, vol. 106, pp. 7578–7580, 2002.
- [9] P. Sudhagar, J. H. Jung, S. Park et al., "The performance of coupled (CdS:CdSe) quantum dot-sensitized TiO₂ nanofibrous solar cells," *Electrochemistry Communications*, vol. 11, no. 11, pp. 2220–2224, 2009.
- [10] M. Seol, H. Kim, Y. Tak, and K. Yong, "Novel nanowire array based highly efficient quantum dot sensitized solar cell," *Chemical Communications*, vol. 46, pp. 5521–5523, 2010.
- [11] C. Ratanatawanate, C. Xiong, and K. J. Balkus Jr., "Fabrication of PbS quantum dot doped TiO₂ nanotubes," *ACS Nano*, vol. 2, no. 8, pp. 1682–1688, 2008.
- [12] N. Zhou, G. Chen, X. Zhang et al., "Highly efficient PbS/CdS co-sensitized solar cells based on photoanodes with hierarchical pore distribution," *Electrochemistry Communications*, vol. 20, no. 1, pp. 97–100, 2012.
- [13] B.-R. Hyun, Y.-W. Zhong, A. C. Bartnik et al., "Electron injection from colloidal PbS quantum dots into titanium dioxide nanoparticles," *ACS Nano*, vol. 2, no. 11, pp. 2206–2212, 2008.
- [14] M. Samadpour, P. P. Boix, S. Giménez et al., "Fluorine treatment of TiO₂ for enhancing quantum dot sensitized solar cell performance," *Journal of Physical Chemistry C*, vol. 115, no. 29, pp. 14400–14407, 2011.
- [15] S. Kim, Y. T. Lim, E. G. Soltész et al., "Near-infrared fluorescent type II quantum dots for sentinel lymph node mapping," *Nature Biotechnology*, vol. 22, no. 1, pp. 93–97, 2004.
- [16] X. Gao, Y. Cui, R. M. Levenson, L. W. K. Chung, and S. Nie, "In vivo cancer targeting and imaging with semiconductor quantum dots," *Nature Biotechnology*, vol. 22, no. 8, pp. 969–976, 2004.
- [17] R. G. Xie, K. Chen, X. Y. Chen, and X. Peng, "InAs/InP/ZnSe core/shell/shell quantum dots as near-infrared emitters: bright, narrow-band, non-cadmium containing, and biocompatible," *Nano Research*, vol. 1, pp. 457–464, 2008.
- [18] H. Yang and P. H. Holloway, "Enhanced photoluminescence from CdS:Mn/ZnS core/shell quantum dots," *Applied Physics Letters*, vol. 82, no. 12, pp. 1965–1967, 2003.
- [19] N. Pradhan, D. Goorskey, J. Thessing, and X. Peng, "An alternative of CdSe nanocrystal emitters: pure and tunable impurity emissions in ZnSe nanocrystals," *Journal of the American Chemical Society*, vol. 127, no. 50, pp. 17586–17587, 2005.
- [20] Y. Yang, O. Chen, A. Angerhofer, and Y. C. Cao, "Radial-position-controlled doping in CdS/ZnS core/shell nanocrystals," *Journal of the American Chemical Society*, vol. 128, no. 38, pp. 12428–12429, 2006.
- [21] D. J. Norris, A. L. Efros, and S. C. Erwin, "Doped nanocrystals," *Science*, vol. 319, no. 5871, pp. 1776–1779, 2008.
- [22] W. Lee, W.-C. Kwak, S. K. Min et al., "Spectral broadening in quantum dots-sensitized photoelectrochemical solar cells based on CdSe and Mg-doped CdSe nanocrystals," *Electrochemistry Communications*, vol. 10, no. 11, pp. 1699–1702, 2008.
- [23] X. P. Zou, Z. B. Huang, and H. Q. Zhou, "Application of indium doped plumbous sulfide quantum dots of quantum dot sensitized solar cells and the preparation methods of the doped quantum dots, China," Patent 201210520527.8, 2012.
- [24] S. Jana, B. B. Srivastava, and N. Pradhan, "Correlation of dopant states and host bandgap in dual-doped semiconductor nanocrystals," *The Journal of Physical Chemistry Letters*, vol. 2, no. 14, pp. 1747–1752, 2011.

- [25] R. G. Xie and X. G. Peng, "Synthesis of Cu-doped InP nanocrystals (d-dots) with ZnSe diffusion barrier as efficient and color-tunable NIR emitters," *Journal of the American Chemical Society*, vol. 131, no. 30, pp. 10645–10651, 2009.
- [26] J. W. Lee, D. Y. Son, T. K. Ahn et al., "Quantum dot sensitized solar cell with unprecedentedly high photocurrent," *Scientific Reports*, vol. 3, pp. 1050–1058, 2013.
- [27] K. Prabakar, H. Seo, M. Son, and H. Kim, "CdS quantum dots sensitized TiO₂ photoelectrodes," *Materials Chemistry and Physics*, vol. 117, no. 1, pp. 26–28, 2009.
- [28] Z. B. Huang, X. P. Zou, and H. Q. Zhou, "A strategy to achieve superior photocurrent by Cu-doped quantum dot sensitized solar cells," *Materials Letters*, vol. 95, pp. 139–141, 2013.
- [29] Y.-L. Lee and Y.-S. Lo, "Highly efficient quantum-dot-sensitized solar cell based on co-sensitization of CdS/CdSe," *Advanced Functional Materials*, vol. 19, no. 4, pp. 604–609, 2009.
- [30] H. J. Lee, H. C. Leventis, S. J. Moon et al., "PbS and CdS quantum dot-sensitized solid-state solar cells: "Old Concepts, New Results,"" *Advanced Functional Materials*, vol. 19, no. 17, pp. 2735–2742, 2009.
- [31] G. Hodes, "Chemical bath deposited CdS/CdSe-sensitized porous TiO₂ solar cells," *The Journal of Physical Chemistry C*, vol. 112, no. 46, pp. 17778–17787, 2008.
- [32] F. Zhou, K. Kang, T. Maxisch, G. Ceder, and D. Morgan, "The electronic structure and band gap of LiFePO₄ and LiMnPO₄," *Solid State Communications*, vol. 132, no. 3-4, pp. 181–186, 2004.
- [33] P. Ardalan, T. P. Brennan, H.-B. Lee et al., "Effects of self-assembled monolayers on solid-state CdS quantum dot sensitized solar cells," *ACS Nano*, vol. 5, no. 2, pp. 1495–1504, 2011.
- [34] L. Li, X. Yang, J. Gao et al., "Highly efficient CdS quantum dot-sensitized solar cells based on a modified polysulfide electrolyte," *Journal of the American Chemical Society*, vol. 133, no. 22, pp. 8458–8460, 2011.
- [35] G. Zhu, L. Pan, T. Xu, and Z. Sun, "CdS/CdSe-cosensitized TiO₂ photoanode for quantum-dot-sensitized solar cells by a microwave-assisted chemical bath deposition method," *ACS Applied Materials and Interfaces*, vol. 3, no. 8, pp. 3146–3151, 2011.
- [36] S. W. Watson, "Electrochemical study of SiC particle occlusion during nickel 100 nm wide copper lines made by selective electroless deposition," *Journal of the Electrochemical Society*, vol. 140, pp. 2229–2235, 1993.
- [37] G. Zhu, L. K. Pan, T. Xu, and Z. Sun, "One-step synthesis of CdS sensitized TiO₂ photoanodes for quantum dot-sensitized solar cells by microwave assisted chemical bath deposition method," *ACS Applied Materials and Interfaces*, vol. 3, no. 5, pp. 1472–1478, 2011.
- [38] I. Mora-Seró, S. Giménez, F. Fabregat-Santiago, R. Gómez, Q. Shen, and T. Toyoda, "Recombination in quantum dot sensitized solar cells," *Accounts of Chemical Research*, vol. 42, no. 11, pp. 1848–1857, 2009.
- [39] V. González-Pedro, X. Xu, I. Mora-Seró, and J. Bisquert, "Modeling high-efficiency quantum dot sensitized solar cells," *ACS Nano*, vol. 4, no. 10, pp. 5783–5790, 2010.
- [40] J. G. Radich, R. Dwyer, and P. V. Kamat, "Cu₂S reduced graphene oxide composite for high-efficiency quantum dot solar cells. Overcoming the redox limitations of S₂⁻/S₂²⁻ at the counter electrode," *Journal of Physical Chemistry Letters*, vol. 2, no. 19, pp. 2453–2460, 2011.
- [41] V. Chakrapani, D. Baker, and P. V. Kamat, "Understanding the role of the sulfide redox couple (S²⁻/S_n²⁻) in quantum dot-sensitized solar cells," *Journal of the American Chemical Society*, vol. 133, no. 24, pp. 9607–9615, 2011.
- [42] X.-Y. Yu, J.-Y. Liao, K.-Q. Qiu, D.-B. Kuang, and C.-Y. Su, "Dynamic study of highly efficient CdS/CdSe quantum dot-sensitized solar cells fabricated by electrodeposition," *ACS Nano*, vol. 5, no. 12, pp. 9494–9500, 2011.

Research Article

Investigating the Effect of Piezoelectric Polarization on GaN-Based LEDs with Different Prestrain Layer by Temperature-Dependent Electroluminescence

C. K. Wang,¹ Y. Z. Chiou,¹ T. H. Chiang,² and T. K. Lin²

¹ Department of Electronic Engineering, Southern Taiwan University of Science and Technology, Tainan 71005, Taiwan

² Epistar Corporation, Tainan 744, Taiwan

Correspondence should be addressed to C. K. Wang; ckwang@mail.stust.edu.tw

Received 24 July 2014; Revised 11 September 2014; Accepted 16 September 2014

Academic Editor: Sheng-Po Chang

Copyright © 2015 C. K. Wang et al. This is an open access article distributed under the Creative Commons Attribution License, which permits unrestricted use, distribution, and reproduction in any medium, provided the original work is properly cited.

The effect of piezoelectric polarization on GaN-based light emitting diodes (LEDs) with different kinds of prestrain layers between the multiple quantum wells (MQWs) and n-GaN layer is studied and demonstrated. Compared with the conventional LED, more than 10% enhancement in the output power of the LED with prestrain layer can be attributed to the reduction of polarization field within MQWs region. In this study, we reported a simple method to provide useful comparison of polarization fields within active region in GaN-based LEDs by using temperature-dependent electroluminescence (EL) measurement. The results pointed out that the polarization field of conventional LED was stronger than that of the others due to larger variation of the wavelength transition position (i.e., blue-shift change to red-shift) from 300 to 350 K, and thus the larger polarization field must be effectively screened by injecting more carriers into the MQWs region.

1. Introduction

GaN-based materials generally exist in a wurtzite crystal structure which has a strong polarization field along the *c*-plane direction. Therefore, the space charges induced by spontaneous and piezoelectric polarization fields were at the interfaces of heterostructure for GaN-based materials, for example, in the *c*-plane InGaN/GaN multiple quantum wells (MQWs) structure. This inherent effect, which was called quantum-confined stark effect (QCSE), has resulted in the reduction of quantum efficiency for the GaN-based LEDs. This is because the QCSE within MQWs region lead to the significant spatial separation of the electron and hole wave functions and the reduction of the electron-hole recombination probability [1–5]. Furthermore, investigating the spontaneous and piezoelectric polarization-induced electrostatic field on InGaN/GaN MQWs heterostructure is a very important key issue currently. Thus, many novel and useful growth techniques and structures have been developed to release the strain and reduce the separation of the wave function in the InGaN QWs to improve the optical properties of nitride-based LEDs [6–14].

Besides, some research groups also calculate both the internal electric-field strengths and the carrier density screening of the potential by the measured spectral shifts using photoluminescence (PL) system [15–18]. In our previous work [19], we also successively reported a simple method by temperature-dependent EL measurement to provide useful comparison of electrostatic fields within the QWs of GaN-based LEDs, specifically for structures consisting of identical active regions with different barrier thicknesses. On the other hand, several studies have revealed that the optical properties of LEDs with the structures of InGaN/GaN short-period superlattices (SPS) or low-temperature (LT) GaN layer between the n-GaN and MQWs can be improved due to the release of the residual strain in MQWs, reduction of the QCSE, enhancement of electron-hole recombination rate, reduction of the V-defect density, and improvement of the crystal quality in MQWs [17, 18, 20, 21]. However, it is very necessary to investigate the more detailed relationship between prestrain layer and QCSE. Moreover, in this study, the strengths of the polarization field and the effect of QCSE in the active region of GaN-based LEDs with different

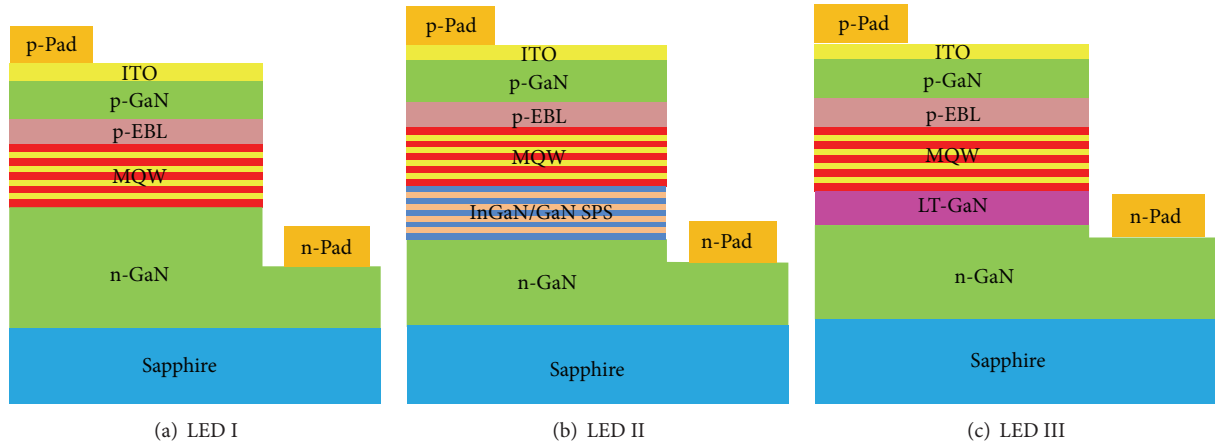


FIGURE 1: The schematic structures of the three fabricated LEDs. (a) LED I without any specific prestrain interlayer. (b) LED II with InGaN/GaN SPS interlayer. (c) LED III with LT-GaN interlayer.

prestrain layer were compared by using our previous method of temperature-dependent EL measurement.

2. Experimental

All samples used in this study were grown on *c*-plane (0001) sapphire (Al_2O_3) substrate by metal-organic chemical vapor deposition (MOCVD). During the growth, trimethylgallium (TMGa), trimethylindium (TMIn), and ammonia (NH_3) were used as gallium, indium, and nitrogen sources, respectively, while biscyclopentadienyl magnesium (CP_2Mg) and disilane (Si_2H_6) were used as the p-type and n-type doping sources, respectively. The conventional LED structure, called LED I, consists of a 30 nm thick buffer layer grown at low temperature, a 1.5 μm thick undoped GaN layer grown at 1040°C, a 2 μm thick Si-doped n-GaN layer grown at 1040°C, and an MQW active region grown at 750°C. The MQW active region consists of 10 periods of 3 nm thick InGaN well layers (with nominal indium content $\sim 17\%$) and 10 nm thick GaN barrier layers. Subsequently, the temperature was elevated to 1000°C to grow a 30 nm thick Mg-doped $\text{p-Al}_{0.15}\text{Ga}_{0.85}\text{N}$ electron blocking layer (EBL) and a 0.3 μm thick p-GaN layer. In order to reduce the strain and polarization effect in the active region, the LEDs with prestrain interlayer structure are also prepared. As shown in Figure 1, the LEDs with lower-indium content ($\sim 5\%$) 10-pair InGaN (2 nm)/GaN (3 nm) SPS interlayer grown at 800°C were labeled as LED II. And the LEDs with LT-GaN (50 nm) interlayer grown at 750°C were labeled as LED III. The as-grown samples were subsequently annealed at 750°C in N_2 ambient to activate Mg in the p-type layers.

After the growth, the surface of the samples was partially etched until the 2 μm thick Si-doped n-GaN layer was exposed. Subsequently, a 70 nm thick indium-tin oxide (ITO) layer was deposited by sputter system onto the p-GaN layer to serve as a current spreading layer. A Ni/Au (30 nm/500 nm) metal contact was deposited on the ITO layer to form the p-electrode. A Ti/Al/Ti/Au (15 nm/450 nm/50 nm/500 nm)

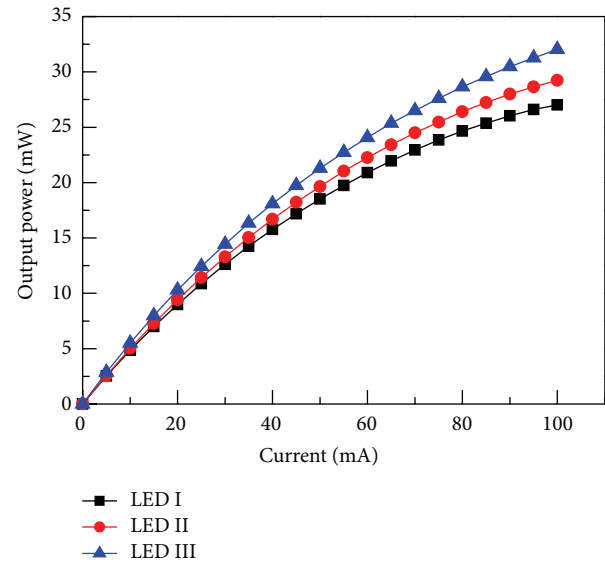


FIGURE 2: Light output powers measured from LEDs I, II, and III as functions of injection currents.

metal contact was then deposited on the exposed n-GaN layer to form the n-electrode. The LEDs fabricated in this study had a chip size of $250 \times 580 \mu\text{m}^2$. The light output powers were measured by the integrating sphere detector. The optical characteristics of these samples were measured by EL system.

3. Results and Discussion

Figure 2 shows the measured light output power as a function of the injection current for these three fabricated LED structures. In order to avoid the effects of self-heating, we applied pulse-width-modulated injection currents on each of the measured LEDs [22]. By increasing the injection current, the light output powers of these three fabricated LED

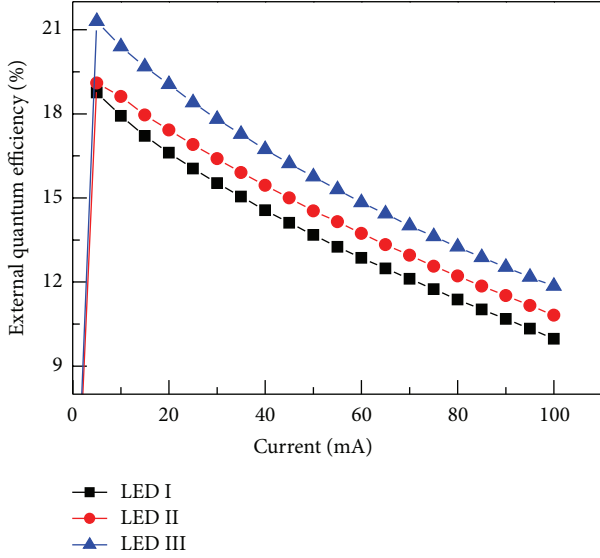


FIGURE 3: EQE as functions of injection currents for LEDs I, II, and III.

structures are increased. At an injection current of 20 mA, the light output powers of LEDs I, II, and III are 8.99, 9.42, and 10.30 mW, respectively. The output powers of LEDs II and III with prestrain structures were 4.8 and 14.6% higher than those of LED I, respectively. It was also found that the difference of output power between these three LEDs was remarkably enlarged especially at higher injection current. Compared with LED I, the light output powers of LEDs II and III were improved by approximately 8.2% and 18.6% under an injection current of 100 mA, respectively. These results show that the light output power can be improved obviously with inserting the prestrain interlayers between the n-GaN and MQWs. This means that the improvement of output power can be attributed to the release of the residual strain, the reduction of the polarization field and QCSE, the enhancement of electron-hole recombination rate, the reduction the V-defect density, and the improvement of the crystal quality in MQWs for LEDs II and III [20, 21]. Figure 3 shows the measured external quantum efficiency (EQE) as a function of injection current. The EQE is defined as

$$\text{EQE} = \frac{P/(h\nu)}{I/e}, \quad (1)$$

where P is the light output power, $h\nu$ is the energy of photon emitted from a semiconductor, I is the injection current, and e is the electron charge. When the LED is operated with injection current, the light power and emission wavelength are measured by integrating sphere detector at the same time. Thus, the values of EQE can be calculated by using (1). The peak efficiency of LEDs I, II, and III is 18.8%, 19.1%, and 23.3%, respectively. The improvement of EQE for LEDs II and III is mainly due to the partial strain relaxation within the active region, which resulted in a less tilt of band-edge and a better overlap of the electron and hole wave functions in each

quantum well. It implies that the polarization field within the active region in this study could be reduced effectively by inserting prestrain interlayer structure.

In order to further differentiate the piezoelectric polarization field for these three fabricated LED structures, the emission spectrum characteristics of the LEDs by temperature-dependent EL were measured and achieved. The temperature of the LEDs was varied by using a heat controller. The temperature was ramped from 300 K up to 350 K with a step of 10 K. Figures 4(a)–4(c) show the peak emission wavelength of these three fabricated LEDs at various ambient temperatures as a function of injection current. First, it was obviously found that the overall emission wavelength in these three LEDs shifted to longer wavelength as the ambient temperature increased. The temperature dependence of the energy band-gap for a semiconductor can be expressed by the *Varshni formula*:

$$E_g = E_g|_{T=0\text{K}} - \frac{\alpha T^2}{T + \beta}, \quad (2)$$

where α and β are fitting parameters, frequently called the Varshni parameters [23]. It indicates that the energy band-gap of semiconductor generally decreases as the temperature increases, and thus the overall emission wavelength of the LEDs shifted to longer wavelength. The reason is that energy band-gap of quantum well became narrow which is caused by the increase in ambient temperature according to the Varshni effect [23, 24].

Then, it was also found that the wavelength of these three LEDs initially shifted toward shorter wavelength and then shifted toward longer wavelength as the injection current was increased. It is well known that the phenomenon of the wavelength shifting toward shorter wavelength was called blue-shift, which can be attributed to the screening effect and band-filling effect [25]. On the contrary, the wavelength shifted toward longer wavelength was called red-shift, which was induced by the thermal effect created by the parasitic resistances of contacts and semiconductor layers due to the I^2R dependence of Joule heating [24]. Regarding the blue-shift values of emission wavelength which was related with polarization field within the active region, it was found that these values for LEDs I, II, and III at room temperature were 1.37, 1.22, and 1.11 nm, respectively. Such a result showed that the conventional LEDs possess a larger blue-shift value than that of LEDs II and III with prestrain interlayer. This is because the stronger QCSE for LED I induced by the spontaneous and piezoelectric fields in the MQW layers would show an obvious screening effect and band-filling effect. These results once more explained that the polarization field within the active region in this study could be reduced effectively by inserting prestrain interlayer structure. Therefore, the output powers of LEDs II and III were improved due to a better overlap of the electron and hole wave functions in each quantum well.

On the other hand, it is very worthy to note that the value of injection current, at which the wavelength of blue-shift changed to red-shift, shifted to larger injection current

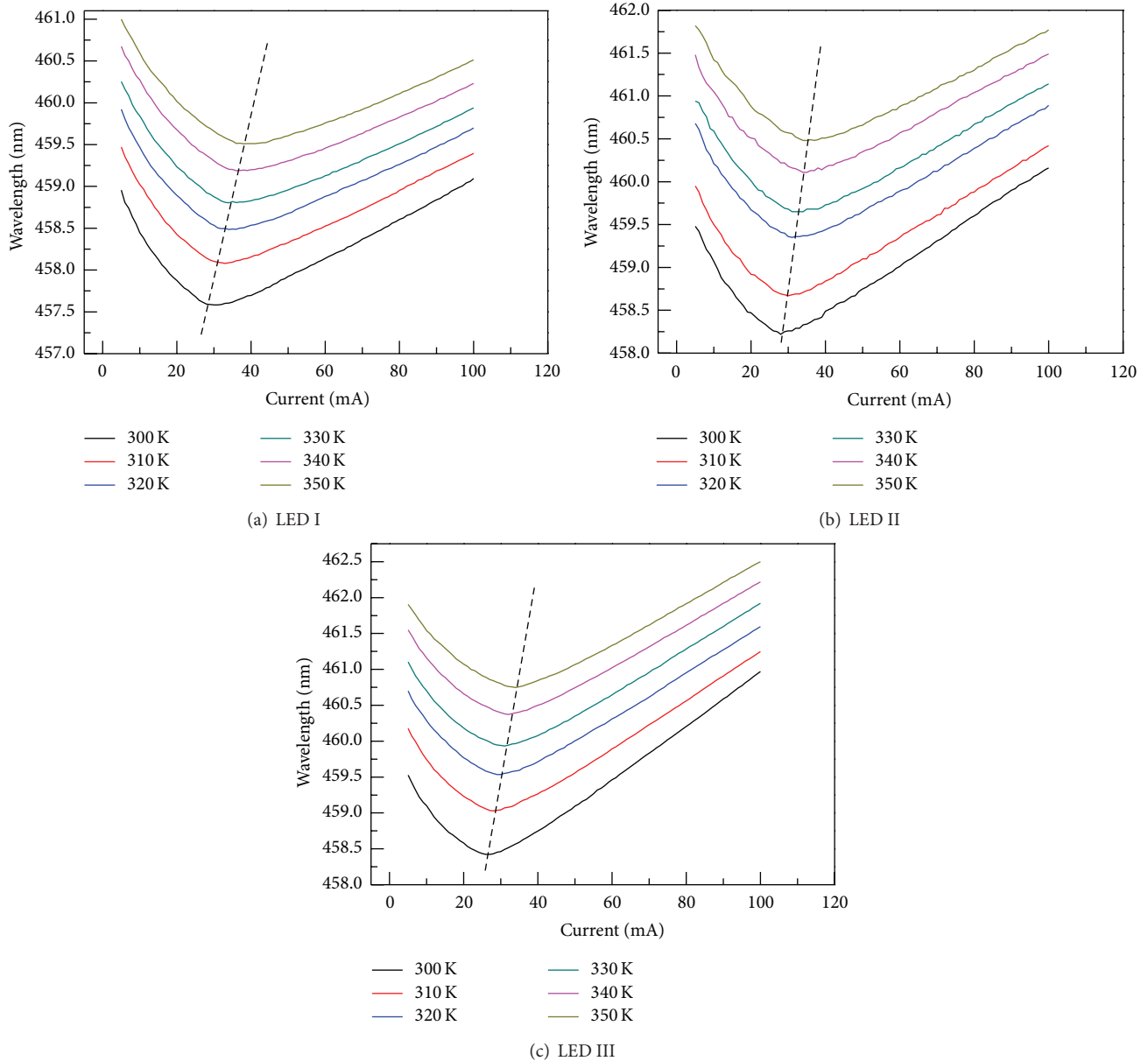


FIGURE 4: The emission wavelengths as functions of injection currents under different ambient temperatures measured from 300 to 350 K for (a) LED I, (b) LED II, and (c) LED III.

when the temperature increased, as shown in the dashed line of Figure 4. It can be seen clearly that LED I as shown in Figure 4(a) has a more obvious change than those of LEDs II and III as shown in Figures 4(b) and 4(c). This is because the carriers injected into the MQWs would be excited by the higher ambient temperature. Thus, these excited carriers would escape from the MQWs, and the energy bandgap of MQWs caused by QCSE cannot be screened and filled effectively. In other words, it needs higher injection current to provide more carriers which can complete the screening effect of LEDs. Therefore, LED I without prestrain structure with more serious QCSE resulting from larger polarization field within the active region must inject more currents into QWs to compensate the screening effect.

Figure 5 also shows the blue-shift value as a function of ambient temperature on these three fabricated LED structures. It was found that the blue-shift values of these three LEDs kept almost the same with increasing ambient temperature. Such a result indicated that the value of blue-shift induced by screening and band-filling effect for these three LEDs was independent of the ambient temperature. In other words, this pointed out that QCSE caused by polarization field in this study did not change with the ambient temperature increase. Figure 6 shows the variation of the injection current of wavelength transition position from blue-shift to red-shift, which was extracted from the dashed line of Figure 4, as a function of the ambient temperature. It can be seen clearly that the slope of conventional LED is

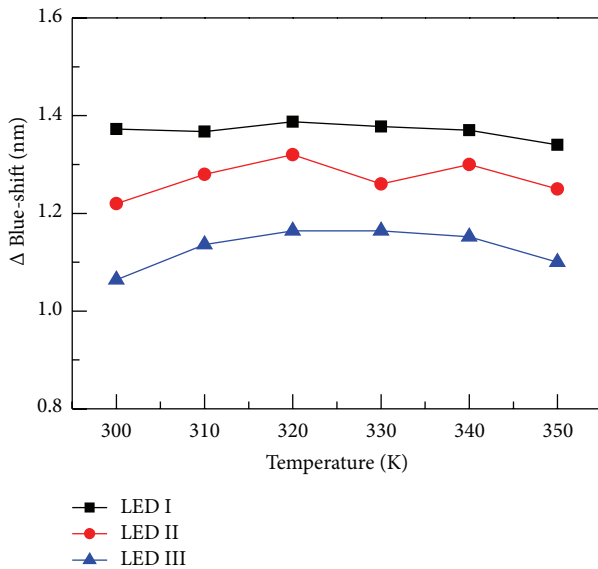


FIGURE 5: Blue-shift values of emission wavelength as functions of ambient temperatures for the three fabricated LEDs.

larger than that of the other LEDs with prestrain interlayer. According to Figure 6, it was found that the injection current of wavelength transition position from blue-shift to red-shift of LED I, LED II, and LED III is 30, 28, and 27 mA at room temperature and that those of LED I, LED II, and LED III are 40, 36, and 34 mA at 350 K. The results again imply that the polarization fields within the active region of LED I were stronger than others due to larger variation of the injection current of the wavelength transition position from 300 K to 350 K, and thus it needed more injection carriers (higher injection current) to complete the screening of QCSE within the active region. Thus, we reported a simple method to provide useful comparison of electrostatic fields within the InGa_N MQW active region on the GaN-based LEDs, specifically for structures consisting of identical active regions with different prestrain layers.

4. Conclusions

The effect of piezoelectric polarization on GaN-based LEDs with different kinds of prestrain layers between the MQWs layers and n-GaN layer is studied and demonstrated. Compared with the conventional LED, it was found that more than 10% enhancement in the output power of the LED with prestrain layer can be attributed to the reduction of polarization field within MQWs layers. In this study, we reported a simple method to provide useful comparison of polarization fields in the LEDs which were estimated using temperature-dependent EL measurement. The results pointed out that the polarization field of conventional LED was stronger than that of the others due to larger variation of the wavelength transition position (i.e., blue-shift change to red-shift) from 300 to 350 K, and thus the larger polarization field must be effectively screened by injecting more carriers.

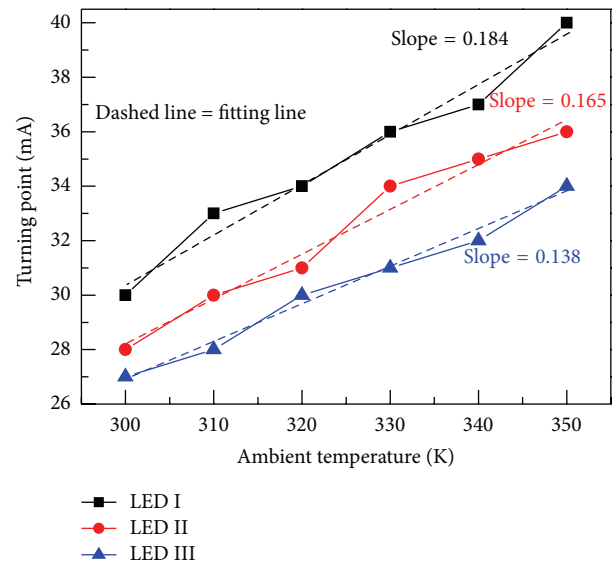


FIGURE 6: The turning points of injection currents (i.e., wavelength transition position from blue-shift to red-shift) as shown by the dashed lines in Figures 4(a)–4(c) as functions of ambient temperatures for the three fabricated LEDs.

Conflict of Interests

The authors declare that there is no conflict of interests regarding the publication of this paper.

Acknowledgment

This work was supported by the National Science Council of Taiwan under Contract nos. NSC 101-2221-E-218-023-MY2 and NSC 101-2632-E-218-001-MY3.

References

- [1] Z. H. Zhang, W. Liu, Z. Ju et al., "Self-screening of the quantum confined Stark effect by the polarization induced bulk charges in the quantum barriers," *Applied Physics Letters*, vol. 104, Article ID 243501, 2014.
- [2] A. Dadgar, L. Groh, S. Metzner et al., "Green to blue polarization compensated c-axis oriented multi-quantum wells by AlGaInN barrier layers," *Applied Physics Letters*, vol. 102, no. 6, Article ID 062110, 2013.
- [3] T. Langer, H. Jönen, A. Kruse, H. Bremers, U. Rossow, and A. Hangleiter, "Strain-induced defects as nonradiative recombination centers in green-emitting GaInN/GaN quantum well structures," *Applied Physics Letters*, vol. 103, no. 2, Article ID 022108, 2013.
- [4] M. Thomsen, H. Jönen, U. Rossow, and A. Hangleiter, "Spontaneous polarization field in polar and nonpolar GaInN/GaN quantum well structures," *Physica Status Solidi (B) Basic Research*, vol. 248, no. 3, pp. 627–631, 2011.
- [5] H.-M. Huang, T.-C. Lu, C.-Y. Chang et al., "Investigation of emission polarization and strain in InGa_N-Ga_N multiple quantum wells on nanorod epitaxially lateral overgrowth templates," *Journal of Lightwave Technology*, vol. 29, no. 18, Article ID 5983376, pp. 2761–2765, 2011.

- [6] H. Zhao, G. Liu, and N. Tansu, "Analysis of InGa δ N-delta-InN quantum wells for light-emitting diodes," *Applied Physics Letters*, vol. 97, no. 13, Article ID 131114, 2010.
- [7] C.-T. Liao, M.-C. Tsai, B.-T. Liou, S.-H. Yen, and Y.-K. Kuo, "Improvement in output power of a 460 nm InGa δ N light-emitting diode using staggered quantum well," *Journal of Applied Physics*, vol. 108, no. 6, Article ID 063107, 2010.
- [8] J. Park and Y. Kawakami, "Photoluminescence property of InGa δ N single quantum well with embedded AlGa δ N δ layer," *Applied Physics Letters*, vol. 88, no. 20, Article ID 202107, 2006.
- [9] Y. Li, B. Liu, R. Zhang, Z. Xie, and Y. Zheng, "Investigation of optical properties of InGa δ NInNInGa δ N/GaN quantum-well in the green spectral regime," *Physica E*, vol. 44, p. 821, 2012.
- [10] L. Zhang, K. Cheng, H. Liang, R. Lieten, M. Leys, and G. Borghs, "Photoluminescence studies of polarization effects in InGa δ N/(In)Ga δ N multiple quantum well structures," *Japanese Journal of Applied Physics*, vol. 51, no. 3, Article ID 030207, 2012.
- [11] H. Zhao, R. A. Arif, Y.-K. Ee, and N. Tansu, "Self-consistent analysis of strain-compensated InGa δ N-AlGa δ N quantum wells for lasers and light-emitting diodes," *IEEE Journal of Quantum Electronics*, vol. 45, no. 1, pp. 66–78, 2009.
- [12] C.-L. Tsai, G.-C. Fan, and Y.-S. Lee, "Effects of strain-compensated AlGa δ N/InGa δ N superlattice barriers on the optical properties of InGa δ N light-emitting diodes," *Applied Physics A: Materials Science and Processing*, vol. 104, no. 1, pp. 319–323, 2011.
- [13] C. H. Wang, S. P. Chang, P. H. Ku et al., "Hole transport improvement in InGa δ N/GaN light-emitting diodes by graded-composition multiple quantum barriers," *Applied Physics Letters*, vol. 99, no. 17, Article ID 171106, 2011.
- [14] R. M. Farrell, E. C. Young, F. Wu, S. P. Denbaars, and J. S. Speck, "Materials and growth issues for high-performance nonpolar and semipolar light-emitting devices," *Semiconductor Science and Technology*, vol. 27, no. 2, Article ID 024001, 2012.
- [15] V. Ramesh, A. Kikuchi, K. Kishino, M. Funato, and Y. Kawakami, "Strain relaxation effect by nanotexturing InGa δ N/GaN multiple quantum well," *Journal of Applied Physics*, vol. 107, no. 11, Article ID 114303, 2010.
- [16] J. Xu, M. F. Schubert, D. Zhu et al., "Effects of polarization-field tuning in GaInN light-emitting diodes," *Applied Physics Letters*, vol. 99, no. 4, Article ID 041105, 2011.
- [17] S. P. Chang, C. H. Wang, C. H. Chiu et al., "Characteristics of efficiency droop in GaN-based light emitting diodes with an insertion layer between the multiple quantum wells and n-GaN layer," *Applied Physics Letters*, vol. 97, no. 25, Article ID 251114, 2010.
- [18] C.-F. Huang, C.-Y. Chen, C.-F. Lu, and C. C. Yang, "Reduced injection current induced blueshift in an InGa δ NGa δ N quantum-well light-emitting diode of prestrained growth," *Applied Physics Letters*, vol. 91, no. 5, Article ID 051121, 2007.
- [19] C. K. Wang, T. H. Chiang, K. Y. Chen et al., "Investigating the effect of piezoelectric polarization on GaN-based LEDs with different quantum barrier thickness," *Journal of Display Technology*, vol. 9, no. 4, pp. 207–212, 2013.
- [20] S. J. Leem, Y. C. Shin, K. C. Kim et al., "The effect of the low-mole InGa δ N structure and InGa δ N/GaN strained layer superlattices on optical performance of multiple quantum well active layers," *Journal of Crystal Growth*, vol. 311, no. 1, pp. 103–106, 2008.
- [21] R.-M. Lin, Y.-H. Lin, C.-H. Chiang et al., "Inserting a low-temperature n-GaN underlying layer to separate nonradiative recombination centers improves the luminescence efficiency of blue InGa δ N/GaN LEDs," *Microelectronics Reliability*, vol. 50, no. 5, pp. 679–682, 2010.
- [22] D. H. Lee, H. K. Lee, J. S. Yu et al., "Temperature and thermal characteristics of InGa δ N/GaN vertical light-emitting diodes on electroplated copper," *Semiconductor Science and Technology*, vol. 26, no. 5, Article ID 055014, 2011.
- [23] Y. P. Varshni, "Temperature dependence of the energy gap in semiconductors," *Physica*, vol. 34, no. 1, pp. 149–154, 1967.
- [24] E. F. Schubert, *Light-Emitting Diodes*, Cambridge University Press, Cambridge, Mass, USA, 2nd edition, 2006.
- [25] D.-Y. Lee, S.-H. Han, D.-J. Lee et al., "Effect of an electron blocking layer on the piezoelectric field in InGa δ N/GaN multiple quantum well light-emitting diodes," *Applied Physics Letters*, vol. 100, no. 4, Article ID 041119, 2012.

Research Article

Hydrothermal Growth of Quasi-Monocrystal ZnO Thin Films and Their Application in Ultraviolet Photodetectors

Yung-Chun Tu,¹ Shui-Jinn Wang,^{1,2} Tseng-Hsing Lin,¹ Chien-Hsiung Hung,¹
Tsung-Che Tsai,¹ Ru-Wen Wu,¹ Kai-Ming Uang,³ and Tron-Min Chen³

¹Institute of Microelectronics, Department of Electrical Engineering, National Cheng Kung University, Tainan 701, Taiwan

²Advanced Optoelectronic Technology Center, National Cheng Kung University, Tainan 701, Taiwan

³Department of Electrical Engineering, Wu Feng University, Chiayi 621, Taiwan

Correspondence should be addressed to Shui-Jinn Wang; sjwang@mail.ncku.edu.tw

Received 28 October 2014; Revised 31 January 2015; Accepted 2 February 2015

Academic Editor: Shyh-Jer Huang

Copyright © 2015 Yung-Chun Tu et al. This is an open access article distributed under the Creative Commons Attribution License, which permits unrestricted use, distribution, and reproduction in any medium, provided the original work is properly cited.

Quasi-monocrystal ZnO film grown using the hydrothermal growth method is used for the fabrication of Cu₂O/ZnO heterojunction (HJ) ultraviolet photodetectors (UV-PDs). The HJ was formed via the sputtering deposition of p-type Cu₂O onto hydrothermally grown ZnO film (HTG-ZnO-film). The effect of annealing temperature in the nitrogen ambient on the photoluminescence spectra of the synthesized ZnO film was studied. The optoelectronic properties of Cu₂O/ZnO film with various Cu₂O thicknesses (250–750 nm) under UV light (365 nm; intensity: 3 mW/cm²) were determined. The UV sensitivity of the HTG-ZnO-film-based UV-PDs and the sputtered ZnO-film-based UV-PDs were 55.6-fold (S_{HTG}) and 8.8-fold (S_{sputter}), respectively. The significant gain in sensitivity ($S_{\text{HTG}}/S_{\text{sputter}} = 630\%$) of the proposed ZnO-film-based device compared to that for the device based on sputtered film can be attributed to the improved photoelectric properties of quasi-monocrystal ZnO film.

1. Introduction

Ultraviolet photodetectors (UV-PDs) have attracted considerable interest for applications such as combustion engineering, missile plume detection, space-to-space communication, ozone layer monitoring, pollution monitoring, and flame detection [1, 2]. UV-PDs have been fabricated on wide-direct-band-gap materials, including ZnO film obtained via spray deposition [3], GaN film obtained via plasma-assisted molecular beam epitaxy [4], and TiO₂ obtained via hydrothermal growth (HTG) [5]. Among them, ZnO is a well-known direct wide band gap (3.37 eV at room temperature) and thermally stable n-type wurtzite semiconductor with a large exciton binding energy (about 60 meV) [6]. It has been widely investigated for its unique properties and potential applications in sensitive devices [7–15].

ZnO-based UV-PDs with a nanowire- (NW) type structure have drawn a lot of attention due to their ease of fabrication, low-temperature processing, and unique properties, such as high aspect ratio, high surface-to-volume ratio,

and good carrier confinement in two dimensions, which benefit device performance [16]. However, UV-PDs based on ZnO NWs usually suffer from a relatively low junction area for photo detection. In addition, the integration of ZnO NWs into a working device remains a complicated, time-consuming, and uneconomical process, and there is a potential short-circuit problem for ZnO-NW-based UV-PDs [17, 18].

In this study, the fabrication of UV-PDs based on a p-Cu₂O/n-ZnO heterojunction (HJ) is demonstrated. A quasi-monocrystalline ZnO film grown on an indium tin oxide- (ITO) coated glass substrate via the hydrothermal method is proposed to serve as the n-type semiconductor with improved photoelectric properties. Sputter deposition is used to deposit cupric oxide (Cu₂O) as the p-type semiconductor. In addition to nontoxicity, low cost, and abundance of the starting material, Cu₂O has a direct band gap of 2.0 eV [19, 20]. A sensing response with a wide spectrum range of 660–300 nm can be expected for the proposed p-Cu₂O/n-ZnO HJ. The effects of Cu₂O film thickness on the optoelectrical

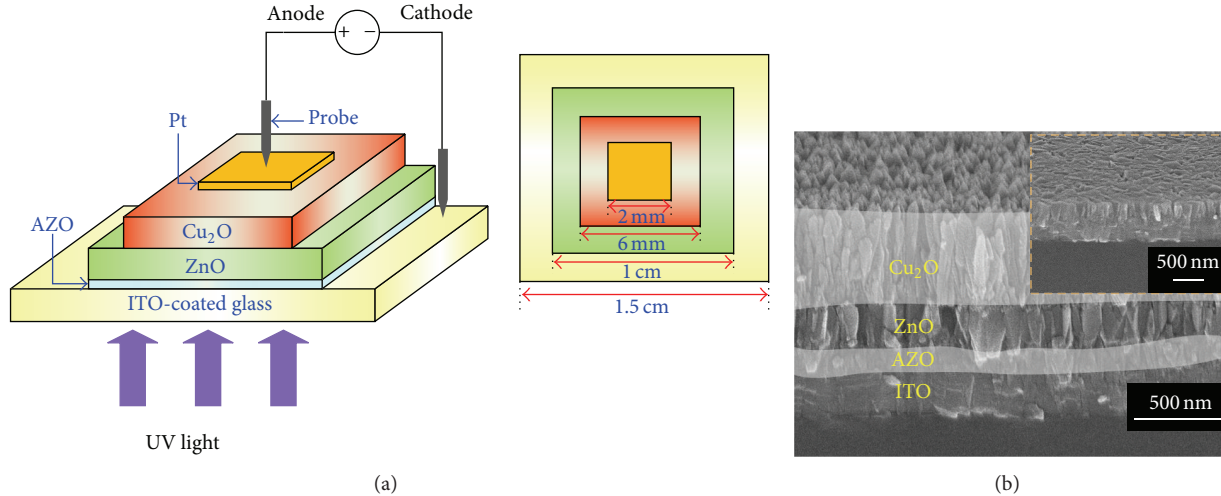


FIGURE 1: Schematic device structure and SEM images of prepared UV-PDs. (a) Schematic device structure and (b) tilted-view images of ZnO (HTG)/AZO/ITO and p-Cu₂O/n-ZnO (HTG)/AZO/ITO structures.

properties of UV-PDs are investigated. Comparisons between the performances of p-Cu₂O/n-ZnO UV-PDs based on n-type ZnO films prepared via HTG and sputtering deposition, respectively, are made.

2. Experimental Details

Figure 1(a) shows the device structures of ZnO-based UV-PDs presented in this work. First, ITO-coated glass substrates were cleaned in a sonicating bath of acetone and isopropanol for 30 min, rinsed in deionized water for 10 min, and dried with nitrogen gas. The ITO-coated glass substrates were used for the fabrication of an n-side-up vertical-structured PD devices. Essentially, the ITO glass substrate is with a high electrical conductivity and high optical transparency ITO coating layer atop glass substrate, which could serve as an excellent transparent electrode for optoelectronic devices with bottom-up fabrication process. In addition, it offers a much shorter length for forward current path ($\sim 1\mu\text{m}$), better current uniformity, and smaller series resistance, as compared with regular PD devices fabricated on glass substrate or insulated substrate. A 150 nm thick aluminum-doped zinc oxide (AZO) film was sputtered on ITO-coated glass substrates using radiofrequency (RF) sputtering with an RF power of 60 W for 90 min to serve as a seed layer. These samples were placed in a solution of 0.06 M zinc nitrate hexahydrate ($\text{Zn}(\text{NO}_3)_2 \cdot 6\text{H}_2\text{O}$) and hexamethylenetetramine ($\text{C}_6\text{H}_{12}\text{N}_4$) at 70°C for 4 h for the growth of ZnO film (300 nm). At the end of the reaction, the samples were removed from the solution, washed with deionized water for 5 min, and dried in nitrogen gas. Subsequently, p-Cu₂O films with three thicknesses (250, 500, and 750 nm) were sputtered onto the surface of the ZnO film by RF sputtering with a power of 90 W for 3, 6, and 9 h, respectively, to complete the fabrication of p-Cu₂O/n-ZnO HJs. To examine the impact of annealing temperature on material quality, the samples were annealed in N₂ gas at 300, 400, 500, and 600°C for 10 min, respectively.

Finally, an ohmic-contact electrode with 200 nm thick Pt film electrodes was deposited on the surface of the p-Cu₂O layer via e-gun evaporation. For comparison, p-Cu₂O (500 nm)/n-ZnO (300 nm) UV-PDs based on sputter-deposited ZnO film of the same thickness and annealed in N₂ gas at 600°C for 10 min were also fabricated. All UV-PDs reported in this work have a die size of 1.5 cm × 1.5 cm and a working area of 6 mm × 6 mm.

The surface morphologies and thicknesses of the grown ZnO film and p-Cu₂O/n-ZnO structure were characterized using scanning electron microscopy (SEM; Hitachi SU8000) at an accelerating voltage of 10 keV. The crystal structure and optical properties of ZnO films fabricated via HTG were examined using X-ray diffraction (XRD; D/MAX2500, Rigaku) with CuK α (wavelength: 1.5418 Å) radiation at a scan step of 0.01° (2θ), UV-visible-near-infrared double-beam spectrophotometry (U-3010 UV-VIS) with a 300–900 nm spectral range, and photoluminescence (PL) with an He-Cd laser as the light source using an excitation wavelength of 325 nm and a power of 3 mW, respectively. The current density-voltage (J - V) characteristics of the p-Cu₂O/n-ZnO film fabricated via HTG were measured using a Keithley 2636 voltage source instrument at room temperature in darkness and under 500-W Xe arc lamp illumination.

3. Results and Discussion

SEM images of the grown ZnO film and the prepared p-Cu₂O (500 nm)/n-ZnO structure on an AZO/ITO substrate are shown in Figure 1(b). ZnO film with a controllable thickness (300 nm) was obtained by regulating the solution concentration, temperature, and growth time. As revealed by the inset in the figure, the grown ZnO film fully covered the AZO/ITO substrate, which effectively prevented the p-type material (Cu₂O) from reaching the substrate during HJ formation and avoided the possible short-circuit problem usually encountered for ZnO-NW-based UV-PDs [17, 18].

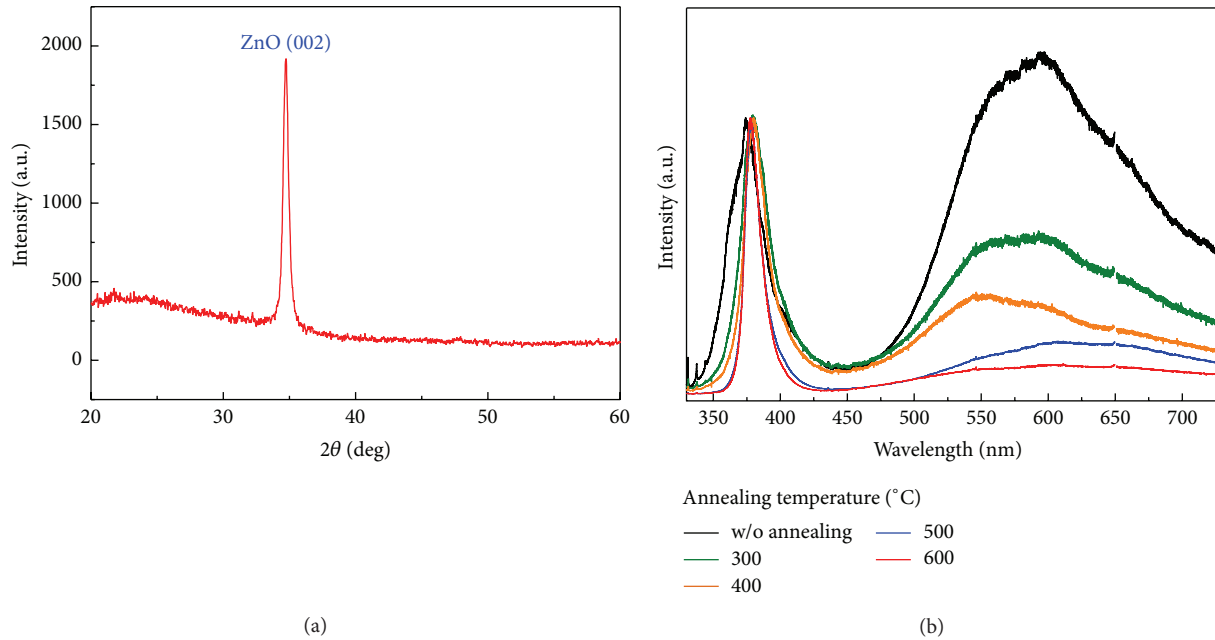


FIGURE 2: (a) XRD pattern of prepared n-ZnO film with quasi-monocrystal structure fabricated via HTG. (b) PL spectra of ZnO film (HTG) for various annealing temperatures in nitrogen.

The mechanism of the growth of the quasi-monocrystal ZnO film on the ITO-coated glass substrate can be attributed to the well-controlled parameters, such as solution concentration, temperature, and growth time, of the HTG process. It has been reported that these parameters have a strong impact on the aspect ratio of ZnO NWs [21]. A lower HTG temperature, higher solution concentration, and longer growth time lead to a larger diameter of ZnO NWs. ZnO films were formed through the aggregation of NWs and then followed by self-organized growth among interconnected NWs [22]. As shown in Figure 1(b), the sputter-deposited p-Cu₂O film had a dense NW-like morphology. It is speculated that the sputtering power used in this work might have enough energy to increase the nucleation kinetics during sputter deposition, which is in good agreement with the experimental findings on sputter-deposited Cu₂O films with various sputtering powers [23, 24].

The material properties of the prepared ZnO film were analyzed by XRD and PL, with the results shown in Figure 2. On the basis of the diffraction peak that corresponded to the (002) plane shown in Figure 2(a), the ZnO film fabricated via HTG was indexed to have a hexagonal wurtzite signal according to the standard JCPDS card [25]. This indicates that ZnO films fabricated via HTG are mainly formed via self-organized growth interconnections of closely packed crystalline columnar ZnO with the *c*-axis vertical to the substrate surface. It is believed that the ZnO films fabricated via HTG in the present work do have a quasi-monocrystalline structure. The influence of thermal annealing conditions on the PL spectra of the ZnO films fabricated via HTG on a controlled wafer was examined. The results are shown in Figure 2(b). The ZnO films with and without annealing exhibit UV and visible (VIS) emission peaks with different

full widths at half maximum (FWHM) values for the former and different intensities for the latter. The UV and VIS emission peaks are attributed to free exciton recombination and a transition of excited optical centers from a deep level to the valence level arising from singly ionized oxygen vacancies [26], respectively. Our results show that the intensity of the VIS light emission peak decreases with increasing annealing temperature. This might be due to the nitrogen atmosphere suppressing the reevaporation of oxygen during annealing. At the same time, nonradiative-related defects may have been reduced, increasing UV emission [27]. As a result, a considerable decay in VIS emission intensity of the nitrogen-annealed ZnO films fabricated via HTG was observed.

Figure 3 shows the measured *J-V* curves of the p-Cu₂O/ZnO film (HTG) HJs in darkness. The fabricated HJs with various Cu₂O thicknesses after annealing at 600°C in nitrogen all exhibit well-defined rectifying behaviors. In this work, the electron concentrations in the annealed ZnO film and the hole concentration in the annealed Cu₂O are $1\sim 2 \times 10^{16} \text{ cm}^{-3}$ and $2\sim 3 \times 10^{15} \text{ cm}^{-3}$, respectively, based on Hall measurements. The width of depletion region corresponding to the abovementioned carrier concentrations is 350~500 nm (Cu₂O: 300~400 nm; ZnO: 50~90 nm). The band offsets between ZnO and Cu₂O are $\Delta E_c = 0.9 \text{ eV}$ and $\Delta E_v = 2.17 \text{ eV}$ [28], respectively. Note that the sample with 250 nm thick Cu₂O film exhibits the highest forward current, which can be attributed to the thickness of the Cu₂O layer being insufficient, and as a result, both the built-in voltage and the depletion region were limited. Similarly, the decrease in the forward current of the 750 nm thick Cu₂O device might be due to the series resistance of the thicker Cu₂O layer. The annealed sample with 500 nm thick Cu₂O film is the most suitable for UV-PDs because it has the best trade-off between

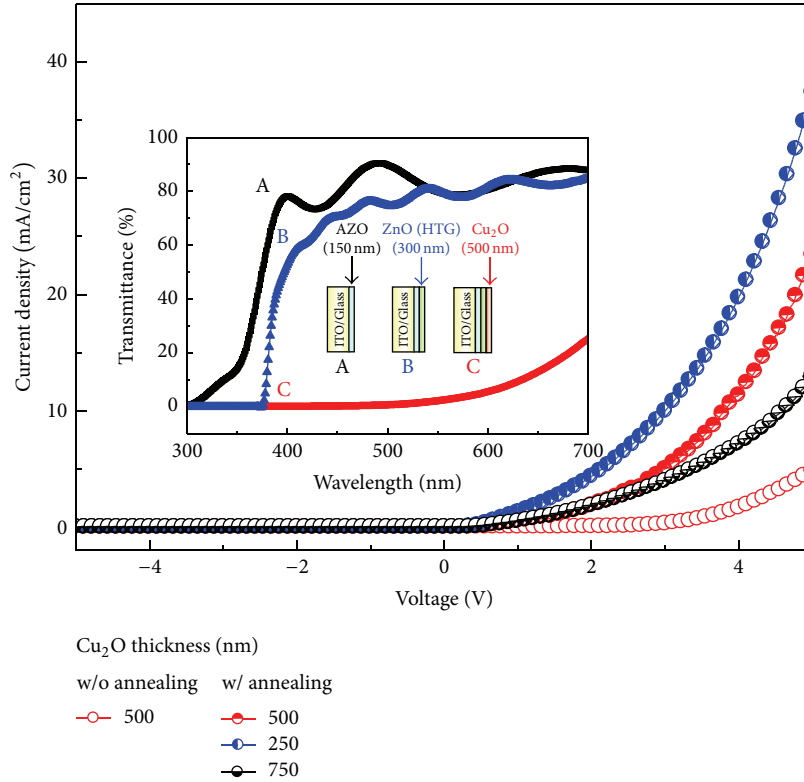


FIGURE 3: Experimental J - V curves of p - $\text{Cu}_2\text{O}/\text{ZnO}$ film (HTG) HJs in darkness. Inset shows the measured transmittance of the prepared samples after annealing. ITO-coated glass substrate after AZO (150 nm) layer deposition (structure A), with an additional ZnO film (HTG) (300 nm) (structure B), and with a Cu_2O layer (500 nm) atop structure B (structure C).

built-in voltage/depletion width and the series resistance. The annealed device with 500 nm thick Cu_2O film exhibits a lower forward threshold voltage (V_{th} at $0.1 \text{ mA}/\text{cm}^2$) of 0.5 V and a lower leakage current (J_r) of $9 \times 10^{-8} \text{ A}/\text{cm}^2$ biased at -1 V compared to those of the unannealed devices ($V_{\text{th}} = 2.5 \text{ V}$; $J_r = 1.37 \times 10^{-7} \text{ A}/\text{cm}^2$). These results suggest that ZnO films fabricated via HTG have improved material quality, including reduced defect states and enhanced crystallinity, after thermal annealing [29]. The light transmittances of the annealed samples including AZO film (150 nm) and ZnO film (300 nm) fabricated via HTG/AZO and Cu_2O film (500 nm)/ZnO/AZO prepared atop the ITO glass substrate are compared in the inset of Figure 3. The $\text{Cu}_2\text{O}/\text{ZnO}/\text{AZO}$ structure has the lowest transmittance (0~1%) in the UV light spectrum, indicating that both Cu_2O and ZnO films have strong UV light absorptivity.

Figure 4 shows the measured reverse-biased J - V characteristics of the prepared HJs based on ZnO films fabricated via HTG in the dark or under various illumination conditions. The experimental results indicate that unannealed UV-PDs are responsive to both UV and VIS light and that annealed UV-PDs are only sensitive to UV light, avoiding VIS interference during UV detection. The improved performance of the annealed UV-PDs can be attributed to the suppression of structural and interfacial defects, which decreases the component of photocurrent through defect states to the conduction band in the ambient in the presence of VIS light.

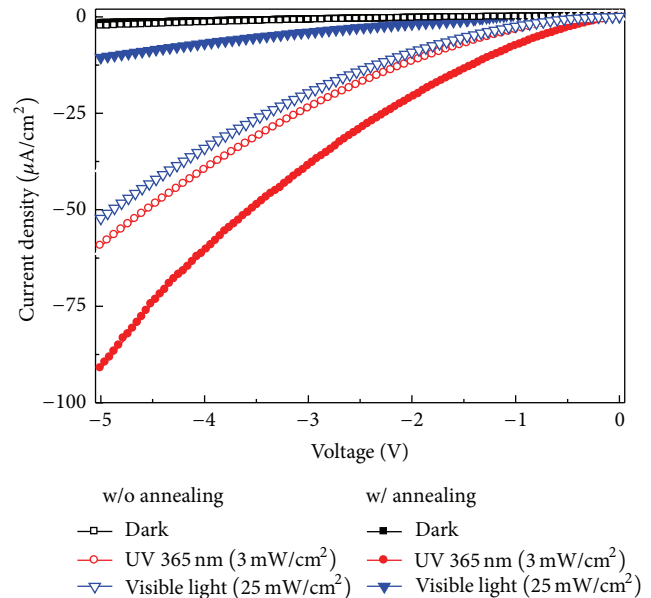


FIGURE 4: Comparisons of experimental J - V curves of p - $\text{Cu}_2\text{O}/\text{ZnO}$ (HTG) sample with and without thermal annealing.

Figure 5 shows the spectral response of the annealed UV-PDs measured under a reverse bias of 1V. It was found that the responsibility shows a cutoff at around 370~390 nm and the

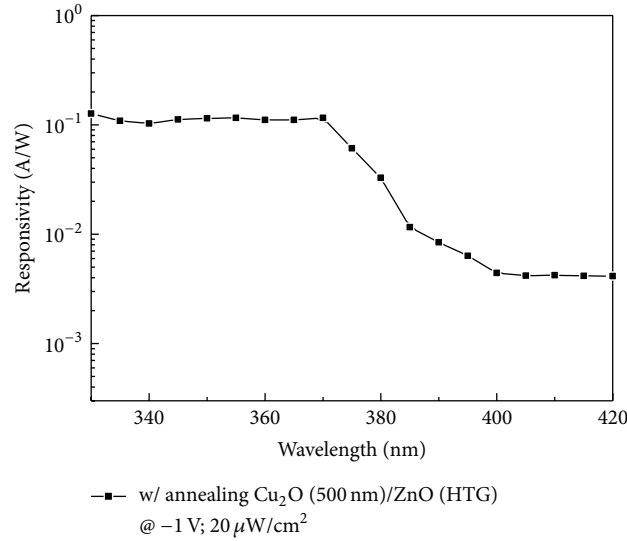


FIGURE 5: Spectral response of the p-Cu₂O/ZnO (HTG) sample UV sensor measured at a reverse bias of 1 V.

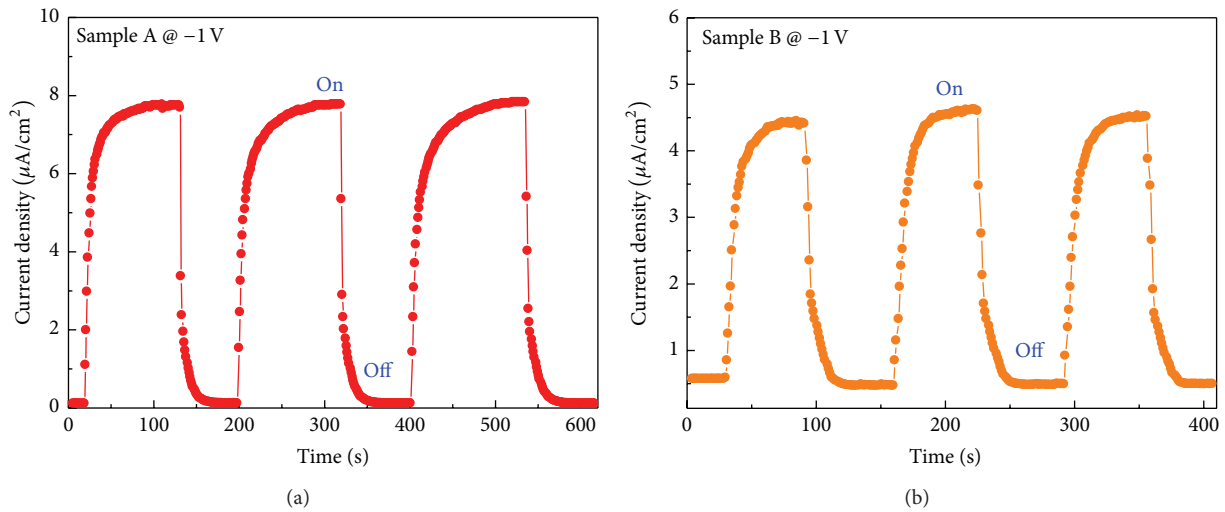


FIGURE 6: Transient response of photocurrent density of fabricated devices based on ZnO film (HTG) (sample A) and sputter-deposited ZnO film (sample B). Wavelength and intensity of UV light are 365 nm and 3 mW/cm², respectively.

response of the UV region (330~370 nm) is nearly constant which is higher than that of in the visible spectrum by one order more.

Figure 6 shows the dynamic photoresponses of the UV-PDs annealed at 600°C in nitrogen based on hydrothermally grown and sputter-deposited ZnO films, respectively (referred to as samples A and B, resp.). Note that the thicknesses of the p-Cu₂O and ZnO layers were 500 and 300 nm, respectively. The response times of the devices with sputter-deposited and hydrothermally grown films are about 20 and 22 s and the recovery times are about 26 and 30 s, respectively. The device based on hydrothermally grown film shows a 55.6-fold increase in the current at -1 V with irradiation under 365 nm UV light and a power density of 3 mW/cm² compared to that for the device based on sputter-deposited film. The enhanced photoresponse of the former

device is mainly attributed to the hydrothermal-grown ZnO film which was formed by aggregated single-crystalline ZnO nanowires with the *c*-axis vertical to the substrate surface. It provides parallel current paths through the coalesced single-crystalline ZnO nanowires with much better optoelectronic properties, as compared with the sputter-deposited ZnO films with polycrystalline or amorphous structure. In addition, thermal annealing offers further improvement in the ZnO film quality through suppressing nonradiative-related defects as revealed from PL measurements.

In recent years, ZnO-based UV PDs have been widely reported. Lee et al. reported the RF sputtering of p-NiO film onto the surface of the ZnO NW by MOCVD and the measured UV sensitivity, response times, and recovery times were 11.3-fold, 72 s, and 110 s, respectively. Wang et al. reported the hydrothermal growth of ZnO NW on CuO

nanowires and the measured UV sensitivity, response times, and recovery times were 3-fold, 100 s, and 141 s, respectively. More recently, Guo et al. presented the hydrothermal growth of ZnO nanorod arrays on NiO nanowires and the measured UV sensitivity, response times, and recovery times were 23-fold, 55 s, and 70 s, respectively [30–32]. In this work, the preparation of p-Cu₂O/ZnO film (HTG) HJs is with measured UV sensitivity, response times, and recovery times which were 55.6-fold, 20 s, and 26 s, respectively, which are comparably much better than those of UV-PDs reported in the literature mentioned above.

4. Conclusion

The preparation of p-Cu₂O/ZnO film (HTG) HJs with good UV sensitivity was demonstrated. ZnO films with a controllable thickness (300 nm) that fully covered the AZO/ITO substrate were obtained by suitably regulating the solution concentration, temperature, and growth time of the HTG process. According to the XRD and PL analyses, the ZnO film fabricated via HTG had a quasi-monocrystalline structure. Thermal annealing in nitrogen at 600°C effectively eliminated defect states in the ZnO films, suppressing VIS interference during UV light detection. Experimental results reveal that the p-Cu₂O/n-ZnO films fabricated via HTG have a fairly good response to UV light (3 mW/cm² at 365 nm) with an increase in the photocurrent of about 55.6-fold compared to that for the device based on sputter-deposited film. It is expected that the HJs based on ZnO film fabricated via HTG will be suitable for future optoelectronic applications.

Conflict of Interests

The authors declare that there is no conflict of interests regarding the publication of this paper.

Acknowledgments

This work was supported by the Ministry of Science and Technology (MOST) of Taiwan, under Grant MOST 103-2221-E-006-132 and the National Science Council (NSC) of Taiwan, under Grant NSC 102-2221-E-006-217-MY2. The authors would like to thank the National Nano Device Laboratories and the Center for Micro/Nano Science and Technology, National Cheng Kung University, Taiwan, for equipment access and financial and technical support.

References

- [1] K. J. Chen, F. Y. Hung, S. J. Chang, and S. J. Young, "Optoelectronic characteristics of UV photodetector based on ZnO nanowire thin films," *Journal of Alloys and Compounds*, vol. 479, no. 1-2, pp. 674–677, 2009.
- [2] K. Liu, M. Sakurai, and M. Aono, "ZnO-based ultraviolet photodetectors," *Sensors*, vol. 10, no. 9, pp. 8604–8634, 2010.
- [3] S. I. Inamdar and K. Y. Rajpure, "High-performance metal-semiconductor-metal UV photodetector based on spray deposited ZnO thin films," *Journal of Alloys and Compounds*, vol. 595, pp. 55–59, 2014.
- [4] M. Z. M. Yusoff, A. Mahyuddin, Z. Hassan et al., "AlN/GaN/AlN heterostructures grown on Si substrate by plasma-assisted MBE for MSM UV photodetector applications," *Materials Science in Semiconductor Processing*, vol. 29, pp. 231–237, 2015.
- [5] Y. Xie, L. Wei, Q. Li et al., "High-performance self-powered UV photodetectors based on TiO₂ nano-branched arrays," *Nanotechnology*, vol. 25, no. 7, Article ID 075202, 2014.
- [6] S.-P. Chang, S.-J. Chang, C.-Y. Lu et al., "A ZnO nanowire-based humidity sensor," *Superlattices and Microstructures*, vol. 47, no. 6, pp. 772–778, 2010.
- [7] F. S. Tsai, S. J. Wang, Y. C. Tu et al., "Preparation of p-SnO/n-ZnO heterojunction nanowire arrays and their optoelectronic characteristics under UV illumination," *Applied Physics Express*, vol. 4, no. 2, Article ID 025002, pp. 1–3, 2011.
- [8] F.-S. Tsai and S.-J. Wang, "Enhanced sensing performance of relative humidity sensors using laterally grown ZnO nanosheets," *Sensors and Actuators B: Chemical*, vol. 193, pp. 280–287, 2014.
- [9] D. An, Y. Li, X. Lian, Y. Zou, and G. Deng, "Synthesis of porous ZnO structure for gas sensor and photocatalytic applications," *Colloids and Surfaces A: Physicochemical and Engineering Aspects*, vol. 447, pp. 81–87, 2014.
- [10] T.-Y. Chen, H.-I. Chen, C.-S. Hsu et al., "ZnO-nanorod-based ammonia gas sensors with underlying Pt/Cr interdigitated electrodes," *IEEE Electron Device Letters*, vol. 33, no. 10, pp. 1486–1488, 2012.
- [11] P.-Y. Yang, J.-L. Wang, W.-C. Tsai et al., "Photoresponse of hydrothermally grown lateral ZnO nanowires," *Thin Solid Films*, vol. 518, no. 24, pp. 7328–7332, 2010.
- [12] C. Tian, D. Jiang, B. Li et al., "Performance enhancement of ZnO UV photodetectors by surface plasmons," *ACS Applied Materials and Interfaces*, vol. 6, no. 3, pp. 2162–2166, 2014.
- [13] S. P. Chang, C. Y. Lu, S. J. Chang, Y. Z. Chiou, T. J. Hsueh, and C. L. Hsu, "Electrical and optical characteristics of UV photodetector with interlaced ZnO nanowires," *IEEE Journal on Selected Topics in Quantum Electronics*, vol. 17, no. 4, pp. 990–995, 2011.
- [14] H. Y. Chen, K. W. Liu, X. Chen et al., "Realization of a self-powered ZnO MSM UV photodetector with high responsivity using an asymmetric pair of Au electrodes," *Journal of Materials Chemistry C*, vol. 2, no. 45, pp. 9689–9694, 2014.
- [15] S. P. Chang, R. W. Chuang, S. J. Chang, C. Y. Lu, Y. Z. Chiou, and S. F. Hsieh, "Surface HCl treatment in ZnO photoconductive sensors," *Thin Solid Films*, vol. 517, no. 17, pp. 5050–5053, 2009.
- [16] Y. B. Li, F. D. Valle, M. Simonnet, I. Yamada, and J.-J. Delaunay, "High-performance UV detector made of ultra-long ZnO bridging nanowires," *Nanotechnology*, vol. 20, no. 4, Article ID 045501, 2009.
- [17] L. Luo, Y. Zhang, S. S. Mao, and L. Lin, "Fabrication and characterization of ZnO nanowires based UV photodiodes," *Sensors and Actuators A: Physical*, vol. 127, no. 2, pp. 201–206, 2006.
- [18] J. Y. Wang, C. Y. Lee, Y. T. Chen et al., "Double side electroluminescence from p-NiO/n-ZnO nanowire heterojunctions," *Applied Physics Letters*, vol. 95, no. 13, Article ID 131117, pp. 1–3, 2009.
- [19] X. Zou, H. Fan, Y. Tian, and S. Yan, "Synthesis of Cu₂O/ZnO hetero-nanorod arrays with enhanced visible light-driven photocatalytic activity," *CrystEngComm*, vol. 16, no. 6, pp. 1149–1156, 2014.
- [20] M. Izaki, T. Shinagawa, K.-T. Mizuno, Y. Ida, M. Inaba, and A. Tasaka, "Electrochemically constructed p-Cu₂O/n-ZnO heterojunction diode for photovoltaic device," *Journal of Physics D: Applied Physics*, vol. 40, no. 11, pp. 3326–3329, 2007.

- [21] M. Guo, P. Diao, and S. Cai, "Hydrothermal growth of well-aligned ZnO nanorod arrays: dependence of morphology and alignment ordering upon preparing conditions," *Journal of Solid State Chemistry*, vol. 178, no. 6, pp. 1864–1873, 2005.
- [22] N. Yu, L. Du, H. Du et al., "Synthesis of ZnO film on P-GaN/Si(111) by one-step hydrothermal method," *Thin Solid Films*, vol. 550, pp. 206–209, 2014.
- [23] A. S. Reddy, H.-H. Park, V. S. Reddy et al., "Effect of sputtering power on the physical properties of dc magnetron sputtered copper oxide thin films," *Materials Chemistry and Physics*, vol. 110, no. 2-3, pp. 397–401, 2008.
- [24] Z. G. Yin, H. T. Zhang, D. M. Goodner et al., "Two-dimensional growth of continuous Cu_2O thin films by magnetron sputtering," *Applied Physics Letters*, vol. 86, no. 6, Article ID 061901, pp. 1–3, 2005.
- [25] Y.-C. Tu, S.-J. Wang, J.-C. Lin et al., "Light output improvement of GaN-based light-emitting diodes using hydrothermally grown ZnO nanotapers," *Japanese Journal of Applied Physics*, vol. 52, no. 6, Article ID 06GG13, 2013.
- [26] H. S. Kang, J. S. Kang, S. S. Pang, E. S. Shim, and S. Y. Lee, "Variation of light emitting properties of ZnO thin films depending on post-annealing temperature," *Materials Science and Engineering B*, vol. 102, no. 1–3, pp. 313–316, 2003.
- [27] L. H. Quang, S. J. Chua, K. P. Loh, and E. Fitzgerald, "The effect of post-annealing treatment on photoluminescence of ZnO nanorods prepared by hydrothermal synthesis," *Journal of Crystal Growth*, vol. 287, no. 1, pp. 157–161, 2006.
- [28] H. T. Hsueh, S. J. Chang, W. Y. Weng et al., "Fabrication and characterization of coaxial p-copper oxide/n-ZnO nanowire photodiodes," *IEEE Transactions on Nanotechnology*, vol. 11, no. 1, pp. 127–133, 2012.
- [29] K. H. Tam, C. K. Cheung, Y. H. Leung et al., "Defects in ZnO nanorods prepared by a hydrothermal method," *Journal of Physical Chemistry B*, vol. 110, no. 42, pp. 20865–20871, 2006.
- [30] T. Guo, Y. Luo, Y. Zhang, Y.-H. Lin, and C.-W. Nan, "Controllable growth of ZnO nanorod arrays on NiO nanowires and their high UV photoresponse current," *Crystal Growth and Design*, vol. 14, no. 5, pp. 2329–2334, 2014.
- [31] K. R. Lee, B. O. Jung, S. W. Cho, K. Senthil, and H. K. Cho, "Semitransparent all-oxide p-NiO/n-ZnO nanowire ultraviolet photosensors," *Journal of Materials Research*, vol. 28, no. 18, pp. 2605–2610, 2013.
- [32] S.-B. Wang, C.-H. Hsiao, S.-J. Chang et al., "ZnO branched nanowires and the p-CuO/n-ZnO heterojunction nanostructured photodetector," *IEEE Transactions on Nanotechnology*, vol. 12, no. 2, pp. 263–269, 2013.

Research Article

Scalability of Phase Change Materials in Nanostructure Template

Wei Zhang,¹ Biyun L. Jackson,² Ke Sun,³ Jae Young Lee,⁴ Shyh-Jer Huang,⁵ Hsin-Chieh Yu,⁵ Sheng-Po Chang,⁵ Shoou-Jinn Chang,⁵ and Ya-Hong Xie¹

¹Department of Materials Science and Engineering, University of California, Los Angeles, Los Angeles, CA 90095, USA

²Portland Technology Development, Intel Corporation, Hillsboro, OR 97124, USA

³WaferTech LLC, Camas, WA 98607, USA

⁴GLOBALFOUNDRIES, Inc., Milpitas, CA 95035, USA

⁵Advanced Optoelectronic Technology Center, Institute of Microelectronics, Department of Electrical Engineering, National Cheng Kung University, Tainan 701, Taiwan

Correspondence should be addressed to Ya-Hong Xie; yahong.xie@gmail.com

Received 23 September 2014; Accepted 11 December 2014

Academic Editor: Jimmy C. Yu

Copyright © 2015 Wei Zhang et al. This is an open access article distributed under the Creative Commons Attribution License, which permits unrestricted use, distribution, and reproduction in any medium, provided the original work is properly cited.

The scalability of In_2Se_3 , one of the phase change materials, is investigated. By depositing the material onto a nanopatterned substrate, individual In_2Se_3 nanoclusters are confined in the nanosize pits with well-defined shape and dimension permitting the systematic study of the ultimate scaling limit of its use as a phase change memory element. In_2Se_3 of progressively smaller volume is heated inside a transmission electron microscope operating in diffraction mode. The volume at which the amorphous-crystalline transition can no longer be observed is taken as the ultimate scaling limit, which is approximately 5 nm^3 for In_2Se_3 . The physics for the existence of scaling limit is discussed. Using phase change memory elements in memory hierarchy is believed to reduce its energy consumption because they consume zero leakage power in memory cells. Therefore, the phase change memory applications are of great importance in terms of energy saving.

1. Introduction

Chalcogenide phase change materials (PCM) are a family of materials with prominent contrast in conductivity between amorphous state (highly resistive) and crystalline state (highly conductive) [1]. When used as nonvolatile memory elements, crystalline-to-amorphous phase transition is conventionally accomplished by Joule heating from an electrical current pulse, during which the material is heated to above melting temperature followed by rapid quenching leaving the material being frozen in the amorphous state. The opposite amorphous-to-crystalline transition is achieved by heating to below melting temperature followed by a gradual lowering of the temperature leading to the formation of crystalline state [2–4]. Using phase change memory elements as nonvolatile memory in memory hierarchy is believed to reduce its energy consumption because they consume zero leakage power in

memory cells. This advantage makes phase change memory element a perfect candidate in the memory industry due to its excellent performance in energy consumption. Driven by Moore's law [5], the system functionality increases rapidly in the same size package with decreasing device dimensions. A question crucial to the technology development of phase change random access memories (PcRAM) is the ultimate scaling limit. Despite the fact that the phase transition of some PCM in bulk form is well studied by dedicated groups [3, 6–8] and the fact that ultimate limit of phase change in $\text{Ge}_2\text{Sb}_2\text{Te}_5$ was reported [9], the size effects of In_2Se_3 , another important candidate in the PCM family, have not been reported yet. Size effects start to play an important role as PCM devices scale further down to below 10 nm. Under these nanometer scale dimensions—(a) neither the crystallization temperature nor the melting temperature is the same as those of bulk and (b) crystalline state needs to

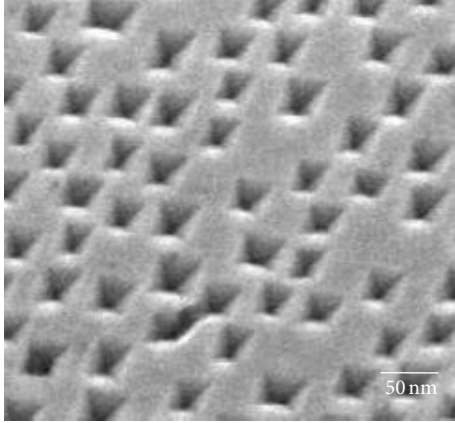


FIGURE 1: 35° tilt SEM image of nanopit substrate after KOH etching.

have long range order—the amorphous and crystalline states may not be thermodynamically distinguishable any more. Therefore, a concern may be raised as to whether PCM has a size limit; that is, the crystalline state becomes unstable when the volume is reduced to a certain value. In this work, the scalability and ultimate size limit of In_2Se_3 are investigated. By depositing In_2Se_3 onto a unique nanopit substrate, size effects of the nano-volume In_2Se_3 confined in individual nanopits can be studied. The underlying physics of the diminishing of crystalline state is discussed.

2. Experiment

The fabrication of nanopit substrate is achieved by anisotropic KOH etching of Si. Figure 1 shows the SEM image of the nanopit substrate. Detailed process flow has been reported previously [10]. The tip of the nanopit is atomically sharp with the radius of curvature being less than 1 nm [11]. Amorphous In_2Se_3 with different nominal thickness is deposited onto the nanopit substrate by sputtering, followed by SiO_2 capping layer to prevent the oxidation of In_2Se_3 . Morphologies of the as-deposited films are examined by STEM. In order to determine the ultimate size limit, in situ heating TEM is used to observe the crystallization and melting behaviors of the nano-volume In_2Se_3 .

3. Results and Discussions

3.1. Coverage of In_2Se_3 on Nanopit Substrate. Six different thicknesses (2, 3, 5, 8, 23, and 45 nm) of In_2Se_3 were deposited on the nanopitted substrate. STEM studies revealed that two types of morphologies exist depending on the nominal film thickness. In Figure 2(a), bare Si nanopit substrate is shown. The contrast of the bare pit image is mainly from mass-thickness contrast since Si is the only element in the sample [12]. Similarly, the contrast of Figure 2(c), showing the 45 nm nominal film thickness of In_2Se_3 on nanopit substrate, is also contributed from mass-thickness contrast only since In_2Se_3 covers the whole sample surface. The difference between the morphologies of the two images is the size of the open area in the pit region. Smaller opening area for the 45 nm

sample results from that the In_2Se_3 fills in the pits, coating the entire substrate uniformly and forming a conformal film. The 23 nm (not shown) sample is also conformably coated as well, with similar morphology as in Figure 2(c). On the other hand, samples of 2, 3, 5, and 8 nm nominal film thickness are distinct from the conformal case. In Figure 2(b), the film coverage of the 2 nm sample is shown (the morphologies of the 3, 5, and 8 nm films are similar and are not shown here). We observed that there is lighter contrast from the pits region compared to the bare pit sample (Figure 2(a)). This indicates that the contrast is not only from mass-thickness contrast, but also from Z (atomic number) contrast. The higher the Z number of the material is, the more electrons get scattered at high angles into the High Angle Annular Dark Field (HAADF) detector [12]. Since In_2Se_3 is heavier than Si, it should give a brighter contrast. In this sample, the pit region is relatively darker compared to the surface, which suggests that In_2Se_3 did not fill up the pits. For films with very thin nominal thickness, due to different interfacial energies between $\text{In}_2\text{Se}_3/\text{Si}(100)$ and $\text{In}_2\text{Se}_3/\text{Si}(111)$, materials deposited into the pits are very likely to be confined in there forming nanoclusters instead of conformal films. A schematic of film coverage on pits is also shown in Figure 2.

3.2. Phase Transition. The initial phase of the as-deposited In_2Se_3 is amorphous; thus, the diffraction pattern of the sample is a combination of halo amorphous rings from In_2Se_3 and diffraction spots from the Si substrate. Phase transition temperature is determined by the observation of single crystalline diffraction spots or polycrystalline diffraction rings appearing from crystalline In_2Se_3 as the sample is in situ heated. The sample temperature is first heated to around 90°C, stabilized, and then annealed for 3 minutes. If no phase transition is observed in the time period, the sample temperature is then increased in 10°C increments. The process was repeated until phase transition is observed. Figure 3 shows the crystallization temperatures (T_x) of the samples with different nominal film thickness. An increase in crystallization temperature is observed as the nominal film thickness decreases. Such crystallization behavior is also observed from the thin films $\text{Ge}_2\text{Sb}_2\text{Te}_5$, GeSb , and Sb_2Te reported in another group's work [13]. For the sample with nominal thickness of 2 nm which translates to a volume of 5.3 nm³, no crystallization was observed. Therefore, 5.3 nm³ is believed to be the scaling limit of In_2Se_3 . We speculate that the underlying physics of the scaling limit phenomenon is as follows. Thermodynamically, the driving force for crystallization is the reduction of the Gibbs free energy; that is, the amorphous phase is of higher energy which is at metastable state compared to the crystalline phase. However, for crystalline state In_2Se_3 , the surface atoms are disordered or have higher energy than in the bulk due to the dangling bonds they have. This energy increase will be negligible for a bulk material with large volume. But with reducing volume or increasing surface to volume ratio, the higher energy of the surface atoms will become dominant in the total energy of the system. That means when the volume decreases to a certain value, which is the scaling limit, the disorderliness or the free energy of crystalline state is comparable to that of the amorphous state;

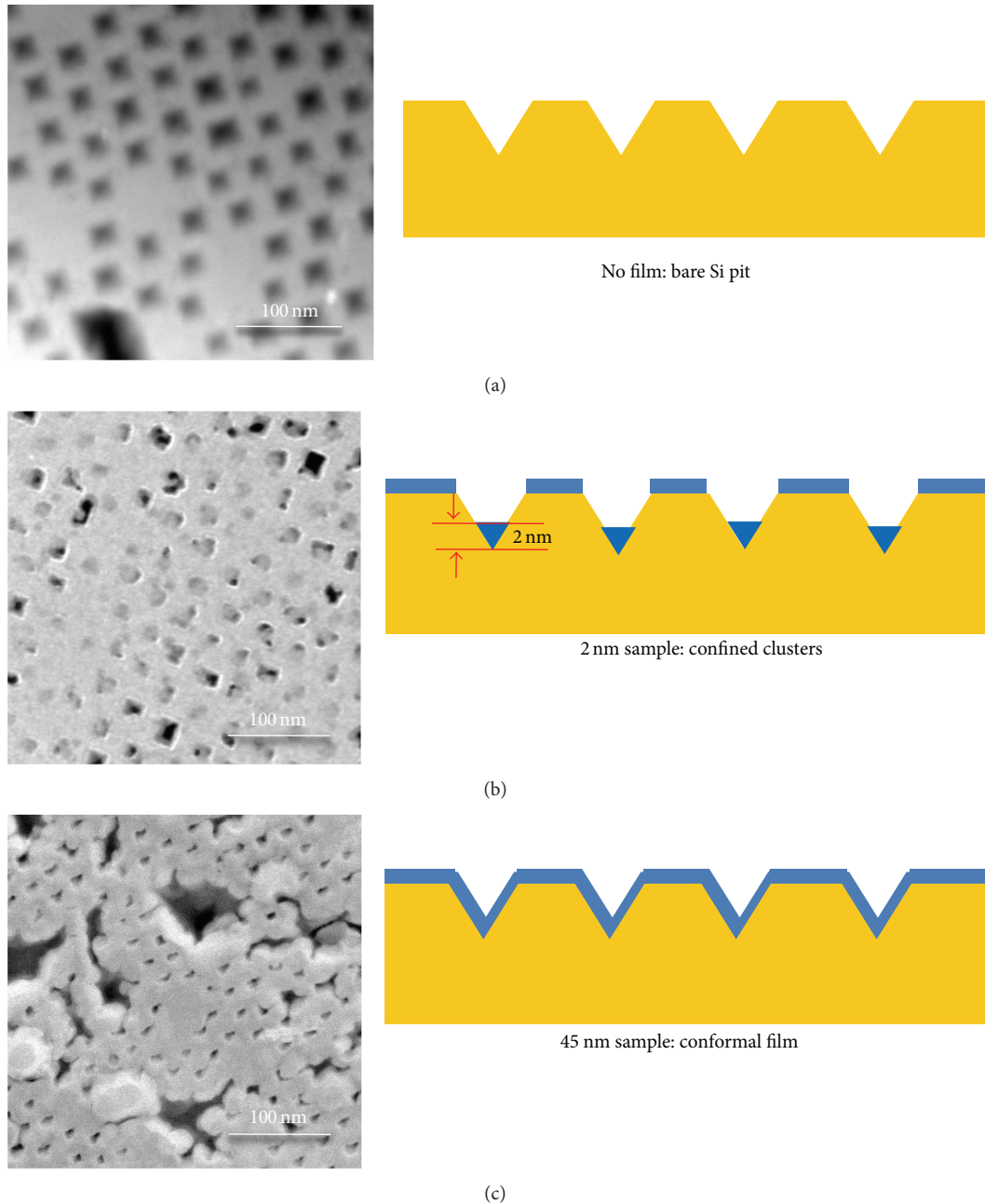


FIGURE 2: STEM images of (a) bare nanopit Si substrate and (b) 2 nm and (c) 45 nm In_2Se_3 deposited on Si nanopit substrate with cross section schematic of film coverage.

thus, the crystalline state diminishes. On the other hand, as we have already known from the working mechanism of In_2Se_3 phase transition, the crystallization temperature should be lower than the melting temperature. Therefore, the melting behavior of In_2Se_3 is also of interest as the crystallization temperature goes up with decreasing volume. The procedure for melting temperature measurement is similar to crystallization. The melting temperature is determined by the disappearance of polycrystalline diffraction rings. The sample is first heated to 280°C and then annealed for 3 minutes at the stabilized temperature. If no melting occurred, the sample

temperature is increased by 10°C . This process is repeated until melting is observed. As seen from Figure 4, the melting temperature (T_m) decreases as the nominal film thickness decreases. As the volume of In_2Se_3 scales down, the melting temperature drops while the crystallization temperature rises. The T_m/T_x ratio has dropped from 2.8 in bulk to 1.7 at 5 nm size. The melting temperature of the 2 nm nominal thickness sample cannot be measured because there were no polycrystalline diffraction rings observed throughout the entire heating process. This indicates that the decrease of melting temperature is also a potential cause for the scaling limit of In_2Se_3 .

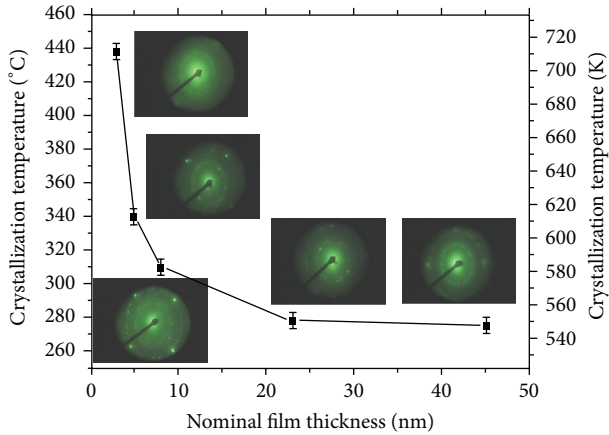


FIGURE 3: Crystallization temperature versus nominal film thickness of In_2Se_3 in nanopit substrate. Insets are diffraction pattern of the polycrystalline diffraction rings for each crystallization temperature.

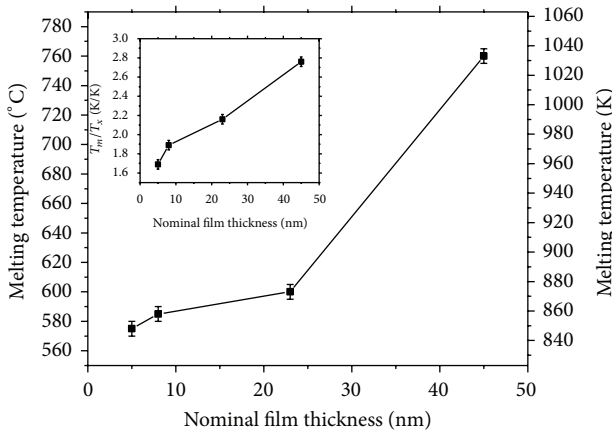


FIGURE 4: Melting temperature versus nominal film thickness of In_2Se_3 in nanopit substrate. Inset shows the ratio of T_m/T_x .

4. Conclusion

This study has shown that nanopit substrate is a unique pattern for nanosize PCM study. Film coverage on the nanopit substrate is not conformal when nominal film thickness of In_2Se_3 becomes very thin. 39% reduction of the ratio of T_m/T_x is measured with reducing volume of In_2Se_3 , and it is a possible cause for the elimination of phase transition. At 2 nm nominal film thickness, no crystallization is observed, which suggests that the corresponding volume of 5.3 nm^3 is the scaling limit of In_2Se_3 concluded from this study. The diminishing of the crystalline state is believed to be due to the fact that the surface disorderliness dominates for small volume materials.

Conflict of Interests

The authors declare that there is no conflict of interests regarding the publication of this paper.

Acknowledgments

This work was supported in part by FAME, one of the six centers of STARnet, a Semiconductor Research Corporation program sponsored by MARCO and DARPA. Y. H. Xie acknowledges the support from Alexander von Humboldt Foundation Research Award that made this research possible.

References

- [1] S. R. Ovshinsky, "Reversible electrical switching phenomena in disordered structures," *Physical Review Letters*, vol. 21, no. 20, pp. 1450–1453, 1968.
- [2] H.-S. P. Wong, S. Raoux, S. Kim et al., "Phase change memory," *Proceedings of the IEEE*, vol. 98, no. 12, pp. 2201–2227, 2010.
- [3] A. Redaelli, A. Pirovano, A. Benvenuti, and A. L. Lacaita, "Threshold switching and phase transition numerical models for phase change memory simulations," *Journal of Applied Physics*, vol. 103, no. 11, Article ID 111101, 2008.
- [4] G. W. Burr, M. J. Breitwisch, M. Franceschini et al., "Phase change memory technology," *Journal of Vacuum Science & Technology B*, vol. 28, no. 2, pp. 223–262, 2010.
- [5] G. E. Moore, "Cramming more components onto integrated circuits," *Electronics*, vol. 38, pp. 114–117, 1965.
- [6] M. Wuttig and N. Yamada, "Phase-change materials for rewritable data storage," *Nature Materials*, vol. 6, no. 11, pp. 824–832, 2007.
- [7] A. V. Kolobov, P. Fons, A. I. Frenkel, A. L. Ankudinov, J. Tomimaga, and T. Uruga, "Understanding the phase-change mechanism of rewritable optical media," *Nature Materials*, vol. 3, no. 10, pp. 703–708, 2004.
- [8] N. Yamada, E. Ohno, K. Nishiuchi, N. Akahira, and M. Takao, "Rapid-phase transitions of $\text{GeTe-Sb}_2\text{Te}_3$ pseudobinary amorphous thin films for an optical disk memory," *Journal of Applied Physics*, vol. 69, no. 5, pp. 2849–2856, 1991.
- [9] R. E. Simpson, M. Krbal, P. Fons et al., "Toward the ultimate limit of phase change in $\text{Ge}_2\text{Sb}_2\text{Te}_5$," *Nano Letters*, vol. 10, no. 2, pp. 414–419, 2010.
- [10] J. Y. Lee, K. Sun, B. Li, X. Wei, T. Russell, and Y.-H. Xie, "A method to fabricate a template with a long range ordered dense array of true nanometer scale pits," *IEEE Transactions on Nanotechnology*, vol. 10, no. 2, pp. 256–259, 2011.
- [11] K. Sun, W. Zhang, B. Li et al., "Field emission tip array fabrication utilizing geometrical hindrance in the oxidation of Si," *IEEE Transactions on Nanotechnology*, vol. 11, no. 5, pp. 999–1003, 2012.
- [12] D. B. Williams and C. B. Carter, *Transmission Electron Microscopy: A Textbook for Materials Science*, Springer, New York, NY, USA, 2009.
- [13] S. Raoux, J. L. Jordan-Sweet, and A. J. Kellock, "Crystallization properties of ultrathin phase change films," *Journal of Applied Physics*, vol. 103, no. 11, Article ID 114310, pp. 114310–114316, 2008.

Research Article

An Accurate Thermoviscoelastic Rheological Model for Ethylene Vinyl Acetate Based on Fractional Calculus

Marco Paggi¹ and Alberto Sapora²

¹IMT Institute for Advanced Studies Lucca, Piazza San Francesco 19, 55100 Lucca, Italy

²Department of Structural, Geotechnical and Building Engineering, Polytechnic University of Turin, Corso Duca degli Abruzzi 24, 10129 Torino, Italy

Correspondence should be addressed to Marco Paggi; marco.paggi@imtlucca.it

Received 18 November 2014; Revised 2 January 2015; Accepted 2 January 2015

Academic Editor: Sheng-Po Chang

Copyright © 2015 M. Paggi and A. Sapora. This is an open access article distributed under the Creative Commons Attribution License, which permits unrestricted use, distribution, and reproduction in any medium, provided the original work is properly cited.

The thermoviscoelastic rheological properties of ethylene vinyl acetate (EVA) used to embed solar cells have to be accurately described to assess the deformation and the stress state of photovoltaic (PV) modules and their durability. In the present work, considering the stress as dependent on a noninteger derivative of the strain, a two-parameter model is proposed to approximate the power-law relation between the relaxation modulus and time for a given temperature level. Experimental validation with EVA uniaxial relaxation data at different constant temperatures proves the great advantage of the proposed approach over classical rheological models based on exponential solutions.

1. Introduction

Ethylene vinyl acetate (EVA) is the most used material for encapsulating solar cells in photovoltaic (PV) modules due to its low cost, high transmittance of light, good thermal conduction, and long operating range. This polymer is used for binding the glass cover, the solar cells, and the backsheets together in order to realize the layered stack of a typical PV module [1, 2]. Moreover, EVA provides protection of cells and interconnections from moisture, foreign impurities, and mechanical damage. The provision of such properties makes it a vital component on which the performance of a PV module depends [3].

In this context, modeling accurately the thermoviscoelastic behavior of EVA over the whole thermal range used in applications, which varies from -40°C , the lowest temperature for standard qualification testing of PV modules [4], up to $+150^{\circ}\text{C}$, corresponding to the lamination temperature [5], is a crucial and not trivial task. The elastic modulus may vary up to three orders of magnitude depending on the temperature and for temperatures less than zero, it may vary up to one order of magnitude depending on the relaxation time [2, 6]. Eva constitutive behavior significantly influences

the stress and deformation states of solar cells [1, 2, 6–8]. It is responsible for the nonlinear variation of the gap between solar cells during temperature excursions experienced in the field, which may lead to the interconnection failure [9–13]. EVA is also subjected to degradation phenomena and discoloration due to aging [14–18] and, as shown very recently, its properties can have a role in the mechanism of backsheets delamination [19], influencing the toughness of the interface between backsheets and the polymer.

EVA shows a relaxation behavior of power-law type, as many other natural and artificial materials [20–23]. Classical rheological models used so far generally provide exponential-type relations and, in order to approximate a power-law trend, a huge number of elements (and thus of model parameters) should be taken into account. Generalized Maxwell models or Prony series have been usually proposed to fit EVA experimental relaxation curves and have been implemented in commercial finite element software like Abaqus, Ansys, or Comsol multiphysics as user defined elements. A Prony series with up to 100 Maxwell arms in parallel was considered in [6], whereas models with up to 32 arms were used in [14].

This gives rise to several drawbacks, including the fact that it is not always possible to provide a clear mechanical

meaning to all the parameters and that the numerical procedure for their identification is not trivial, being these subjected to several physical constraints [24].

On the other hand, power-law relations rise out naturally by assuming a material constitutive law of fractional type, that is, involving noninteger order derivatives of stress and/or strain [25, 26]. The ability of fractional calculus to model hereditary phenomena with long memory has now been widely accepted by the scientific community [27–29].

In the present work, a two-parameter element consisting of a fractional dashpot (or springpot) is considered to model the viscoelastic behavior of EVA. The aim is to determine a simple constitutive model of easy numerical implementation able to capture the material mechanical behavior at all temperatures and with only two free parameters to be identified. The fractional approach will be successfully applied to relaxation tests carried out on EVA samples at different constant temperatures ranging from -35°C to 139°C [6] and used to assess the evolution of the gap between solar cells [1, 9]. The advantages with respect to Prony series in terms of both accuracy and model parameters identification are proven.

The paper is organized as follows: classical rheological models are summarized in Section 2, while the proposed fractional approach is described in Section 3. Section 4 includes details on the numerical procedure to fit the model parameters, the comparison between experimental data and theoretical results and comments on the relevance of the proposed constitutive model for computational simulations on PV modules. Concluding remarks are given in Section 5.

2. Classical Rheological Models

Basic models in the classical rheology are herein briefly summarized, since they constitute the actual state-of-the-art modelling of the viscoelastic behavior of EVA.

2.1. Spring and Dashpot Elements. The material elastic behavior is classically represented in mechanics by a spring element, whose stress-strain (σ - ε) constitutive relation writes

$$\sigma(t) = E\varepsilon(t), \quad (1)$$

with E being the spring stiffness.

On the other hand, the limit case of a fluid viscous response is described by a dashpot element, whose constitutive law can be expressed:

$$\sigma(t) = \eta \frac{d\varepsilon(t)}{dt}, \quad (2)$$

where η is the dynamic viscosity.

Viscoelastic materials exhibit both elastic and viscous behaviors, which are then modeled by properly combining springs and dashpots. Since the viscoelastic constitutive equation will be expressed by using a relaxation-based formulation, it is now useful to introduce the relaxation modulus for the two elements considered so far. While for the spring it is simply $E(t) = E$, for the dashpot it takes the form $E(t) = \eta\delta(t)$, with $\delta(t)$ being the Dirac-function.

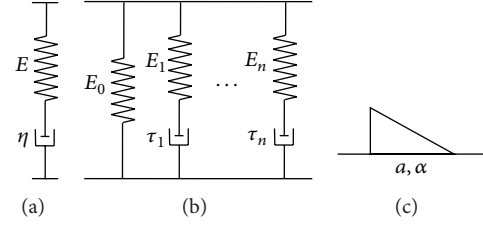


FIGURE 1: Maxwell model (a); generalized Maxwell model (b); Scott-Blair element or springpot (c).

2.2. Maxwell Model and Its Generalization. The Maxwell model consists of a spring and a dashpot in series (Figure 1(a)). Since the two elements are subjected to the same stress, while the total strain is the sum of two contributions—one of the spring and one of the dashpot, respectively—the constitutive relation is obtained by differentiating (1) and adding the result to (2):

$$\sigma(t) + \frac{\eta}{E} \frac{d\sigma(t)}{dt} = \eta \frac{d\varepsilon(t)}{dt}. \quad (3)$$

By introducing the relaxation time $\tau = \eta/E$, the corresponding relaxation function is

$$E(t) = E \exp\left(\frac{-t}{\tau}\right). \quad (4)$$

The Maxwell element is therefore based just on two parameters, E and η (or τ). Indeed, a more accurate but complicated model can be obtained by arranging n Maxwell elements (also called *arms*) in parallel, leading to the generalized model depicted in Figure 1(b). Note that an isolated spring with stiffness E_0 is also introduced, in order for the relaxation function to achieve an asymptotic value different from zero. This choice is supported by several experimental data available in the literature [10]. The function $E(t)$ takes the following form:

$$E(t) = E_0 + \sum_{i=1}^n E_i \exp\left(\frac{-t}{\tau_i}\right), \quad (5)$$

which is referred to as a Prony series [30]. The difficulties in fitting the related $2n + 1$ parameters will be discussed in Section 4.

3. A Rheological Model Based on Fractional Calculus

The fractional generalization of the models presented in Section 2 can be achieved by replacing the first-order derivative in (2) with the derivative of order $\alpha \in (0, 1)$ [27]. According to Caputo's definition, the α -derivative of a generic function f is given by [31]

$$\frac{d^\alpha f(x)}{dx^\alpha} = \frac{1}{\Gamma(1-\alpha)} \int_0^x \frac{f'(y)}{(x-y)^\alpha} dy, \quad (6)$$

where Γ is Euler's Gamma function. By reminding that $\Gamma(0^+) = +\infty$ and $\Gamma(1) = 1$, according to (6) the function f

itself is recovered for $\alpha = 0$, while the first-order classical derivative is obtained for $\alpha = 1$. For quiescent systems at $x = 0$, the definition (6) coincides with that provided by Riemann and Liouville [31]. We will thus refer with the same symbol to both definitions, without losing of generality.

To substitute the first-order derivative with the derivative of order $\alpha \in (0, 1)$ is equivalent, from a mechanical point of view, to replace a dashpot with a fractional dashpot (or *springpot*) of order α . The simplest fractional element (also known as Scott-Blair element) consists of a single springpot (Figure 1(c)). The constitutive equation writes ($\alpha \in (0, 1)$)

$$\sigma(t) = a \frac{d^\alpha \varepsilon(t)}{dt^\alpha}. \quad (7)$$

Equation (7) tends to (1), that is, the classic spring element, for $\alpha \rightarrow 0^+$, while it provides (2), that is, the dashpot, for $\alpha \rightarrow 1$. As α varies, the mechanical meaning of the parameter a (with SI units Pa s^α) changes accordingly, passing from a stiffness ($\alpha = 0$) to a viscosity ($\alpha = 1$). For this element, the relaxation modulus $E(t)$ assumes the following power-law form:

$$E(t) = a \frac{t^{-\alpha}}{\Gamma(1-\alpha)}. \quad (8)$$

Equation (8) will be sufficient for the purposes of the present study, although the singular nature of the power law's relationship, that is, infinite modulus at time zero, is inappropriate for the goal of portraying the phenomenon at times close to the onset of the strain. This point was deeply discussed in [32].

The analysis of fractional viscoelastic models is limited to what is presented above, for the sake of simplicity. Interested readers can refer to [27, 33] for a deeper insight on this topic. It is however important to realize that the substitution of a dashpot by a springpot involves an additional parameter in the modeling analysis, for a total of two parameters to be identified.

4. Experimental Validation of the Proposed Approach for EVA and Critical Comparison with Classical Methods

Several experimental tests on viscoelastic materials show relaxation functions with a power-law behavior [20, 28]. This is also the case of EVA; see the recent experimental campaign in [6]. If a classical rheological model is used, since an exponential function (4) is obtained through the Maxwell element, this implies the need of implementing generalized Prony series (5). Indeed, several drawbacks emerge from this approach. First of all, it is not always clear what the physical meaning of all the arms is. Secondly, several restrictions must be imposed for physically realistic materials; for example, the coefficients have to be strictly positive [34]. The fitting algorithm results therefore into a constrained least squares problem, and sophisticated numerical methods must be implemented; see, for example, [24, 30].

Eventually, notice that a creep experiment is usually easier to perform than a relaxation one, so most of the experimental

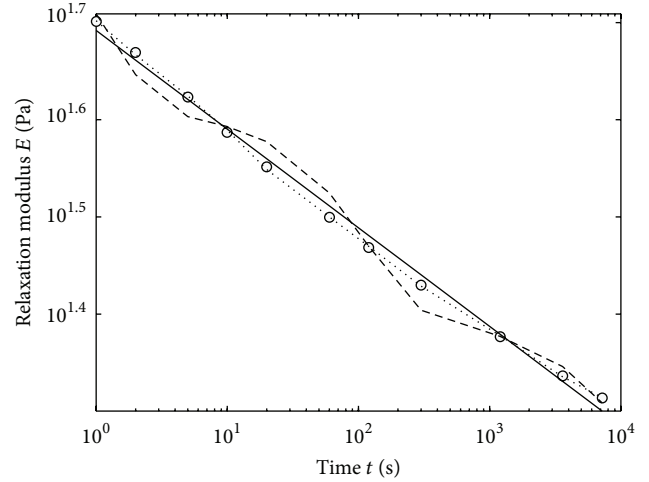


FIGURE 2: Relaxation modulus versus time for EVA at 60°C: experimental data (circles), predictions by the generalized Maxwell model with 3 arms (dashed line), by the generalized Maxwell model with 5 arms (dotted line), and by the springpot model based on fractional calculus (continuous line).

data are available in the form of creep compliance versus time. Since there is no known closed form for the (creep) compliance in terms of the coefficients of the Prony series, once the creep data are known, it is not straightforward at all to get the coefficients of the (relaxation) Prony series.

On the other hand, the fractional model discussed in Section 3 is more efficient to handle, since a power-law relaxation modulus (8) comes naturally from the constitutive law (7). Furthermore, only two coefficients (a, α) need to be fitted. Observe also that fractional operators have a simple definition in terms of the Laplace transforms, so it is not difficult to obtain the creep compliance starting from the relaxation modulus (and *vice versa*), with these functions being strictly related to each other in the Laplace domain [20, 25].

Generalized Maxwell models and the proposed fractional element are now applied to the results of the uniaxial relaxation tests on EVA specimens carried out in [6] at different temperatures. The reader is referred to [6, 10] for a description on the testing procedure, which is standard, and it is not reported here to avoid duplication of information.

Let us start by considering the relaxation data of EVA tested at 60°C (Figure 2). Predictions according to two different generalized Maxwell models, one with 3 arms ($n = 3$) and one with 5 arms ($n = 5$), are firstly considered. For the implementation, the values τ_i (s) are chosen equidistant to cover the whole time range; that is, $\tau = (10^0, 10^2, 10^4)$ for $n = 3$ and $\tau = (10^0, 10^1, 10^2, 10^3, 10^4)$ for $n = 5$. Given the times τ_i , the remaining $n+1$ coefficients E_j (Pa) ($j = 0, \dots, n$) are obtained by fitting the Prony series to the experimental curve, resulting in $E = (0.6557, 0.3541, 0.3548, 0.3216)$ for $n = 3$ and $E = (0.7774, 0.1253, 0.1744, 0.1888, 0.1746, 0.1052)$ for $n = 5$.

A similar fitting is carried out for the fractional model (8), where a procedure to evaluate the coefficients of a nonlinear

TABLE 1: Identified parameters of the proposed rheological model based on fractional calculus used to fit experimental uniaxial relaxation tests at different temperatures.

Temperature (°C)	α	a (Pa s $^\alpha$)	Mean absolute percentage error (%)
-35	0.22600	814.7	3.728
-28	0.16810	182.7	2.702
-18	0.10150	52.63	1.823
0	0.05566	23.55	1.851
20	0.04227	11.04	0.3044
40	0.07417	4.668	2.977
49	0.08634	4.116	5.467
60	0.06542	1.544	0.9898
80	0.05117	1.049	1.110
100	0.04179	0.9276	0.8064
119	0.03610	0.7965	0.9627
139	0.03311	0.8228	0.3811

regression function, using a least squares estimate, is adopted. The identified parameters are $a = 1.544$ Pa s $^\alpha$, $\alpha = 0.06542$ (Table 1).

A comparison between the generalized Maxwell models with 3 or 5 arms, the proposed rheological model based on fractional calculus, and the experimental results is shown in Figure 2 on a bilogarithmic plane. The generalized Maxwell model with 3 arms, often available in the majority of finite element programs, like the Finite Element Analysis Program (FEAP) by Zienkiewicz and Taylor, without the need of implementing new user element subroutines, generates a wavy curve with very low accuracy. More accurate predictions are achieved by increasing n up to 5, but with the necessity of identifying 6 parameters. The simpler 2-parameter springpot model proposed in this work, leading to a straight line with negative slope $-\alpha$ and intercept a , is indeed reasonably accurate and simple.

With the efficiency of the proposed approach over the classic one being proven, the identification procedure for the fractional model is repeated here for relaxation data related to different testing temperatures; see Figure 3. The identified values (a, α) are collected in Table 1, together with the mean absolute percentage error of the correlations, which is always very low.

It is remarkable to note here that this further identification procedure is not usually done in the framework of the classic approaches which rely on the time-temperature superposition principle [35]. It states that the material response at a given temperature can be related to that at another temperature by a suitable change in time-scale. Actually, when this principle is checked against experimental results [14], its validity for EVA was found to be questionable and leading to poor predictions if tacitly assumed to be valid (see the comparison in Figure 4 between the actual shift factor deduced by experiments and the Williams-Landel-Ferry (WLF) theoretically expected shift function). This behavior is imputable to a modification of the EVA

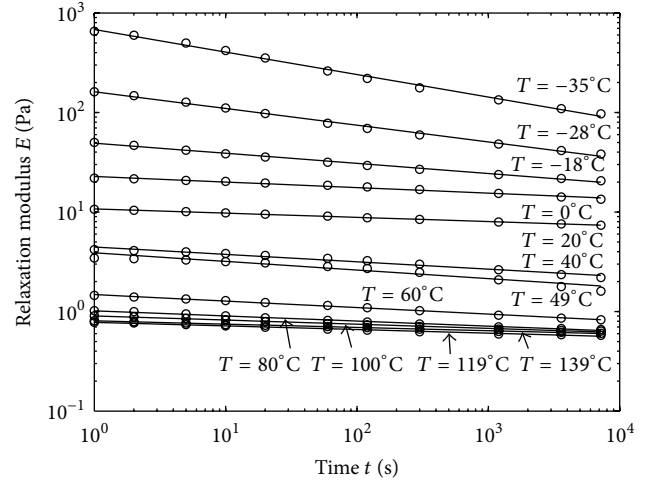


FIGURE 3: Relaxation modulus versus time for EVA specimens at different temperatures: experimental data (circles) and predictions by the springpot model based on fractional calculus (continuous lines).

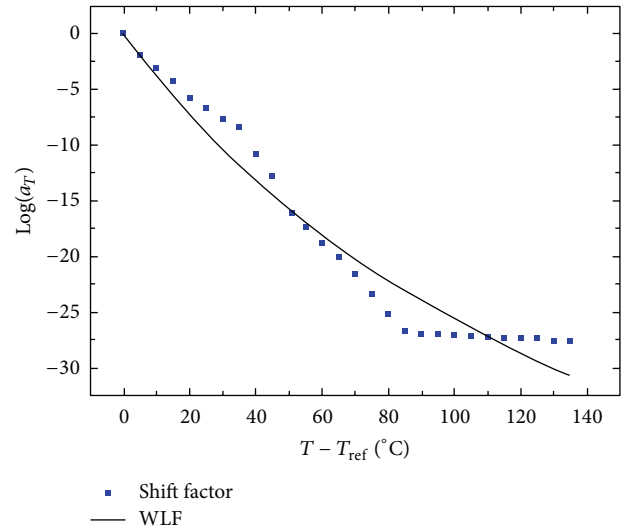


FIGURE 4: Comparison between the actual shift factor determined from EVA experiments (dots) and the expected Williams-Landel-Ferry WLF shift function (solid curve) for the application of the time-temperature superposition principle (adapted from [14]). The reference temperature is $T_{ref} = -20^\circ\text{C}$.

microstructure due to melting of the crystalline part, as reported in [14]. Therefore, the use of the classical principle of time-temperature superposition should not be applied to model the thermoviscoelastic behavior of EVA over the whole temperature range. In spite of this evidence, the problem was left unresolved up to now in the framework of a Prony series representation. In fact, for a model with $n = 25$ arms that was deemed necessary in [14], it would be necessary to determine $n + 1 = 26$ fitting parameters for each testing temperature and then construct a look-up table from where different model parameters can be picked up during numerical simulations. Clearly, this leads to a complex numerical implementation

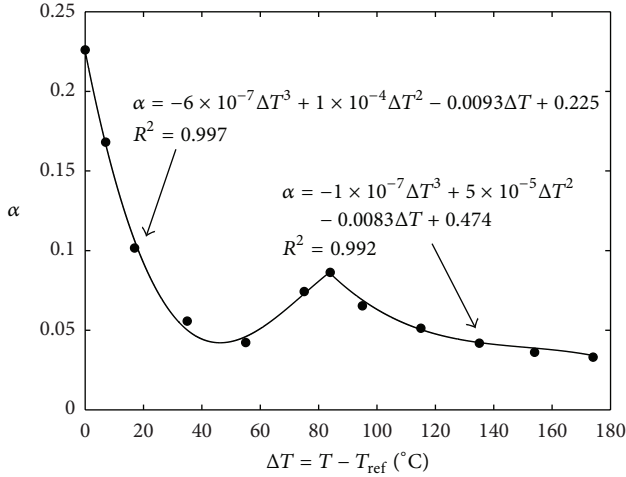


FIGURE 5: Variation of the identified model parameter α versus temperature. Two different correlations are suggested due to a modification in the material microstructure of EVA for $\Delta T \sim 80^\circ\text{C}$. The reference temperature is $T_{\text{ref}} = -35^\circ\text{C}$. R^2 represents the coefficient of determination of the best-fit.

that cannot be handled by commercial finite element software. Moreover, interpolation between Prony series approximations corresponding to different temperatures is not an obvious procedure as well.

By using the proposed approach, only 2 model parameters have to be determined for each testing temperature, which makes it possible to determine useful correlations of much easier implementation in finite element software. In particular, by plotting the exponent α versus $\Delta T = T - T_{\text{ref}}$ ($T_{\text{ref}} = -35^\circ\text{C}$) in Figure 5 (using the data collected in Table 1), we note that the transition in the EVA microstructure due to melting of the crystalline phase is well evidenced by this method due to the deviation from a single trend and it occurs at $\Delta T \sim 80^\circ\text{C}$, consistently with that reported in [14] (see also [36]). Therefore, within the present approach, an accurate modelling of the rheological behavior of EVA suggests the use of the following two distinct correlations for the parameter $\alpha = \alpha(T)$, depending on temperature:

$$\alpha(T) = \begin{cases} -6 \times 10^{-7} \Delta T^3 + 1 \times 10^{-4} \Delta T^2 - 0.0093 \Delta T + 0.225, & \Delta T \leq 80^\circ\text{C}, \\ -1 \times 10^{-7} \Delta T^3 + 5 \times 10^{-5} \Delta T^2 - 0.0083 \Delta T + 0.474, & \Delta T > 80^\circ\text{C}. \end{cases} \quad (9)$$

A similar analysis can be performed for the coefficient $a = a(T)$, which generally decreases by increasing temperature; see Table 1. This physically implies that the stiffness of the material increases as temperature decreases, consistently with the experimental evidence.

Therefore, the limited amount of identified data in Table 1 or, alternatively, correlations of the type (9) can be efficiently passed as input to a new user material element based on the proposed approach for accurate finite element simulations, without the need of relying on the time-temperature superposition principle. The implementation of the new constitutive

equation (7) in the finite element method [37] via a user defined material will require the numerical approximation of the fractional derivative (6). Starting from the simple Grunwald-Letnikov definition, different algorithms based on fractional finite differences can be considered [38] and their comparison is left for further research.

The rheological model proposed in the present work can be very useful for improving the accuracy of numerical simulations of coupled problems in multiphysics whenever time and temperature are varying at the same time [1, 2]. Examples of this type where the proposed methodology is expected to be beneficial are the simulation of the process of cooling down of PV modules to the ambient temperature from the lamination temperature in order to assess residual stresses; the simulation of aging of PV modules and crack propagation in Silicon during standard tests inside a climate chamber; temperature degradation of EVA in case of hot spots or defects [39, 40]. In all of these cases, in fact, the temperature is varying with position and time inside the PV module and an accurate instantaneous value of EVA Young's modulus has to be used in each Gauss point and at each integration time step.

5. Conclusions

In this study, a rheological constitutive relationship based on fractional calculus has been proposed to model the viscoelastic behavior of EVA. The formulation involves just two parameters, the identification of which is much easier to be made than classical Prony series related to standard approaches. The relaxation modulus, as function of time, has been evaluated over the whole temperature range important in PV applications: theoretical results have been compared with experimental data, showing a very satisfactory agreement.

The present modeling allows bypassing the problem of inapplicability of the time-temperature superposition principle for EVA noticed in the literature, since a very limited number of identified model parameters (or just correlations, see (9)) can be passed as input to a user defined material subroutine for finite element software.

Conflict of Interests

The authors declare that there is no conflict of interests regarding the publication of this paper.

Acknowledgments

Professor Paggi would like to acknowledge funding from the European Research Council under the European Union's Seventh Framework Programme (FP/2007–2013)/ERC Grant Agreement no. 306622 (ERC Starting Grant "Multi-Field and Multi-Scale Computational Approach to Design and Durability of PhotoVoltaic Modules" (CA2PVM)). The research activity by Dr. Sabora has been supported by the Italian Ministry of Education, University and Research in the project FIRB 2010 Future in Research "Structural Mechanics Models

for Renewable Energy Applications” (RBFRI07AKG), which is also gratefully acknowledged.

References

- [1] M. Paggi, S. Kajari-Schröder, and U. Eitner, “Thermomechanical deformations in photovoltaic laminates,” *Journal of Strain Analysis for Engineering Design*, vol. 46, no. 8, pp. 772–782, 2011.
- [2] M. Paggi, M. Corrado, and M. A. Rodriguez, “A multi-physics and multi-scale numerical approach to microcracking and power-loss in photovoltaic modules,” *Composite Structures*, vol. 95, pp. 630–638, 2013.
- [3] O. Hasan and A. F. M. Arif, “Performance and life prediction model for photovoltaic modules: effect of encapsulant constitutive behavior,” *Solar Energy Materials and Solar Cells*, vol. 122, pp. 75–87, 2014.
- [4] K. Agroui, A. Maallemi, M. Boumaour, G. Collins, and M. Salama, “Thermal stability of slow and fast cure EVA encapsulant material for photovoltaic module manufacturing process,” *Solar Energy Materials and Solar Cells*, vol. 90, no. 15, pp. 2509–2514, 2006.
- [5] International Electrotechnical Commission, “Crystalline silicon terrestrial photovoltaic (PV) modules—design qualification and type approval,” International Standard IEC 61215:2006, 2006.
- [6] U. Eitner, *Thermomechanics of photovoltaic modules [Ph.D. thesis]*, Zentrum für Ingenieurwissenschaften der Martin-Luther-Universität Halle-Wittenberg, 2011.
- [7] S. Dietrich, M. Pander, M. Sander, S. H. Schulze, and M. Ebert, “Mechanical and thermo-mechanical assessment of encapsulated solar cells by finite-element-simulation,” in *Reliability of Photovoltaic Cells, Modules, Components, and Systems III*, vol. 7773 of *Proceedings of SPIE*, August 2010.
- [8] M. Koehl, M. Heck, and S. Wiesmeier, “Modelling of conditions for accelerated lifetime testing of Humidity impact on PV-modules based on monitoring of climatic data,” *Solar Energy Materials and Solar Cells*, vol. 99, pp. 282–291, 2012.
- [9] U. Eitner, M. Köntges, and R. Brendel, “Use of digital image correlation technique to determine thermomechanical deformations in photovoltaic laminates: measurements and accuracy,” *Solar Energy Materials and Solar Cells*, vol. 94, no. 8, pp. 1346–1351, 2010.
- [10] U. Eitner, S. Kajari-Schröder, M. Köntges, and R. Brendel, “Non-linear mechanical properties of ethylene-vinyl acetate (EVA) and its relevance to thermomechanics of photovoltaic modules,” in *Proceedings of the 25th European Conference on Photovoltaic Solar Energy*, pp. 4366–4368, 2010.
- [11] J. Schlothauer, S. Jungwirth, M. Köhl, and B. Röder, “Degradation of the encapsulant polymer in outdoor weathered photovoltaic modules: spatially resolved inspection of EVA ageing by fluorescence and correlation to electroluminescence,” *Solar Energy Materials & Solar Cells*, vol. 102, pp. 75–85, 2012.
- [12] A. Saporita and M. Paggi, “A coupled cohesive zone model for transient analysis of thermoelastic interface debonding,” *Computational Mechanics*, vol. 53, no. 4, pp. 845–857, 2014.
- [13] F. J. Pern, “Factors that affect the EVA encapsulant discoloration rate upon accelerated exposure,” *Solar Energy Materials and Solar Cells*, vol. 41–42, pp. 587–615, 1996.
- [14] M. Pander, S. Dietrich, S.-H. Schulze, U. Eitner, and M. Ebert, “Thermo-mechanical assessment of solar cell displacement with respect to the viscoelastic behaviour of the encapsulant,” in *Proceedings of the 12th International Conference on Thermal, Mechanical and Multi-Physics Simulation and Experiments in Microelectronics and Microsystems (EuroSimE '11)*, pp. 1–6, Linz, Austria, April 2011.
- [15] E. Kaplani, “Detection of degradation effects in field-aged c-Si solar cells through IR thermography and digital image processing,” *International Journal of Photoenergy*, vol. 2012, Article ID 396792, 11 pages, 2012.
- [16] N. C. Park, W. W. Oh, and D. H. Kim, “Effect of temperature and humidity on the degradation rate of multicrystalline silicon photovoltaic module,” *International Journal of Photoenergy*, vol. 2013, Article ID 925280, 9 pages, 2013.
- [17] T. Kojima and T. Yanagisawa, “The evaluation of accelerated test for degradation a stacked a-Si solar cell and EVA films,” *Solar Energy Materials and Solar Cells*, vol. 81, no. 1, pp. 119–123, 2004.
- [18] D. Berman and D. Faïman, “EVA browning and the time-dependence of I-V curve parameters on PV modules with and without mirror-enhancement in a desert environment,” *Solar Energy Materials and Solar Cells*, vol. 45, no. 4, pp. 401–412, 1997.
- [19] F. D. Novoa, D. C. Miller, and R. H. Dauskardt, “Environmental mechanisms of debonding in photovoltaic backsheets,” *Solar Energy Materials and Solar Cells*, vol. 120, part A, pp. 87–93, 2014.
- [20] P. G. Nutting, “A new general law of deformation,” *Journal of the Franklin Institute*, vol. 191, no. 5, pp. 679–685, 1921.
- [21] R. Hilfer, *Fractional Calculus in Physics*, World Scientific, Singapore, 2000.
- [22] R. L. Magin, *Fractional Calculus in Bioengineering*, Begel House, Redding, Calif, USA, 2006.
- [23] J. T. Machado, V. Kiryakova, and F. Mainardi, “Recent history of fractional calculus,” *Communications in Nonlinear Science and Numerical Simulation*, vol. 16, no. 3, pp. 1140–1153, 2011.
- [24] J. Sorvari and M. Malinen, “On the direct estimation of creep and relaxation functions,” *Mechanics of Time-Dependent Materials*, vol. 11, no. 2, pp. 143–157, 2007.
- [25] G. Samko, A. A. Kilbas, and O. I. Marichev, *Fractional Integrals and Derivatives*, Gordon and Breach, Amsterdam, The Netherlands, 2000.
- [26] H. Schiessel, R. Metzler, A. Blumen, and T. F. Nonnenmacher, “Generalized viscoelastic models: their fractional equations with solutions,” *Journal of Physics A: General Physics*, vol. 28, no. 23, pp. 6567–6584, 1995.
- [27] F. Mainardi, *Fractional Calculus and Waves in Linear Viscoelasticity. An Introduction to Mathematical Models*, Imperial College Press, London, UK, 2010.
- [28] M. di Paola, A. Pirrotta, and A. Valenza, “Visco-elastic behavior through fractional calculus: an easier method for best fitting experimental results,” *Mechanics of Materials*, vol. 43, no. 12, pp. 799–806, 2011.
- [29] M. di Paola, F. P. Pinnola, and M. Zingales, “A discrete mechanical model of fractional hereditary materials,” *Meccanica*, vol. 48, no. 7, pp. 1573–1586, 2013.
- [30] N. W. Tschoegl, *The Phenomenological Theory of Linear Viscoelastic Behavior: An Introduction*, Springer, Berlin, Germany, 1989.
- [31] I. Podlubny, *Fractional Differential Equations*, vol. 198 of *Mathematics in Science and Engineering*, Academic Press, San Diego, Calif, USA, 1999.
- [32] R. L. Bagley, “Power law and fractional calculus model of viscoelasticity,” *AIAA Journal*, vol. 27, no. 10, pp. 1412–1417, 1989.

- [33] A. Carpinteri and F. Mainardi, *Fractals and Fractional Calculus in Continuum Mechanics*, Springer, Wien, Germany, 1997.
- [34] R. D. Bradshaw and L. C. Brinson, "A sign control method for fitting and interconverting material functions for linearly viscoelastic solids," *Mechanics of Time-Dependent Materials*, vol. 1, no. 1, pp. 85–108, 1997.
- [35] Y. Eom, L. Boogh, V. Michaud, P. Sunderland, and J.-A. Manson, "Time-cure-temperature superposition for the prediction of instantaneous viscoelastic properties during cure," *Polymer Engineering and Science*, vol. 40, no. 6, pp. 1281–1292, 2000.
- [36] W. Stark and M. Jaunich, "Investigation of Ethylene/Vinyl Acetate Copolymer (EVA) by thermal analysis DSC and DMA," *Polymer Testing*, vol. 30, no. 2, pp. 236–242, 2011.
- [37] S. Müller, M. Kästner, J. Brummund, and V. Ulbricht, "On the numerical handling of fractional viscoelastic material models in a FE analysis," *Computational Mechanics*, vol. 51, no. 6, pp. 999–1012, 2013.
- [38] K. B. Oldham and J. Spanier, *The Fractional Calculus*, Academic Press, New York, NY, USA, 1974.
- [39] M. Simon and E. L. Meyer, "Detection and analysis of hot-spot formation in solar cells," *Solar Energy Materials and Solar Cells*, vol. 94, no. 2, pp. 106–113, 2010.
- [40] M. Paggi and A. Sapore, "Numerical modelling of microcracking in PV modules induced by thermo-mechanical loads," *Energy Procedia*, vol. 38, pp. 506–515, 2013.

Research Article

Optical Properties of Indium Doped ZnO Nanowires

Tsung-Shine Ko,¹ Sin-Liang Ou,² Kuo-Sheng Kao,³ Tz-Min Yang,² and Der-Yuh Lin¹

¹Department of Electronic Engineering, National Changhua University of Education, No. 1, Jin-De Road, Changhua 500, Taiwan

²Department of Materials Science and Engineering, National Chung Hsing University, Taichung 40227, Taiwan

³Department of Computer and Communication, SHU-TE University, Kaohsiung 824, Taiwan

Correspondence should be addressed to Der-Yuh Lin; dylin@cc.ncue.edu.tw

Received 17 December 2014; Revised 9 February 2015; Accepted 10 February 2015

Academic Editor: Shyh-Jer Huang

Copyright © 2015 Tsung-Shine Ko et al. This is an open access article distributed under the Creative Commons Attribution License, which permits unrestricted use, distribution, and reproduction in any medium, provided the original work is properly cited.

We report the synthesis of the ZnO nanowires (NWs) with different indium concentrations by using the thermal evaporation method. The gold nanoparticles were used as the catalyst and were dispersed on the silicon wafer to facilitate the growth of the ZnO NWs. High resolution transmission electron microscopy confirms that the ZnO NWs growth relied on vapor-liquid-solid mechanism and energy dispersion spectrum detects the atomic percentages of indium in ZnO NWs. Scanning electron microscopy shows that the diameters of pure ZnO NWs range from 20 to 30 nm and the diameters of ZnO:In were increased to 50–80 nm with increasing indium doping level. X-ray diffraction results point out that the crystal quality of the ZnO NWs was worse with doping higher indium concentration. Photoluminescence (PL) study of the ZnO NWs exhibited main photoemission at 380 nm due to the recombination of excitons in near-band-edge (NBE). In addition, PL results also indicate the slightly blue shift and PL intensity decreasing of NBE emission from the ZnO NWs with higher indium concentrations could be attributed to more donor-induced trap center generations.

1. Introduction

Zinc oxide (ZnO) is one of the most favorable materials for blue/UV-associated optoelectronic devices and exciton-related device applications due to a wide band gap (3.37 eV) at room temperature and a large excitonic binding energy (60 meV) in comparison with GaN (28 meV) [1]. In recent, one-dimensional semiconductors have attracted much attention for nanoscale optoelectronic devices such as field effect transistors (FETs) [2, 3], gas sensors [4, 5], lasers [6], and photovoltaic applications [7]. In general, doping in wide band gap semiconductors often causes dramatic changes in the electric and optical properties. The conduction of transparent ZnO films could increase with cationic doping of group III elements, such as B, Al, Ga, and In. [8]. Among these ZnO with different dopants, In-doped ZnO films show similar electrical conductivity and better transparency in both the visible and IR regions compared to indium tin oxide. Thus, ZnO:In can be widely used as transparent conductors in optoelectronic applications [9, 10]. ZnO exhibits n-type semiconducting behavior due to native defects including Zn interstitials, oxygen vacancies,

or hydrogen interstitials. This makes it difficult to understand the main effect of additional dopants in terms of the structure and optoelectric properties of ZnO. Typically, ZnO doped with indium (>1%) wire-like (wires, belts, and rods) nanostructures were synthesized by thermal evaporation [11] and sol-gel [12] methods, recently. Despite many literatures having revealed main material properties of ZnO, however, the reports related to ZnO wire-like nanostructures with low indium doping concentration are still few and limited. In this paper, we successfully synthesized ZnO:In nanowires (NWs) with different indium doping concentration for comparison using gold nanoparticles as catalyst coated on Si substrates. The influence of the indium concentration on structural and optical properties of ZnO and ZnO:In NWs were investigated by scanning electron microscopy (SEM), transmission electron microscopy (TEM), X-ray diffraction (XRD), energy dispersive spectrometry (EDS), selected area electron diffraction (SAED), and photoluminescence (PL). A series of experiments revealed not only growth mechanism but also analyzed main exciton behavior for the ZnO NWs with different indium doping concentrations.

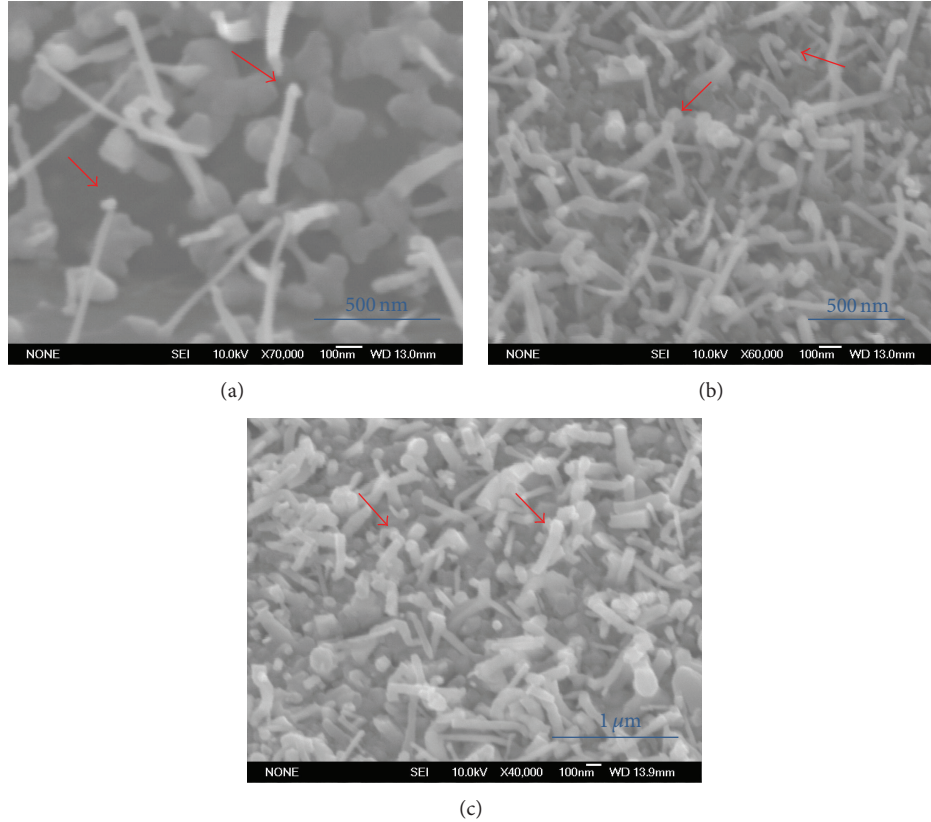


FIGURE 1: SEM images of ZnO:In NWs with different indium concentrations (a) undoped, (b) 0.86%, and (c) 0.95%. The red arrows point out the nanoparticles.

2. Experiments

P-type (001) oriented silicon wafers were prepared as substrates. Gold nanoparticles were produced by chemical reduction of gold tetrahydrate (HAuCl_4) with sodium citrate and then spread onto a native oxide coated silicon wafer with a self-assembled monolayer of 3-aminopropyltrimethoxysilane as adhesion layer. The width and density of gold nanoparticles are 10–20 nm and $6 \times 10^8 \text{ cm}^{-2}$ examined by scanning electron microscopy (SEM) images. A two-zone vacuum furnace was used for the growth of ZnO and ZnO:In NWs. 1.350 g zinc balls mixed with 0, 0.120, and 0.240 g indium balls, respectively, were positioned upstream in the vacuum furnace for providing vapor sources, while the substrates were placed downstream for the condensation of materials. Oxygen flowed through the system with a flow rate of 150 sccm used as reactive gas. During the growth, the temperatures elevated to 1050°C for sources and 700°C for sample, and the system pressure was kept at about 0.1 torr. SEM (JEOL, JSM 6500F) and TEM (JEOL, JEM 2010G, operating at 200 kV) were measured to investigate the morphologies and microstructures of the samples. For the TEM investigation, the samples should be further treated. We put the samples into a methanol solution and then performed the ultrasonic treatment. After this process for 1–2 minutes, the ZnO NWs were separated from the substrate. Subsequently, a drop of the suspension on a holey carbon film supported by

a 3-mm-diameter copper mesh was dried in air. Finally, the sample can be fixed at the TEM holder for microstructural observation. The crystal structure and phase purity were characterized by XRD measurements with $\text{Cu K}\alpha$ as the radiation source and SAED patterns affiliated to the TEM. The chemical compositions were examined by EDS attached to the TEM. PL spectra were performed at room temperature by using TRIAX-320 spectrometer equipped with a 25 mW He-Cd laser with the wavelength of 325 nm.

3. Results and Discussion

The morphologies and microstructures of the as-grown materials were characterized and analyzed by SEM. Figure 1 shows the SEM images of the ZnO (a) and ZnO:In (b) (c) NWs deposited on the gold nanoparticles coated Si substrates. The diameters of pure ZnO NWs range from 20 to 30 nm and the diameters of ZnO:In with different indium doping level were in the range of 20–50 and 20–80 nm, respectively. Also, the lengths of all the ZnO and ZnO:In were about several hundred nanometers. Apparently the incorporation of indium could influence the diameter of ZnO:In NWs. Except the wire-like structure observed from SEM, some unknown nanoparticles could be found on the top of NWs which are pointed out by red arrowheads in Figures 1(a)–1(c), suggesting that they act as catalyst in the growth process of

NWs. This feature could be further confirmed by using TEM and EDS measurements.

XRD diffraction patterns in theta-2theta geometry have been measured for examining the crystal quality and phase purity of the as-deposited materials which is shown in Figure 2. No diffraction peaks of indium or other impurities phases were revealed in any of our samples from XRD results. All the diffraction peaks in XRD spectra are corresponding to the ZnO crystal faces and the intensity of the (002) peak is much stronger than other ZnO peaks in the three of our samples, indicating the (002) crystal face might be the primary face of the NWs and the doping with small amount of indium did not affect the (002) orientation. The intensity and full-width half-maximum (FWHM) of the diffraction peaks, measures of crystal quality, in XRD patterns decreases and increases as the function of indium content, respectively. The degradation in crystal quality may be interpreted as the local disorder and lattice distortion due to the substitution of a zinc atom by an indium atom.

TEM, SAED, and EDS measurements were carried out to obtain more detailed structure and composition characterization of the individual NW. It was found that well NW structures with diameter of about 30 nm and a nanoparticle capped at its top in our TEM observations shown in Figures 3(a), 3(b), and 3(c). The SAED patterns of these three samples were also exhibited in Figures 3(a), 3(b), and 3(c). The planes of some diffraction dots were analyzed and marked; meanwhile, the zone axes of these samples were all identified to [001]. The EDS analysis indicates that the nanoparticles consisted mainly of gold and a small quantity of zinc, indium, and oxygen elements, while the stem of the NWs composed of only zinc, indium, and oxygen. The representative EDS spectra of the stem and tip part from ZnO:In NWs are shown in Figures 4(a) and 4(b). Through the measurement of EDS, the atomic percentages of indium were detected to be 0, 0.86, and 0.95 at. % in ZnO NWs for samples prepared with 0, 0.120, and 0.240 g indium. Since the vapor pressure is about 8×10^{-2} atm for Zn and 7×10^{-8} atm for In at 700°C in sample area, the huge difference of Zn/In mole ratio between the sources and the products in our experiment may be owing to a large discrepancy of vapor pressure between the two elements [13]. The vapor-liquid-solid (VLS) growth mechanism which was first proposed by Wanger and Ellis [14] for the growth of silicon whisker has been widely used in the synthesis of wire-like nanostructures, such as Si, GaN, ZnO, and In_2O_3 recently. According to the VLS process, two significant characteristics of the nanostructures will be mentioned. First, the presence of metal particles located at the growth fronts is demanded, which act as catalytic sites. Second, the dimension of the nanostructure is usually determined by the size of metal particle since the longitudinal growths of nanostructures only take place on the interface of metal particle. Both two features are in agreement with our results obtained from SEM and TEM images, which were considered as the evidence for the growth of VLS mechanism. In addition, the size of gold nanoparticles, before and after the growth of NWs, became larger which may result from the formation of Au-In-Zn alloy examined by EDS results during the period of growth. The

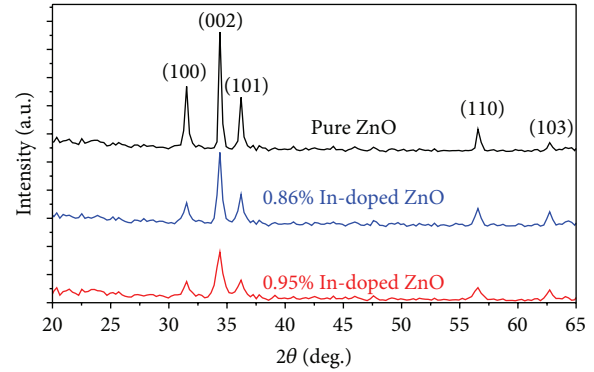


FIGURE 2: XRD patterns of ZnO and ZnO:In NWs.

SAED patterns which revealed the ZnO and ZnO:In NWs are single crystalline which are shown in insets to Figures 3(a), 3(b), and 3(c).

PL is a nondestructive and sensitive technique for investigating the band structure and defect levels of semiconductors. Figure 5 shows the PL spectra recorded at room temperature, using 325 nm line of 25 mW He-Cd laser for the excitation of ZnO and ZnO:In NWs. At the UV region in PL spectra, three strong near-band-edge (NBE) emissions associated with the exciton centered at about 380 nm were found, and on the other hand three weak broad defect-related green band (GB) emissions centered at around 540 nm were also observed at the visible light region. While we focus on the NBE emission (inset in Figure 5), the peak position and PL intensity shifts slightly to higher energy (blue-shift) and depresses with the increasing doping level of indium, respectively. The phenomenon of blue-shift can be attributed to the widening of the optical band-gap due to Burstein-Moss effect [15] which is interpreted that at high electron concentrations, due to small density of states of ZnO near the conduction band minimum, the conduction band edge is filled with excessive carriers donated by donor indium, coming from the substitution of indium for zinc and results in a blue-shift of optical transitions. Afterwards, when ZnO:In samples are excited, the excited electrons will be taken up higher energy levels and lead to a blue-shift of radiative recombination. Similar results were reported by Chen et al. in ZnO:In NWs by sol-gel method [16]. Kim and Park measured the variation of band-gap as the function of carrier concentration [17]. The NBE peak position blue-shifted, comparing to the pure ZnO, about 25 and 43 meV for ZnO doped with indium 0.86 and 0.95 at. %, respectively. According to Kim and Park's research, we suppose the carrier concentration of In-doped ZnO NWs (0.95%) would be in the region of $1.1 \times 10^{19} \text{ cm}^{-3}$. Furthermore, the depression of the NBE emission intensity can be explained by the formation of donor-induced nonradiative recombination centers originating from the incorporation of indium [18]. In comparison to higher In concentration than 1%, Bae et al. proposed that NBE emission of ZnO:In nanowires with 10~20% indium concentration shift to the lower energy region [19]. They suggested the high doping effect causes the decrease of band

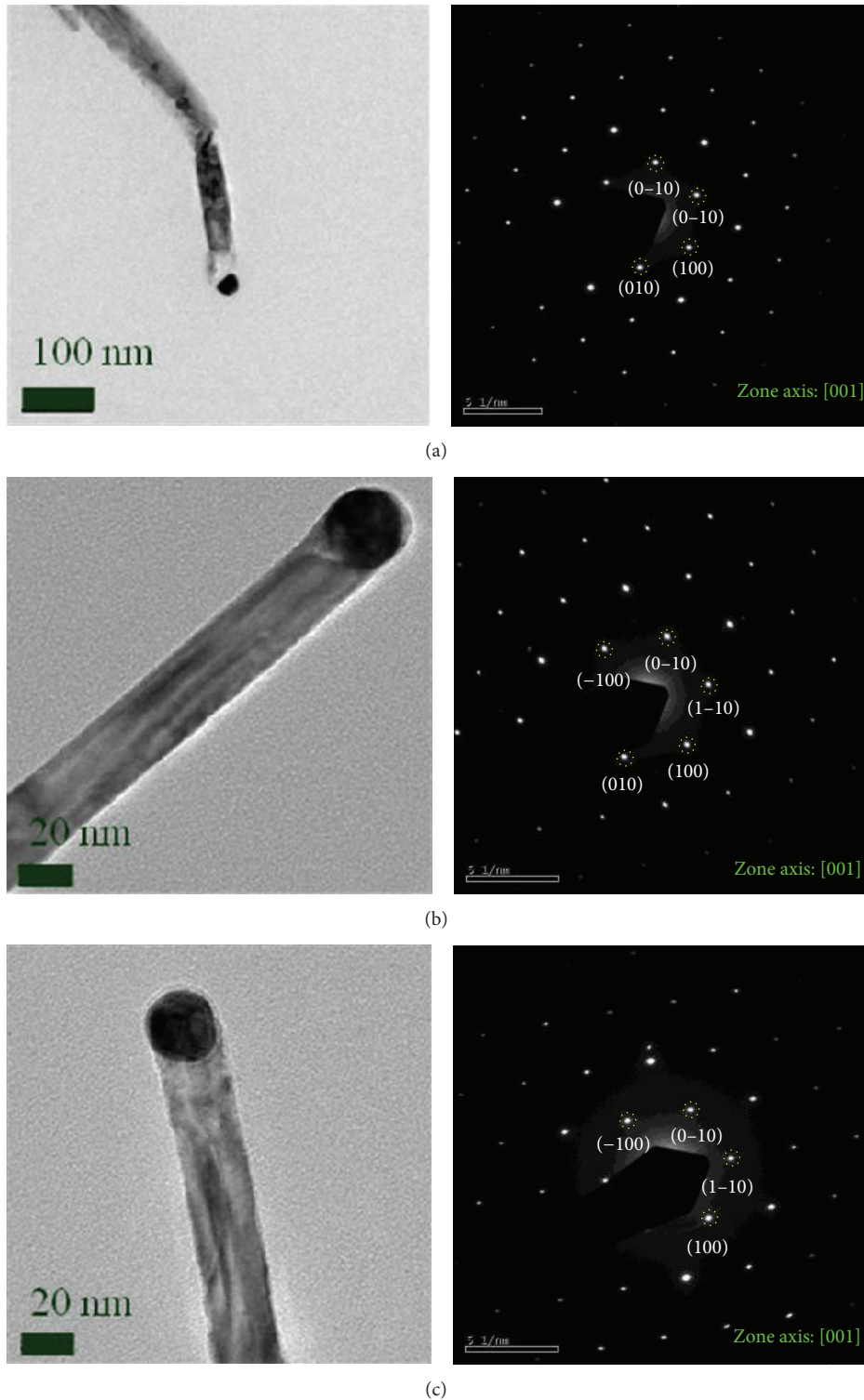


FIGURE 3: TEM images and the corresponding SAED patterns of ZnO:In NWs with different indium concentrations (a) undoped, (b) 0.86%, and (c) 0.95%.

gap and the energy broadening of valence band states. As the doped elements enter the ZnO crystal lattices, the additional localized band edge states form at the doped sites, with a reduction of band gap. After that, it is well known that the incomplete oxidation of oxide compound semiconductors

will lead to the production of nonstoichiometric defects: oxygen vacancies (V_o), and the GB emission is suggested to be the radiative recombination of electrons in singly occupied oxygen vacancies (V_o^+) with photoexcited holes in the valence band [20]. The PL spectrum of pure ZnO NWs

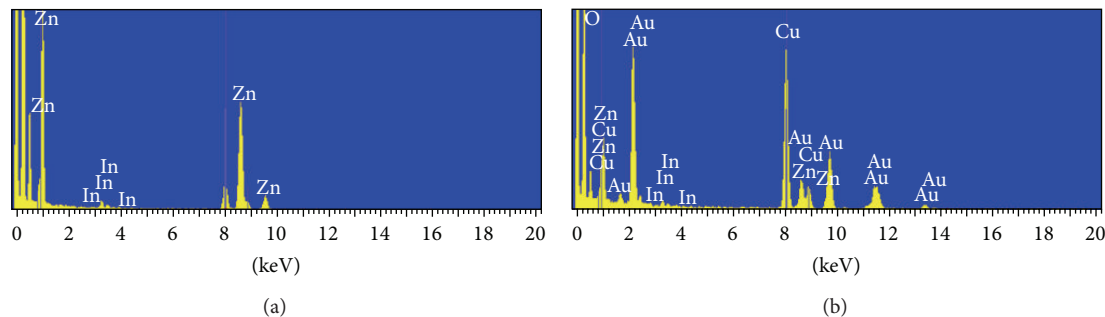


FIGURE 4: The representative EDS spectra results of (a) the stem and (b) tip part from ZnO:In NWs.

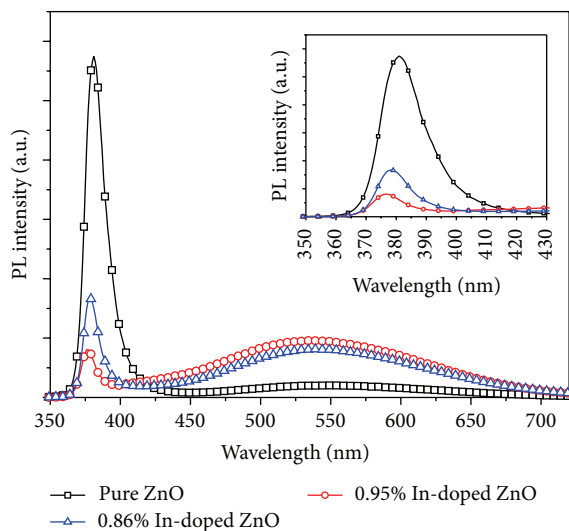


FIGURE 5: Room temperature PL spectra of ZnO and ZnO:In NWs. The inset shows the UV-region PL spectra.

exhibited a GB emission with an extremely low intensity verified ZnO NWs possessed of low oxygen vacancies were synthesized. Moreover, the intensities of GB emission from ZnO:In nanowires were slightly enhanced, which may be ascribed to the incorporation of indium.

4. Conclusion

In conclusion, we have synthesized ZnO NWs with different indium doping concentrations on gold nanoparticles coated Si substrates in the vacuum furnace by using a thermal evaporation method. From SEM investigations, the diameter range of NWs increases after the incorporation of indium. XRD shows a preferred (002) crystal face without any other impurity phase in all of our samples and the crystal quality of NWs degrades with the increasing of indium concentration. The VLS mechanism may be dominant in the growth of ZnO NWs examined by SEM and TEM images. The NBE emission peak showing a slight blue-shift with the increasing indium doping level could be attributed to Burstein-Moss effect. With the incorporation of indium, the NBE emission intensity depresses. The defect-related GB emission intensity is slightly

enhanced after the doping of indium as well. According to the structural and optical properties of lightly indium doped ZnO, it would be beneficial for electrooptical applications.

Conflict of Interests

The authors declare that there is no conflict of interests regarding the publication of this paper.

Acknowledgment

This study was supported by the National Science Council of Taiwan, under Contract NSC 102-2218-E-018-003.

References

- [1] X. W. Sun and H. S. Kwok, "Optical properties of epitaxially grown zinc oxide films on sapphire by pulsed laser deposition," *Journal of Applied Physics*, vol. 86, p. 408, 1999.
- [2] H. Kind, H. Yan, B. Messer, M. Law, and P. Yang, "Nanowire ultraviolet photodetectors and optical switches," *Advanced Materials*, vol. 14, no. 2, pp. 158–160, 2002.
- [3] M. S. Arnold, P. Avouris, Z. W. Pan, and Z. L. Wang, "Field-effect transistors based on single semiconducting oxide nanobelts," *The Journal of Physical Chemistry B*, vol. 107, no. 3, pp. 659–663, 2003.
- [4] Z. L. Wang, "Functional oxide nanobelts: materials, properties and potential applications in nanosystems and biotechnology," *Annual Review of Physical Chemistry*, vol. 55, pp. 159–196, 2004.
- [5] W. Q. Peng, S. C. Qu, G. W. Cong, and Z. G. Wang, "Synthesis and temperature-dependent near-band-edge emission of chain-like Mg-doped ZnO nanoparticles," *Applied Physics Letters*, vol. 88, no. 10, Article ID 101902, 2006.
- [6] J. C. Johnson, K. P. Knutsen, H. Yan et al., "Ultrafast carrier dynamics in single ZnO nanowire and nanoribbon lasers," *Nano Letters*, vol. 4, no. 2, pp. 197–204, 2004.
- [7] P. S. Venkatesh, V. Ramakrishnan, and K. Jeganathan, "Vertically aligned indium doped zinc oxide nanorods for the application of nanostructured anodes by radio frequency magnetron sputtering," *CrystEngComm*, vol. 14, no. 11, pp. 3907–3914, 2012.
- [8] T. Minami, H. Sonohara, T. Kakumu, and S. Takata, "Highly transparent and conductive Zn₂In₂O₅ thin films prepared by RF magnetron sputtering," *Japanese Journal of Applied Physics*, vol. 34, no. 8, p. L971, 1995.
- [9] A. C. Wang, J. Dai, J. Z. Cheng et al., "Charge transport, optical transparency, microstructure, and processing relationships in

- transparent conductive indium-zinc oxide films grown by low-pressure metal-organic chemical vapor deposition,” *Applied Physics Letters*, vol. 73, no. 3, pp. 327–329, 1998.
- [10] L. P. Peng, L. Fang, X. F. Yang et al., “Effect of annealing temperature on the structure and optical properties of In-doped ZnO thin films,” *Journal of Alloys and Compounds*, vol. 484, no. 1, pp. 575–579, 2009.
- [11] J. Jie, G. Wang, X. Hang et al., “Indium-doped zinc oxide nanobelts,” *Chemical Physics Letters*, vol. 387, no. 4–6, pp. 466–470, 2004.
- [12] D. Vorkapic and T. Matsoukas, “Effect of temperature and alcohols in the preparation of titania nanoparticles from alkoxides,” *Journal of the American Ceramic Society*, vol. 81, no. 11, pp. 2815–2820, 1998.
- [13] <http://www.powerstream.com/vapor-pressure.htm>.
- [14] R. S. Wanger and W. C. Ellis, “Vapor-liquid-solid mechanism of single crystal growth,” *Applied Physics Letters*, vol. 4, p. 89, 1964.
- [15] E. Burstein, “Anomalous optical absorption limit in InSb,” *Physical Review*, vol. 93, no. 3, pp. 632–633, 1954.
- [16] Y. W. Chen, Y. C. Liu, S. X. Lu et al., “Optical properties of ZnO and ZnO:In nanorods assembled by sol-gel method,” *The Journal of Chemical Physics*, vol. 123, no. 13, Article ID 134701, 2005.
- [17] K. J. Kim and Y. R. Park, “Large and abrupt optical band gap variation in In-doped ZnO,” *Applied Physics Letters*, vol. 78, no. 4, article 475, 2001.
- [18] Y. Cao, L. Miao, S. Tanemura et al., “Optical properties of indium-doped ZnO films,” *Japanese Journal of Applied Physics, Part 1: Regular Papers and Short Notes and Review Papers*, vol. 45, no. 3A, pp. 1623–1628, 2006.
- [19] S. Y. Bae, C. W. Na, J. H. Kang, and J. Park, “Comparative structure and optical properties of Ga-, In-, and Sn-doped ZnO nanowires synthesized via thermal evaporation,” *The Journal of Physical Chemistry B*, vol. 109, no. 7, pp. 2526–2531, 2005.
- [20] K. Vanheusden, W. L. Warren, C. H. Seager, D. R. Tallant, J. A. Voigt, and B. E. Gnade, “Mechanisms behind green photoluminescence in ZnO phosphor powders,” *Journal of Applied Physics*, vol. 79, no. 10, pp. 7983–7990, 1996.

Research Article

Improving Crystalline Silicon Solar Cell Efficiency Using Graded-Refractive-Index SiON/ZnO Nanostructures

Yung-Chun Tu,¹ Shui-Jinn Wang,^{1,2} Chien-Hung Wu,³ Kow-Ming Chang,⁴
Tseng-Hsing Lin,¹ Chien-Hsiung Hung,¹ and Jhen-Siang Wu¹

¹Institute of Microelectronics, Department of Electrical Engineering, National Cheng Kung University, Tainan 701, Taiwan

²Advanced Optoelectronic Technology Center, National Cheng Kung University, Tainan 701, Taiwan

³Department of Electronics Engineering, Chung Hua University, Hsinchu 300, Taiwan

⁴Department of Electronics Engineering, National Chiao Tung University, Hsinchu 300, Taiwan

Correspondence should be addressed to Shui-Jinn Wang; sjwang@mail.ncku.edu.tw

Received 24 November 2014; Accepted 30 December 2014

Academic Editor: Shyh-Jer Huang

Copyright © 2015 Yung-Chun Tu et al. This is an open access article distributed under the Creative Commons Attribution License, which permits unrestricted use, distribution, and reproduction in any medium, provided the original work is properly cited.

The fabrication of silicon oxynitride (SiON)/ZnO nanotube (NT) arrays and their application in improving the energy conversion efficiency (η) of crystalline Si-based solar cells (SCs) are reported. The SiON/ZnO NT arrays have a graded-refractive-index that varies from 3.5 (Si) to 1.9 ~ 2.0 (Si₃N₄ and ZnO) to 1.72 ~ 1.75 (SiON) to 1 (air). Experimental results show that the use of 0.4 μ m long ZnO NT arrays coated with a 150 nm thick SiON film increases $\Delta\eta/\eta$ by 39.2% under AM 1.5 G (100 mW/cm²) illumination as compared to that of regular SCs with a Si₃N₄/micropyramid surface. This enhancement can be attributed to SiON/ZnO NT arrays effectively releasing surface reflection and minimizing Fresnel loss.

1. Introduction

Surface roughening through the chemical wet etching process [1, 2], nanoimprint lithography [3], and nanostructures [4, 5] has been applied to roughen the top surface of optoelectronic devices. Surface roughening has attracted considerable interest for applications such as solar cells (SCs), light-emitting diodes (LEDs), ultraviolet photodetectors (UV-PDs), and gas sensors [6–9]. A suitably roughened surface can significantly improve the surface reflectivity of SCs, alleviate the total internal reflection of LEDs, and increase the responses of UV-PDs and gas sensors [6–9]. However, most surface roughening methods involve expensive lithographic patterning or cumbersome fabrication processes and can even deteriorate electrical properties, making them unsuitable for mass production.

Zinc oxide (ZnO) is a promising material for surface roughening. It has a wide direct band gap (3.37 eV at room temperature), large exciton binding energy (about 60 meV) [10, 11], and transmittance of about 85% in the visible region [12, 13]. One-dimensional ZnO nanowire (NW) arrays have

received great attention due to their ease of fabrication, low-temperature processing, and unique properties, such as large length-to-diameter ratio, high surface-to-volume ratio, and carrier confinement, which could improve device performance [6, 14–16]. Nevertheless, the transmittance of ZnO NW arrays needs to be improved for light transmission in the visible-light spectrum.

To further improve the light trapping efficiency (LTE) and light transmission of SCs in the visible region, a simple and cost-effective surface roughening scheme that employs SiON/ZnO nanotube (NT) arrays is proposed in this work. The scheme is expected to reduce the Fresnel loss effect from a graded-refractive-index structure. The optoelectronic characteristics of regular SCs and those with the proposed SiON/ZnO NT arrays, ZnO NT arrays, and conventional ZnO NW arrays, respectively, are compared and discussed.

2. Experiments

Figure 1 schematically shows the four types of SC, namely, SC-A, SC-B, SC-C, and regular SC, prepared in this study.

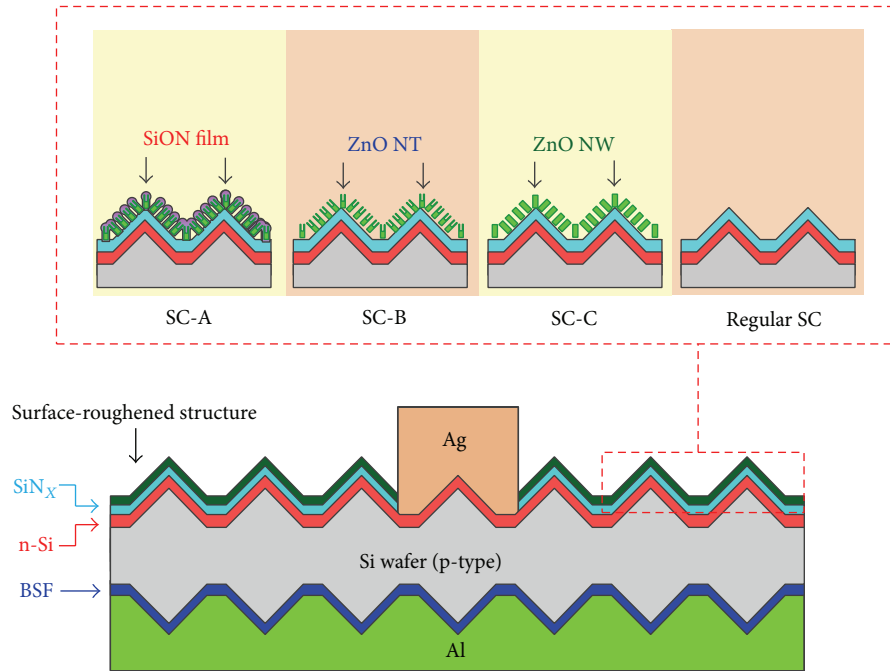


FIGURE 1: Schematic device structures of SC-A (with SiON/ZnO NT arrays), SC-B (with ZnO NT arrays), SC-C (with ZnO NW arrays), and regular SC (with KOH-etched surface).

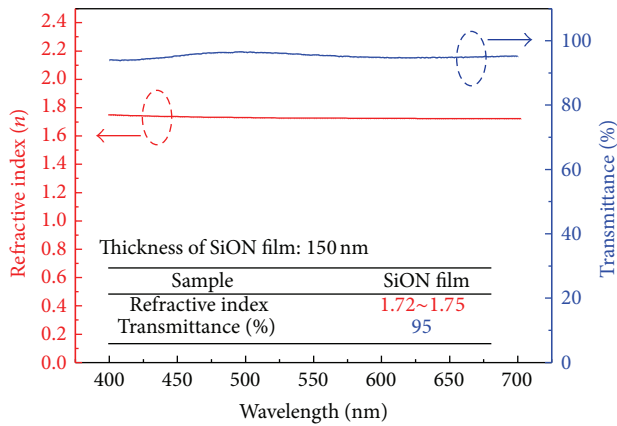


FIGURE 2: Measured transmittance and refractive index of SiON film (150 nm in thickness).

The regular SCs, prepared using the standard fabrication process, had a KOH-etched micropylamid surface and a Si_3N_4 antireflection (AR) coating. For some of the regular SCs, ZnO NW arrays, ZnO NT arrays, or SiON/ZnO NT arrays were synthesized on top of the Si_3N_4 AR layer. To synthesize ZnO NW arrays on the surface of regular SCs, a 10 nm thick ZnO seed layer was sputter-deposited onto the Si_3N_4 surface, and ZnO NW arrays were synthesized on the surface of this via the hydrothermal growth (HTG) method [17, 18]. A mixed solution of 0.07 M ZnO (NO_3) $_2 \cdot 6\text{H}_2\text{O}$ and 0.07 M $\text{C}_6\text{H}_{12}\text{N}_4$ at 80°C was employed for 120 min in the HTG process. The typical diameters and lengths of the obtained ZnO NW arrays were in the ranges of 100–200 nm and 400–500 nm,

respectively. These ZnO-NW-based devices are referred to as SC-C.

A two-step HTG method was used to synthesize ZnO NT arrays on the surface of regular SCs. To synthesize ZnO NT arrays with dimensions equal to those of the NW arrays, the HTG parameters mentioned above were used in the first HTG process. The second step was conducted at 80°C for 120 min and then at room temperature for 24 h for tube formation, which could be caused by the occurrence of a dissolving process at lower temperature [19, 20]. In addition to increased surface roughness, the ZnO NT arrays are expected to alleviate the light absorption that occurs in conventional ZnO nanowires and overcome the issue of light reflection by offering a suitable effective refractive index. SCs based on ZnO NT arrays are referred to as SC-B.

Finally, a 150 nm thick SiON layer with a typical refractive index of 1.72–1.75 was coated onto the ZnO NT arrays using a plasma-enhanced chemical vapor deposition system. A mixed gas of N_2O (350 sccm), NH_3 (10 sccm), 5% SiH_4 (120 sccm), and N_2 (400 sccm) was employed for the deposition process. The applied plasma power was 120 W, the chamber pressure was 700 mTorr, and the substrate temperature was kept at 300°C. These devices are referred to as SC-A. All four types of SC had a die size of 2.1 cm × 3.4 cm.

The light reflectance and refractive indexes of the prepared SiON films and ZnO nanostructures were characterized using a spectrophotometer and an ellipsometer, respectively. The current density-voltage (J - V) and EQE characteristics of the prepared SCs were measured using a Science Tech 150 W under standard AM 1.5G test conditions (100 mW/cm 2 at 25°C).

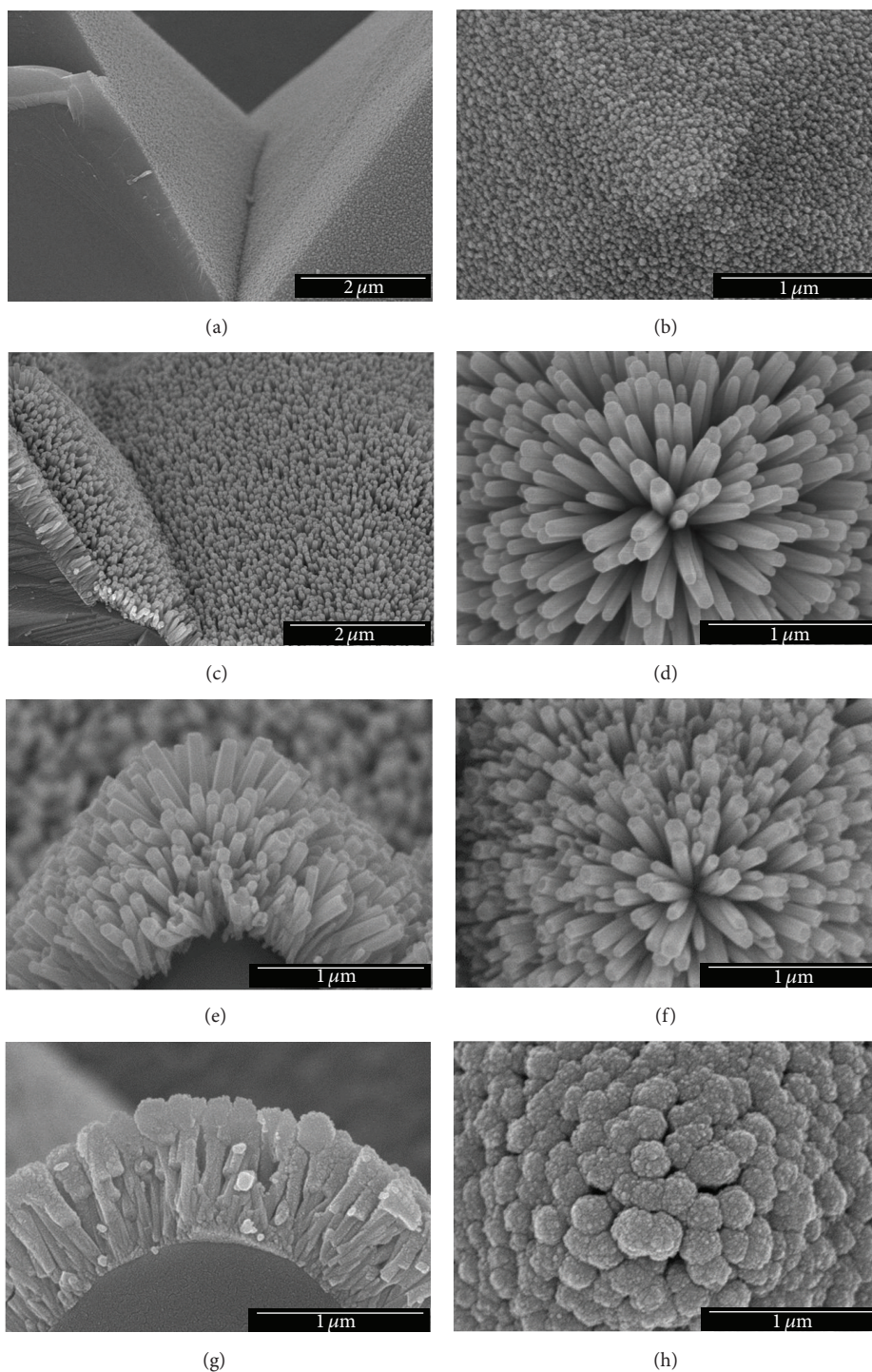


FIGURE 3: SEM images of surface morphology of prepared SCs. (a) Tilted- and (b) top-view images of regular SC, (c) tilted- and (d) top-view images of SC-C, (e) tilted- and (f) top-view images of SC-B, and (g) tilted- and (h) top-view images of SC-A.

3. Results and Discussion

The measured light transmittance and refractive index (n) of the prepared 150 nm thick SiON film are shown in Figure 2. The film has a good transmittance of approximately 95% in the visible-light spectrum and a refractive index of 1.72–1.75.

The results reveal that a 150 nm thick SiON film deposited atop ZnO NT arrays does not significantly absorb sunlight. The film creates a graded-refractive-index scheme with the refractive index varying from 2.0~2.1 ($\text{ZnO}/\text{Si}_3\text{N}_4$) [21] to 1.72~1.75 (SiON) to 1 (air) for SC-A. Figure 3 shows top- and tilted-view scanning electron microscopy (SEM) images of

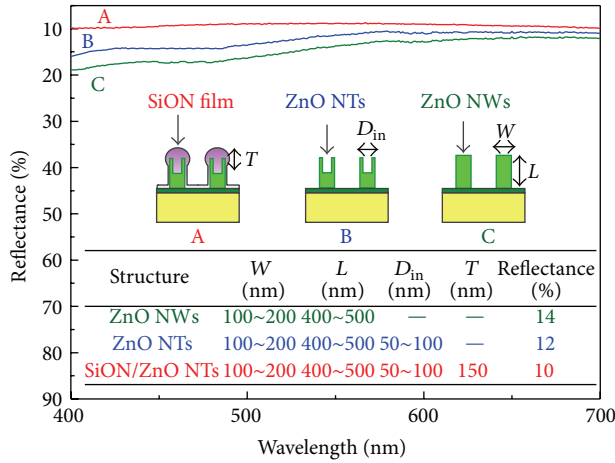


FIGURE 4: Measured reflectance of SiON/ZnO NT, ZnO NT, and NW arrays on ZnO (seed layer)/glass substrate. Thickness of ZnO seed layer is 10 nm.

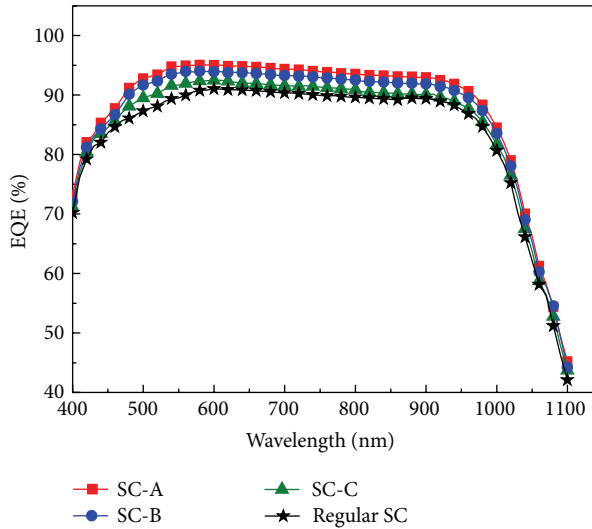


FIGURE 5: Measured EQE as a function of wavelength λ for four types of SC with different surface roughness.

the surface morphology of the four types of SC. Distinctive nanostructures can be clearly observed on top of the $\text{Si}_3\text{N}_4/\text{n-Si}$ surface. The micropyramid structures shown in Figures 3(a) and 3(b) were obtained via anisotropic etching of the Si surface using an alkaline solution. They have an average height and diameter of 3 and 5 μm , respectively. Figures 3(c) and 3(d) show the morphology of the HTG-prepared ZnO NW arrays atop the $\text{Si}_3\text{N}_4/\text{KOH}$ -etched n-Si surface. Figures 3(e) and 3(f) show the ZnO NT arrays obtained from the second step of the HTG process. Figures 3(g) and 3(h) show SiON/ZnO NT arrays with a sphere-like surface obtained via the deposition of SiON film onto the ZnO NT arrays.

The light reflectance of the ZnO NW arrays, ZnO NT arrays, and SiON/ZnO NT arrays atop the ZnO seed layer (10 nm)/glass substrate is shown in Figure 4. It can be seen that the SiON/ZnO NT arrays have the best antireflective

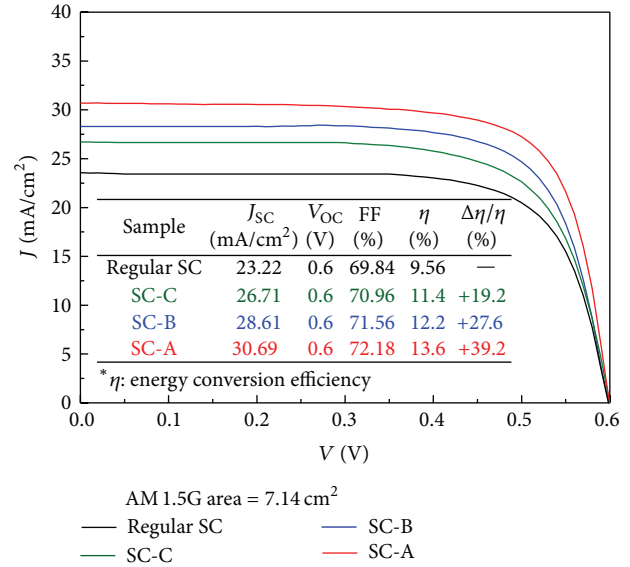


FIGURE 6: Measured J - V characteristics of regular SC, SC-C, SC-B, and SC-A. Inset shows measured cell parameters.

properties (around 10%) in the visible-light spectrum, while the ZnO NWs arrays have reflectance of about 14%. Figure 5 shows the measured external quantum efficiency (EQE) as a function of wavelength λ for four types of SC with different surface roughness. It is found that the SC-A generally has the highest EQEs in the visible-light spectrum, and this is consistent with the reflectance data presented above. The high antireflection and EQE of the SiON/ZnO NT arrays can be attributed to the sphere-like morphology and the formation of a graded-refractive-index layer structure.

The J - V characteristics of the fabricated SCs are shown in Figure 6 to examine the effectiveness of the SiON/ZnO NT arrays with regard to enhancing energy conversion efficiency. With the regular SC as a reference, details of the measured SC parameters, namely, short-circuit current density (J_{SC}), open-circuit voltage (V_{OC}), fill factor (FF), energy conversion efficiency (η), and enhanced energy conversion efficiency enhancement ($\Delta\eta/\eta$) are listed in the inset. The surface roughening schemes provide different degrees of improvement in short-circuit current density and FF, which is attributed to a direct consequence of the broadband light trapping and the reduction in series resistance, as compared with that of the regular SCs. Note that the decreased series resistance is caused by the increase in electron and hole concentrations due to maximizing the light irradiation from air to the active region of cell. Similar experimental results with regard to improved FF have been reported for SCs with different surface structures [21–23]. In contrast, the open-circuit voltage shows no noticeable change, and this suggests that the parallel resistances of the three types of SC are not affected by surface roughening. As shown in Figure 6, SC-A, SC-B, and SC-C show $\Delta\eta/\eta$ increases of 39.2%, 27.6%, and 19.2%, respectively, as compared to a regular SC under AM 1.5G (100 mW/cm²) illumination. SC-A (150 nm thick SiON film and 0.4 μm long ZnO NT arrays) shows the

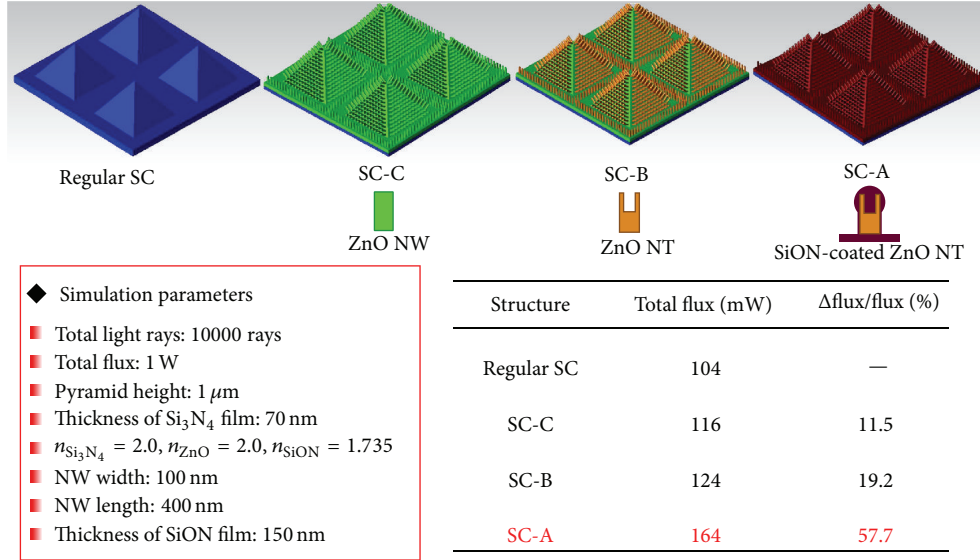


FIGURE 7: Simulation and calculation results of regular SC, SC-C, SC-B, and SC-A.

best improvement in cell performance. This is likely due to the effectiveness of this type of surface roughening, which promotes angular randomization of incident sunlight and enhances LTE. In addition, the SiON/ZnO NT arrays create a graded-refractive-index surface structure scheme, with the refractive index ranging from 2.0–2.1 (ZnO/Si₃N₄) [24] to 1.72–1.75 (SiON) to 1 (air). The use of SiON could maximize light irradiation from air to Si₃N₄, and thus to the active region of the cell, without causing light reflection, because it offers a refractive index (1.72–1.75) that satisfies the optimized refractive index equation [25] $n_{\text{opt}} = \sqrt{n_1 \times n_2}$, where n_1 is the refractive index of ZnO/Si₃N₄ ($n = 2.0\text{--}2.1$) [24] and n_2 is the refractive index of EVA ($n = 1.51$) [26].

The simulation results shown in Figure 7 demonstrate an LTE improvement trend that is similar to those obtained in the experimental findings. To further clarify the effectiveness of the surface roughening schemes, the light absorption efficiency of SCs with micropylramids, ZnO NW arrays atop the micropylramids, ZnO NT arrays atop the micropylramids, and SiON/ZnO NT arrays atop the micropylramids was simulated using Tracepro [7]. The results are shown in Figure 7. The amount of total flux through the SCs with SiON/ZnO NT arrays atop the micropylramids is much larger than that of the SCs with micropylramids, which is in good agreement with the experimental findings. The Fresnel loss at the air/SiON/ZnO/Si₃N₄/Si surface is minimized through the combined effect of surface roughening and the refractive-index-matched (RIM) scheme provided by the SiON/ZnO NT arrays. The theoretical results agree well with the experimental ones. Although the structural parameters of the SiON/ZnO NT arrays need to be further optimized, the results provide a guideline for increasing the LTE of SCs.

4. Conclusion

The effectiveness of a surface roughening scheme was demonstrated with regard to improving the efficiency of

SCs with SiON/ZnO NT arrays. The RIM SiON (150 nm in thickness)/ZnO NT (0.4 μm in length) structure significantly improved the efficiency of SC-A (by 39.2%) under AM 1.5G (100 mW/cm^2) illumination compared with that of a regular SC. This enhancement can be attributed to the RIM SiON/ZnO NT array structure promoting the angular randomization of incident sunlight at the surface of the Si₃N₄/n-Si layer, effectively releasing surface reflection, and minimizing Fresnel loss. It is expected that the proposed RIM scheme with SiON/ZnO NT arrays can be applied to prepare high-energy-conversion-efficiency SCs.

Conflict of Interests

The authors declare that there is no conflict of interests regarding the publication of this paper.

Acknowledgments

This work was supported by the Ministry of Science and Technology (MOST) of Taiwan, under Grant MOST 103-2221-E-006-132 and the National Science Council (NSC) of Taiwan, under Grant NSC 102-2221-E-006-217-MY2. The authors would like to thank the National Nano Device Laboratories and the Center for Micro/Nano Science and Technology, National Cheng Kung University, Taiwan, for equipment access and financial and technical support.

References

- [1] C.-E. Lee, Y.-C. Lee, H.-C. Kuo, T.-C. Lu, and S.-C. Wang, "Further enhancement of nitride-based near-ultraviolet vertical-injection light-emitting diodes by adopting a roughened mesh-surface," *IEEE Photonics Technology Letters*, vol. 20, no. 10, pp. 803–805, 2008.

- [2] M. Berginski, J. Hüpkes, M. Schulte et al., "The effect of front ZnO:Al surface texture and optical transparency on efficient light trapping in silicon thin-film solar cells," *Journal of Applied Physics*, vol. 101, no. 7, Article ID 074903, 2007.
- [3] H. W. Huang, C. H. Lin, K. Y. Lee et al., "Enhanced light output power of GaN-based vertical-injection light-emitting diodes with a 12-fold photonic quasi-crystal by nano-imprint lithography," *Semiconductor Science and Technology*, vol. 24, no. 8, Article ID 085008, 2009.
- [4] R. Sivakumar, K. Punitha, C. Sanjeeviraja, and R. Gopalakrishnan, "Morphology control of ZnO nanostructures by catalyst-free and seed-mediated simple aqueous solution growth method," *Materials Letters*, vol. 121, pp. 141–144, 2014.
- [5] K. V. Gurav, M. G. Gang, S. W. Shin et al., "Gas sensing properties of hydrothermally grown ZnO nanorods with different aspect ratios," *Sensors and Actuators B: Chemical*, vol. 190, pp. 439–445, 2014.
- [6] L.-K. Yeh, K.-Y. Lai, G.-J. Lin et al., "Giant efficiency enhancement of GaAs solar cells with graded antireflection layers based on syringelike ZnO nanorod arrays," *Advanced Energy Materials*, vol. 1, no. 4, pp. 506–510, 2011.
- [7] Y. C. Tu, S. J. Wang, G. Y. Lin et al., "Enhanced light output of vertical GaN-based LEDs with surface roughened by refractive-index-matched $\text{Si}_3\text{N}_4/\text{GaN}$ nanowire arrays," *Applied Physics Express*, vol. 7, no. 4, Article ID 042101, 2014.
- [8] K. J. Chen, F. Y. Hung, S. J. Chang, and S. J. Young, "Optoelectronic characteristics of UV photodetector based on ZnO nanowire thin films," *Journal of Alloys and Compounds*, vol. 479, no. 1-2, pp. 674–677, 2009.
- [9] T.-Y. Chen, H.-I. Chen, C.-S. Hsu et al., "ZnO-nanorod-based ammonia gas sensors with underlying Pt/Cr interdigitated electrodes," *IEEE Electron Device Letters*, vol. 33, no. 10, pp. 1486–1488, 2012.
- [10] Y.-C. Tu, S.-J. Wang, J.-C. Lin et al., "Light output improvement of GaN-based light-emitting diodes using hydrothermally grown ZnO nanotapers," *Japanese Journal of Applied Physics*, vol. 52, no. 6, supplement, Article ID 06GG13, 2013.
- [11] F.-S. Tsai, S.-J. Wang, Y.-C. Tu et al., "Preparation of p-SnO/n-ZnO heterojunction nanowire arrays and their optoelectronic characteristics under UV illumination," *Applied Physics Express*, vol. 4, no. 2, Article ID 25002, 2011.
- [12] J. L. Zhao, X. M. Li, J. M. Bian, W. D. Yu, and X. D. Gao, "Structural, optical and electrical properties of ZnO films grown by pulsed laser deposition (PLD)," *Journal of Crystal Growth*, vol. 276, no. 3-4, pp. 507–512, 2005.
- [13] J. Yi, J. M. Lee, and W. I. Park, "Vertically aligned ZnO nanorods and graphene hybrid architectures for high-sensitive flexible gas sensors," *Sensors and Actuators B: Chemical*, vol. 155, no. 1, pp. 264–269, 2011.
- [14] Y. Li, F. D. Valle, M. Simonnet, I. Yamada, and J.-J. Delaunay, "High-performance UV detector made of ultra-long ZnO bridging nanowires," *Nanotechnology*, vol. 20, no. 4, Article ID 045501, 2009.
- [15] Y. Liu, Z. Lin, K. S. Moon, and C. P. Wong, "Novel ZnO nanowires/silicon hierarchical structures for superhydrophobic, low reflection, and high efficiency solar cells," in *Proceedings of the IEEE 61st Electronic Components and Technology Conference (ECTC '11)*, pp. 2114–2118, Lake Buena Vista, Fla, USA, May-June 2011.
- [16] X. Yu, D. Wang, D. Lei, G. Li, and D. Yan, "Efficiency improvement of silicon solar cells enabled by ZnO nanowhisker array coating," *Nanoscale Research Letters*, vol. 7, article 306, 2012.
- [17] P.-Y. Yang, J.-L. Wang, P.-C. Chiu et al., "pH sensing characteristics of extended-gate field-effect transistor based on Al-doped ZnO nanostructures hydrothermally synthesized at low temperatures," *IEEE Electron Device Letters*, vol. 32, no. 11, pp. 1603–1605, 2011.
- [18] K. H. Baik, H. Kim, J. Kim, S. Jung, and S. Jang, "Nonpolar light emitting diode with sharp near-ultraviolet emissions using hydrothermally grown ZnO on p-GaN," *Applied Physics Letters*, vol. 103, no. 9, Article ID 091107, 2013.
- [19] A. Wei, X. W. Sun, C. X. Xu et al., "Growth mechanism of tubular ZnO formed in aqueous solution," *Nanotechnology*, vol. 17, no. 6, pp. 1740–1744, 2006.
- [20] A. Wei, X. W. Sun, C. X. Xu, Z. L. Dong, M. B. Yu, and W. Huang, "Stable field emission from hydrothermally grown ZnO nanotubes," *Applied Physics Letters*, vol. 88, no. 21, Article ID 213102, 2006.
- [21] H. C. Chen, C. C. Lin, H. W. Han et al., "Enhanced efficiency for c-Si solar cell with nanopillar array via quantum dots layers," *Optics Express*, vol. 19, no. 19, pp. A1141–A1147, 2011.
- [22] I. Lee, D. G. Lim, S. H. Lee, and J. Yi, "The effects of a double layer anti-reflection coating for a buried contact solar cell application," *Surface and Coatings Technology*, vol. 137, no. 1, pp. 86–91, 2001.
- [23] S. K. Sardana, V. S. N. Chava, E. Thouti et al., "Influence of surface plasmon resonances of silver nanoparticles on optical and electrical properties of textured silicon solar cell," *Applied Physics Letters*, vol. 104, no. 7, Article ID 073903, 2014.
- [24] F. K. Shan and Y. S. Yu, "Band gap energy of pure and Al-doped ZnO thin films," *Journal of the European Ceramic Society*, vol. 24, no. 6, pp. 1869–1872, 2004.
- [25] X. Da, X. Guo, L. Dong, Y. Song, W. Ai, and G. Shen, "The silicon oxynitride layer deposited at low temperature for high-brightness GaN-based light-emitting diodes," *Solid-State Electronics*, vol. 50, no. 3, pp. 508–510, 2006.
- [26] E. Klampaftis and B. S. Richards, "Improvement in multicrystalline silicon solar cell efficiency via addition of luminescent material to EVA encapsulation layer," *Progress in Photovoltaics: Research and Applications*, vol. 19, no. 3, pp. 345–351, 2011.

Research Article

Optoelectric Properties of GaInP p-i-n Solar Cells with Different i-Layer Thicknesses

**Tsung-Shine Ko,¹ Der-Yuh Lin,¹ You-Chi He,¹ Chen-Chia Kao,¹ Bo-Yuan Hu,¹
Ray-Hua Horng,² Fan-Lei Wu,² Chih-Hung Wu,³ and Yu-Li Tsai³**

¹Department of Electronic Engineering, National Changhua University of Education, No. 1, Jin-De Road, Changhua 500, Taiwan

²Department of Materials Science and Engineering, National Chung Hsing University, 250 KuoKuang Road, Taichung 402, Taiwan

³High Concentration Photovoltaic Project, Institute of Nuclear Energy Research, 4th Floor, No. 90, Luke 5th Road, Lujhu District, Kaohsiung 821, Taiwan

Correspondence should be addressed to Der-Yuh Lin; dylin@cc.ncue.edu.tw

Received 9 December 2014; Revised 29 January 2015; Accepted 29 January 2015

Academic Editor: Shyh-Jer Huang

Copyright © 2015 Tsung-Shine Ko et al. This is an open access article distributed under the Creative Commons Attribution License, which permits unrestricted use, distribution, and reproduction in any medium, provided the original work is properly cited.

The optoelectric properties of GaInP p-i-n solar cells with different intrinsic layer (i-layer) thicknesses from 0.25 to 1 μm were studied. Both emission intensity and full width at half maximum features of the photoluminescence spectrum indicate that the optimum i-layer thickness would be between 0.5 and 0.75 μm . The integrated current results of photocurrent experiment also point out that the samples with 0.5 to 0.75 μm i-layer thicknesses have optimum value around 156 nA. Electroreflectance measurements reveal that the built-in electric field strength of the sample gradually deviates from the theoretical value larger when i-layer thickness of the sample is thicker than 0.75 μm . *I-V* measurements also confirm crystal quality for whole samples by obtaining the information about short currents of photovoltaic performances. A series of experiments reflect that thicker i-layer structure would induce more defects generation lowering crystal quality.

1. Introduction

Solar cell devices play an important role in renewable energies which convert solar energy directly into electricity. In recent years, tandem structures have been developed for high efficiency applications. These were stacked by multiple subcells with different band gaps to absorb the sun light in different spectral ranges and convert it into electric power. Multijunction III-V tandem structure solar cells such as GaInP/GaInAs/Ge triple junction cells have attracted increasing attention for their very high conversion efficiencies [1, 2]. However, the high cost of III-V tandem cells has been the main impediment for their widespread applications. Another kind of basic solar cell structures is p-i-n structure, which consists of p- and n-doped regions on top and bottom layers and an intrinsic layer (i-layer) in middle one. It provides a simple way to improve the absorption ability with a thick intrinsic region. It is also well known that the built-in electric

field plays a critical role in solar cell devices; however, it is difficult to detect by electric methods directly and less studies have been reported [3]. In addition, the different thicknesses of an i-layer would be studied in detail because the thicker i-layer may induce more defects and lower the built-in electric field. Modulation spectroscopy is a powerful tool for studying optical fine structures in semiconductor devices and materials [4–9]. In order to evaluate the i-layer quality, a systematic optical characterization of thickness and built-in electric field must be clarified for giving us information in order to optimize the power conversion efficiency. These parameters are also desirable for improving the tandem cell design and improving the quality of the epitaxial layers.

In this study, we performed photoluminescence (PL) and photocurrent (PC) spectra measurements to detect the energy band gap of GaInP layers and understand the absorption behaviors of these devices. We also measure the period of Franz-Keldysh oscillations (FKOs) using electroreflectance

p-GaAs contact
p-AlGaInP window
p-GaInP emitter
i-GaInP
n-GaInP base
n-AlGaInP BSF
n-GaAs buffer
n-GaAs substrate

FIGURE 1: The main structure of GaInP p-i-n solar cells.

(ER) spectroscopy to reveal the built-in electric field strength. Consequently, the ER results could determine whether the i-layer thickness is suitable or not for device design. Furthermore, the I - V measurements for the devices could provide many important pieces of information and optoelectric characteristics such as short current (I_{sc}), open circuit (V_{oc}), fill factor (FF), efficiency (η), series resistance (R_s), and shunt resistance (R_{sh}). Comparing the information collected by the different techniques, a clear picture of the built-in electric field and an optimized i-layer thickness in InGaP p-i-n solar cells will be presented in the following content.

2. Experimental Methods

A series of GaInP p-i-n solar cells with different i-layer thicknesses were grown on (100) GaAs substrates by low pressure metal-organic chemical vapor deposition system, and the layered structure is schematically presented in Figure 1. On the top of the n-GaAs substrate, there is an n-GaAs buffer layer, followed by an n-AlGaInP back surface field layer ($0.1\ \mu\text{m}$) and a p-i-n structure consisting of an n-GaInP base ($0.3\ \mu\text{m}$), an i-GaInP layer, and a p-GaInP emitter layer ($0.1\ \mu\text{m}$), followed by an AlGaInP window layer ($0.03\ \mu\text{m}$) and a p-GaAs contact layer ($0.3\ \mu\text{m}$). The composition ratios are about $\text{Ga}_{0.5}\text{In}_{0.5}$ for i-layer and $(\text{Al}_{0.35}\text{Ga}_{0.65})_{0.5}\text{In}_{0.5}\text{P}$ for back surface field layer. According to growth rate and period information, the thicknesses of the i-layers for the four samples that could be calculated are 0.25, 0.5, 0.75, and $1\ \mu\text{m}$, respectively. We symbolized them as samples A, B, C, and D. The doping concentrations for the emitter and base layers of all samples are 2×10^{18} and $3 \times 10^{17}\ \text{cm}^{-3}$, respectively.

PL spectra were performed by using a 100 mW diode pump solid state laser with wavelength of 532 nm for studying the composition and crystal quality of the GaInP layer. A silicon detector and a 0.25 m monochromator equipped with a lock-in amplifier were used to record the optical intensity of the PL spectra. For PC spectra system, the monochromatic light coming from a 150 W halogen lamp was filtered by a monochromator and then focused on the sample surface by a lens. The photocurrent induced by the monochromatic light was measured by a Keithley 6485 picoampere meter. In order to detect the built-in electric field in the solar cells,

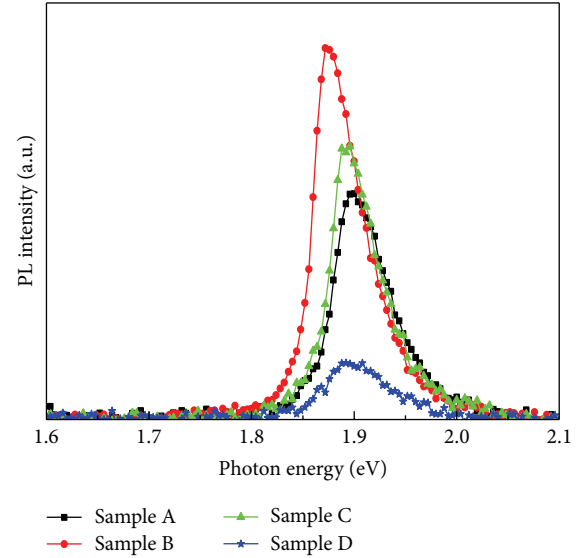


FIGURE 2: The room temperature PL spectra of samples A~D.

ER spectra were performed at various reversed biases [5, 6]. The modulation voltage is 0.3 V and the system configuration is similar to the reflectivity measurement and the detailed experimental setup has been described elsewhere [10, 11]. Furthermore, a solar simulator (SS150 fully reflective solar simulator) was used to obtain the I - V characteristics.

3. Results and Discussion

The PL spectra of samples A, B, C, and D with peaks around 1.9 eV are shown in Figure 2. For these four samples, the PL signals mainly come from the i-GaInP layer, because the high doping will induce nonradiative centers and weaken the luminescent efficiency in p- and n-doping layers. The PL intensity was enhanced as the i-layer thickness increased from 0.25 to $0.5\ \mu\text{m}$. Since main radiative recombination centers located in the thicker i-layer, the PL intensity of sample C is lower than that of sample B although it had a thicker i-layer. In general, PL intensity reflects the probability of a radiative recombination and gives us an evaluation reference for the crystal quality. A high crystalline quality layer exhibits strong PL intensity; however, a layer with poor crystalline quality shows a weak emission because most of the photo generated carriers are recombined by nonradiative recombination centers. Therefore, this result could be probably attributed to the generation of defects in the thick i-layer of sample C. Comparing with the PL peak intensity of samples A, B, and C, the intensity of sample D is quite small. This weak PL intensity indicates that the i-layer quality is also not good due to many defects that have been generated in sample D, which affects the efficiency of the solar cell. Furthermore, we also noted that the full width at half maximum (FWHM) value of the PL spectra is 18.9, 19.3, 20.1, and 25.0 nm for four samples, respectively. Sample D has the largest FWHM value among all samples, which is another evidence showing that the crystalline quality of the i-layer could be degraded

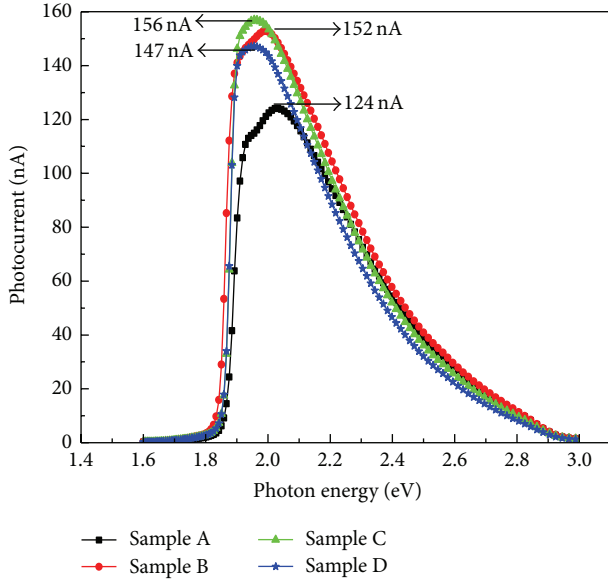


FIGURE 3: The PC spectra of samples A~D.

as the layer thickness increases beyond a critical thickness. In addition, the PL peaks of the four samples are at around 1.88 eV closely. According to the relationship between energy band gap and alloy composition presented in the previous literatures [12, 13], the alloy compositions x of $\text{Ga}_x\text{In}_{1-x}\text{P}$ for samples A to D are determined to be 0.58, 0.54, 0.58, and 0.58, respectively, by using the following equation:

$$E_g = 1.32 + 0.7x + 0.68x^2. \quad (1)$$

The effect of *i*-layer thickness on PC spectra is shown in Figure 3. For four samples, the photo-induced currents all rise abruptly at 1.9 eV indicating the absorption edge positions of the solar cells. The PC peak currents are 124, 152, 156, and 147 nA for samples A to D, respectively, while the integrated values are 63, 76, 71, and 66 nA. In comparison with sun illumination, the low integrated values here is that the samples were measured under single frequent light filtered by the monochromator. The peak and integrated values of sample A are smaller than those of the other samples due to the fact that the *i*-layer is too thin to absorb all light. As the thickness of the *i*-layer increases, a larger photocurrent generation could be expected. Obviously, the PC values for samples B and C were improved among all samples. However, with the *i*-layer thickness continuously increasing, the PC results tend to saturate and then decrease due to the formation of a high density point defect in the thick *i*-layer, which are also consistent with the above PL results. Both the PC and PL results indicate that the optimum *i*-layer thickness should be between 0.5 and 0.75 μm . Furthermore, we analyzed the peak shifts between the PL peak and the PC absorption edge carefully. It is obvious to find that the shifts from sample A to sample D are small and still in a reasonable range (~ 20 meV). These shifts are probably due to slight difference in composition or thickness uniformity because the measurement positions are not totally the same between PL and PC experiments.

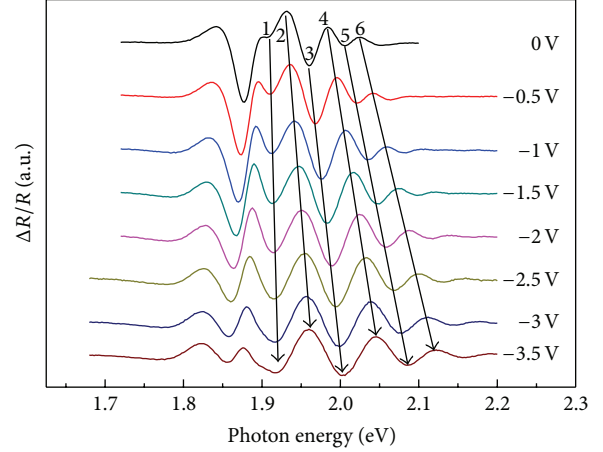


FIGURE 4: The ER spectra of sample A measured at different reverse biases from 0 to 3.5 V.

In general, a small perturbation was triggered for modulation spectroscopy using an external voltage or temperature change to create a periodic variation on the band gap; afterward, the optical absorption coefficients and the dielectric coefficients would be changed as well. The basic principle of ER is to take the derivative of the optical spectrum with respect to a modulation of an electric field. The absorption transitions of carriers could be resolved and other background signals of the ER system could be diminished using a lock-in amplifier to detect the small variation in the reflected light of probe beam. ER system has been widely utilized to reveal the transition energies of quantum wells and the built-in electric fields in many kinds of junction structures [14]. Based on the Franze and Keldysh theory [15], Shen et al. proposed a precise evaluation of the electric field strength by analyzing the period of FKO's existing in ER spectra [16, 17]. Due to the advantages of noncontact and nondestructive methods, these efforts allow modulation spectroscopy a unique method for detecting the built-in electric field in diode and transistor structures [18–20]. For *p-i-n* solar cells, a high electric field is built across the *i*-layer by the Fermi level difference between the *p*- and *n*-doped layers. This built-in electric field is the engine for driving the electron-hole pairs induced by solar light out of the cells and generating electric power. Therefore, we utilized ER measurement to obtain the built-in electric field in the *i*-layer with different thicknesses for the all samples. In Figure 4, we present the ER spectra of sample A at different reverse biases and calculate the built-in electric field strength F from FKO periods. The ER line shape is given approximately by [21]

$$\frac{\Delta R}{R} \propto \exp\left(\frac{-\Gamma(E - E_g)^{1/2}}{(\hbar\Omega)^{3/2}}\right) \cos\left(\frac{2}{3}\left[\frac{E - E_g}{\hbar\Omega}\right]^{3/2} + \theta\right), \quad (2)$$

where $\Delta R/R$ is normalized reflectance difference, E is photon energy, Γ is a damping parameter, $\hbar\Omega$ is electrooptic energy,

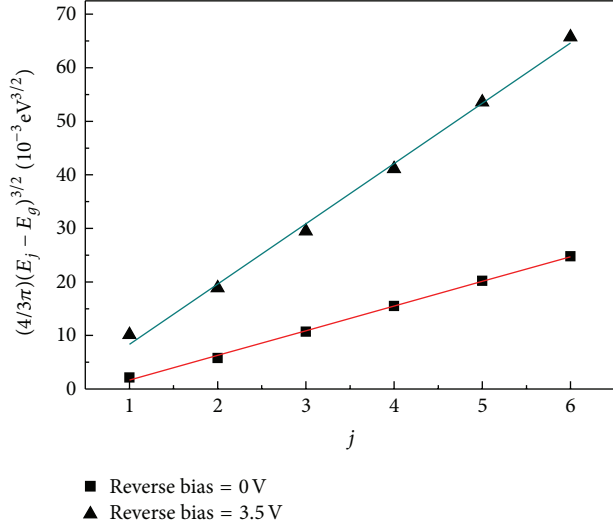


FIGURE 5: The photon energy of the j_{th} as a function of the index j for ER analysis of sample A.

and θ is a phase factor. The cosine term has extrema at energies E_j given by

$$[E_j - E_g]^{3/2} = \frac{3}{2} [\hbar\Omega]^{3/2} (j\pi - \theta) \quad j = 0, 1, 2, 3, \dots, \quad (3)$$

where j is the index number of the j_{th} extremum. The carriers have a resulting electrooptic energy:

$$\hbar\Omega = \left(\frac{e^2 \hbar^2 F^2}{8\mu} \right)^{1/3}, \quad (4)$$

where e is the electronic charge and μ is the inter band reduced effective mass in the field direction. Figure 4 displays the ER spectra of sample A measured at different reverse biases between 0 and 3.5 V. The first feature below 1.9 eV shows the direct energy band gap (E_g) of the i-layer, while features above 1.9 eV are the FKO features. Their photon energies are labeled as 1–6 and guided by the lines with arrows in the end, shift toward high energy with increasing reverse bias due to the increase of the built-in electric field. Figure 5 shows the photon energy of the j_{th} , which is defined as $(4/3\pi)(E_j - E_g)^{3/2}$, and plots as a function of the index j for further ER analysis of sample A. The results indicate two straight lines, squares for zero bias and triangles for 3.5 V reverse bias which we provide for the samples. From the slope of this straight line and (4), the built-in electric fields were determined to be 90 kV/cm at zero bias and 223 kV/cm at 3.5 V reverse bias, respectively. This built-in electric field in the i-layer of a p-i-n structure is mainly determined by the doping levels in n-, p-layers, and the thickness of the i-layer. Because the doping levels are quite high which is $2 \times 10^{18} \text{ cm}^{-3}$ in the p layer and $3 \times 10^{17} \text{ cm}^{-3}$ in the n layers, a lot of electrons and holes are accumulated at both sides of the i-layer and the Fermi level is very close to conduction and valence bands in n- and p-type layers, respectively. Therefore, the built-in electric field at zero bias can be estimated by

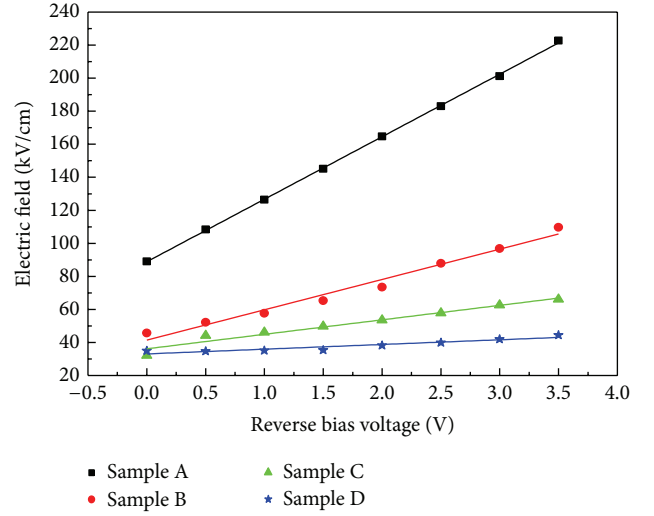


FIGURE 6: The fitting built-in electric fields of samples A~D from the ER results under various biases.

TABLE 1: Increasing rate of built-in electric field strength for samples A~D.

	Increasing rate of built-in electric field (kV/cm)			
	A	B	C	D
Theoretical value	40	20	13.3	10
Experimental value	38	18	10	3

the energy band gap of InGaP divided by i-layer thickness. On the basis of this simple calculation, the theoretical value of the built-in electric field is 86.3 kV/cm for sample A. This theoretical value of the built-in electric field matches well with the measured result.

Figure 6 shows the built-in electric fields of samples A to D which are fitted from the ER spectra results under various biases. These built-in electric fields results reveal a linear accession trend with increasing the reverse bias. The corresponding accession values of built-in electric fields are 38, 18, 10, and 3 kV/cm for samples A to D, respectively. The reverse voltage could be applied on the i-GaInP due to the small leakage current. Therefore, the theoretical accession value of the built-in electric field could be estimated by using the applied voltage divided by the thickness of i-GaInP layer. The theoretical value of the increased electric field when one-volt voltage is provided should be 40.0, 20.0, 13.3, and 10.0 kV/cm for samples A to D, respectively. The theoretical and experimental values are listed in Table 1. It could be found that the experimental values match well with the theoretical values when the thickness of the i-GaInP layer is small, such as samples A and B, but gradually deviate from the theoretical value as the thickness is larger than 0.75 μm . For sample D, the accession value is only one-third of the theoretical value. According to this result, it is clear that the crystal quality of the thin i-GaInP layer is quite good and no defect dipoles existing in this layer, results in that all of the reverse bias has

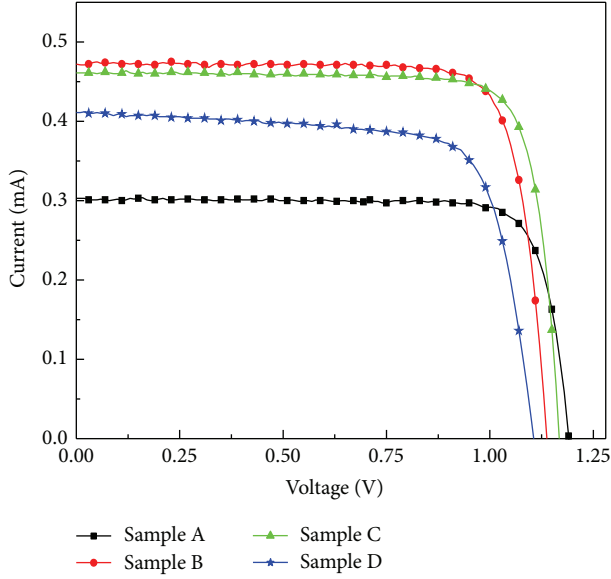


FIGURE 7: The I - V characteristics of samples A~D obtained under sun illumination.

been applied on this layer. On the other hand, the i -GaInP layer quality of sample D is not good enough due to a large number of point defects, which became charged dipoles as the reverse bias was applied and reduced the accession value of the electric field [22, 23].

Figure 7 shows the I - V characteristics of samples A to D obtained under sun illumination. A lot of parameters relating to solar cell circuit could be extracted from I - V curves such as I_{sc} , V_{oc} , R_{sh} , and R_s [24–26]. I_{sc} represents the maximum current at short circuit circumstance and reflects the capability of generating current. We can observe that samples B and C have high values of I_{sc} , while samples A and D have low I_{sc} . However, the I_{sc} was measured by a solar simulator consisting of the whole sun spectra, and their results are similar to the integration of the PC spectra. The integrated values for samples A to D are 63, 76, 71, and 66 nA, respectively. This result indicates the same trend like that we have observed in I_{sc} values. We could further confirm that the suitable i -layer thickness for good performance is between 0.5 and 0.75 μm . Štulík and Singh proposed the influence of defects on I_{sc} for Si based solar cell indicating worse i -layer crystal quality would cause lower I_{sc} value [27]. Therefore, the low I_{sc} values for samples A and D reflect many defects existing in the i -layer with a unsuitable thickness.

The open circuit voltage, V_{oc} , is the maximum voltage available from a junction solar cell, and it occurs at zero currents. The V_{oc} values were obtained from the intersection of the I - V curve and the horizontal axis voltages; these values are 1.19, 1.14, 1.17, and 1.11 V for samples A to D. For single-junction solar cells, V_{oc} could be determined as $V_{oc} = (nk_B T/q) \ln(J_{sc}/J_o + 1)$, where kT/q is the thermal voltage, n is the ideality factor, J_o is saturation current, and J_{sc} is short circuit current density. In general, the saturation current density depends on recombination in the solar cell; therefore, V_{oc} is a measure of the amount of recombination in the device.

TABLE 2: Photovoltaic performances of samples A~D.

Sample	A	B	C	D
V_{oc} (V)	1.19	1.14	1.17	1.11
I_{sc} (mA)	0.30	0.47	0.46	0.41
V_{max} (V)	1.02	0.98	1.03	0.93
I_{max} (mA)	0.29	0.44	0.43	0.36
P_{max} (mW)	0.30	0.43	0.44	0.34
FF (%)	82	81	82	74
η (%)	3.28	4.82	4.88	3.76
R_{sh} (K Ω)	147	137	107	82
R_s (Ω)	123	127	129	246

For sample D, the V_{oc} reduction is obvious, which may be related to the enhanced generation of the saturation current determined by various mechanisms such as the recombination current of defects or diffusion current [28]. Furthermore, the two equivalent resistances connected in series (R_s) and in shunt (R_{sh}) also can be extracted from the slope of I - V curves at open circuit and short circuit circumstances, respectively. The results have been summarized in Table 2. For an efficient solar cell, low R_s and large R_{sh} features are necessary which decrease power loss of solar cell in addition to affecting FF. Table 2 shows that the R_s increases a little from samples A to C and causes a dramatic jump for sample D. We think that the increase in R_s is responsible for the increase of the i -layer thickness [29]. For sample D, a lot of point defects in the i -layer resist the current flow and result in a high series resistance. The resistance of R_{sh} decreases a little from samples A to C and decreases dramatically for sample D. This decrease of R_{sh} is responsible for the increase of the nonradiative recombination centers coming from point defects in the i -layer. In general, the fill factor (FF) value could reflect the performance of solar cell. When FF is closed to 100% which means the solar cells possess ideal I - V characteristic and allow maximum power delivered to the load, the FF is defined as the ratio of maximum power to the product of I_{sc} and V_{oc} . Either a large R_s or a small R_{sh} will reduce the FF. According to the information in Table 2 we organized, the relevant results of sample A show low R_s and large R_{sh} features reflecting a good FF property. In contrast, a poor FF property of the sample D could be reasonable due to a high R_s and a low R_{sh} .

Another key performance characteristic of a solar cell is the efficiency η , which is the ratio of maximum out power to the incidental light power. Table 2 shows the η values for samples A to D are between 3 and 5%. According to a previous literature [30], Shu et al. proposed that the conversion efficiency of GaInP p - i - n solar cells could achieve around 5% with 1 mA/cm² photocurrent density generated using similar measurement methods to ours. In our cases, no antireflection coating layer applied in our devices is probable a reason for low efficiency. From the data shown in Table 2, it could be found that samples B and C have better efficiency than samples A and D. From these key performance characteristics, we can understand that the optimized thickness of the i -layer is critical and in the range around 0.5 to 0.75 μm . The crystal quality of the i -layer is dependent on the thickness

of the i-layer. Both the performance and the built-in electric field of solar cells actually rely on a suitable thickness of i-layer with high quality.

4. Conclusions

In conclusion, we have presented the study on built-in electric fields and optical properties of GaInP p-i-n solar cells with different i-layer thicknesses. A series of experiments determined the built-in electric field strengths and i-layer quality for all samples and confirmed that the optimized i-layer thickness is around 0.5 to 0.75 μm . For the sample with thinner i-layer thickness, solar cells could not absorb all of the sun light efficiently. Therefore, the short circuit current and output power would be low. In addition, a lot of point defects are generated in the sample with thicker layer and the built-in electric field is not high enough to drive out all of photo-induced current.

Conflict of Interests

The authors declare that there is no conflict of interests regarding the publication of this paper.

Acknowledgment

The authors would like to acknowledge the financial support of the National Science Council, Taiwan, under Contract NSC 100-2112-M-018-002.

References

- [1] R. R. King, D. C. Law, K. M. Edmondson et al., "40% efficient metamorphic GaInP/GaInAs/Ge multijunction solar cells," *Applied Physics Letters*, vol. 90, no. 18, Article ID 183516, 2007.
- [2] D. Shahrjerdi, S. W. Bedell, C. Ebert et al., "High-efficiency thin-film InGaP/InGaAs/Ge tandem solar cells enabled by controlled spalling technology," *Applied Physics Letters*, vol. 100, no. 5, Article ID 053901, 2012.
- [3] I. Serdiukova, C. Monier, M. F. Vilela, and A. Freundlich, "Critical built-in electric field for an optimum carrier collection in multiquantum well p-i-n diodes," *Applied Physics Letters*, vol. 74, no. 19, pp. 2812–2814, 1999.
- [4] F. H. Pollak and H. Shen, "Modulation spectroscopy of semiconductors: bulk/thin film, microstructures, surfaces/interfaces and devices," *Materials Science and Engineering: R: Reports*, vol. 10, no. 7-8, pp. 275–374, 1993.
- [5] R. Henninger, J. Klaer, K. Siemer, J. Bruns, and D. Bräunig, "Electroreflectance of CuInS₂ thin film solar cells and dependence on process parameters," *Journal of Applied Physics*, vol. 89, no. 5, pp. 3049–3054, 2001.
- [6] R. G. Rodrigues, I. Bhat, J. M. Borrego, and R. Venkatasubramanian, "Photorefectance characterization of InP and GaAs solar cells," in *Proceedings of the 23rd IEEE Photovoltaic Specialists Conference*, pp. 681–685, Louisville, Ky, USA, May 1993.
- [7] D. Y. Lin, W. C. Lin, F. L. Wu et al., "Investigations of interdiffusion in InGaAsP multiple-quantum-well structures by photorefectance," *Physica Status Solidi A*, vol. 206, no. 5, pp. 791–795, 2009.
- [8] D. Y. Lin, Y. S. Huang, T. S. Shou, K. K. Tiong, and F. H. Pollak, "Temperature-dependent contactless electroreflectance and photoluminescence study of GaAlAs/InGaAs/GaAs pseudomorphic high electron mobility transistor structures," *Journal of Applied Physics*, vol. 90, no. 12, pp. 6421–6427, 2001.
- [9] J. Y. Zheng, D. Y. Lin, and Y. S. Huang, "Piezoreflectance study of band-edge excitons of ReS₂: Au," *Japanese Journal of Applied Physics*, vol. 48, Article ID 052302, 2009.
- [10] F. H. Pollak, H. Qiang, D. Yan, W. Krysten, and S. Moneger, "Contactless electromodulation for the nondestructive, room-temperature analysis of wafer-sized semiconductor device structures," *IEEE Journal of Selected Topics in Quantum Electronics*, vol. 1, no. 4, pp. 1002–1010, 1995.
- [11] D. Y. Lin, J. D. Wu, C. C. Hung et al., "Optical investigation of an AlGaIn/GaN interface with the presence of a two-dimensional electron gas," *Physica E: Low-Dimensional Systems and Nanostructures*, vol. 43, no. 1, pp. 125–129, 2010.
- [12] S. Kamiyama, T. Uenoyama, M. Manno, Y. Ban, and K. Ohnaka, "Analysis of GaInP/AlGaInP compressive strained multiple-quantum-well laser," *IEEE Journal of Quantum Electronics*, vol. 30, no. 6, pp. 1363–1369, 1994.
- [13] Y. Yu, X. Zhang, B. Huang et al., "Strain effect and characteristics of GaInP/AlGaInP strain-compensated multiple quantum wells," *Materials Science and Engineering: B*, vol. 97, no. 3, pp. 211–216, 2003.
- [14] D. Y. Lin, Y. S. Huang, and K. K. Tiong, "A second-harmonic electroreflectance study of a coupled GaAs–AlGaAs double quantum well," *Semiconductor Science and Technology*, vol. 12, no. 9, pp. 1111–1115, 1997.
- [15] H. I. Ralph, "On the theory of the Franz-Keldysh effect," *Journal of Physics C: Solid State Physics*, vol. 1, no. 2, p. 378, 1968.
- [16] H. Shen and F. H. Pollak, "Generalized Franz-Keldysh theory of electromodulation," *Physical Review B*, vol. 42, no. 11, pp. 7097–7102, 1990.
- [17] H. Shen and M. Dutta, "Franz-Keldysh oscillations in modulation spectroscopy," *Journal of Applied Physics*, vol. 78, no. 4, pp. 2151–2176, 1995.
- [18] C. H. Chan, M. C. Chen, H. H. Lin, Y. F. Chen, and G. J. Jan, "Characterization of piezoelectric (111)B InGaAs/GaAs p-i-n quantum well structures using photorelectance spectroscopy," *Applied Physics Letters*, vol. 72, article 1208, 1998.
- [19] C. H. Chan, Y. F. Chen, M. C. Chen, H. H. Lin, G. J. Jan, and Y. H. Chen, "Photorelectance spectroscopy of strained-layer (111)B InGaAs/GaAs quantum well diodes," *Journal of Applied Physics*, vol. 84, no. 3, pp. 1595–1601, 1998.
- [20] Y. S. Huang and F. H. Pollak, "Non-destructive, room temperature characterization of wafer-sized III–V semiconductor device structures using contactless electromodulation and wavelength-modulated surface photovoltage spectroscopy," *Physica Status Solidi A*, vol. 202, no. 7, pp. 1193–1207, 2005.
- [21] T. J. C. Hosea, S. A. Cripps, T. E. Sale, and K. Hild, "Analysis of reflectance and modulation spectroscopic lineshapes in optoelectronic device structures," *Applied Surface Science*, vol. 253, no. 1, pp. 70–79, 2006.
- [22] A. Podolian, V. Kuryliuk, and O. Korotchenkov, "Rf strain-controlled built-in electric field near SiO₂/SiGe interface," *Solar Energy Materials and Solar Cells*, vol. 93, no. 11, pp. 1946–1951, 2009.
- [23] X. J. Shang, J. F. He, H. L. Wang et al., "Effect of built-in electric field in photovoltaic InAs quantum dot embedded GaAs solar cell," *Applied Physics A*, vol. 103, no. 2, pp. 335–341, 2011.

- [24] K. W. J. Barnham, B. Braun, J. Nelson et al., "Short-circuit current and energy efficiency enhancement in a low-dimensional structure photovoltaic device," *Applied Physics Letters*, vol. 59, no. 1, pp. 135–137, 1991.
- [25] M. Chegaar, Z. Ouennoughi, F. Guechi, and H. Langueur, "Determination of solar cells parameters under illuminated conditions," *Journal of Electron Devices*, vol. 2, pp. 17–21, 2003.
- [26] M. J. Morgan, G. Jakovidis, and I. McLeod, "An experiment to measure the I-V characteristics of a silicon solar cell," *Physics Education*, vol. 29, no. 4, pp. 252–254, 1994.
- [27] P. Štulík and J. Singh, "A simple method to simulate the influence of defects on the short circuit current in amorphous silicon solar cells," *Journal of Non-Crystalline Solids*, vol. 226, no. 3, pp. 299–303, 1998.
- [28] T. Tayagaki, Y. Hoshi, and N. Usami, "Investigation of the open-circuit voltage in solar cells doped with quantum dots," *Scientific Reports*, vol. 3, article 2703, 2013.
- [29] T. Taima, M. Chikamatsu, Y. Yoshida, K. Saito, and K. Yase, "Effects of intrinsic layer thickness on solar cell parameters of organic p-i-n heterojunction photovoltaic cells," *Applied Physics Letters*, vol. 85, no. 26, pp. 6412–6414, 2004.
- [30] G. W. Shu, J. J. Yang, I. J. Shu et al., "Dependence of biasing voltage and illumination power on the built-in electric field of InGaP solar cells," *Japanese Journal of Applied Physics*, vol. 51, no. 7, Article ID 072301, 2012.

Research Article

Plasmon-Enhanced Photoluminescence of an Amorphous Silicon Quantum Dot Light-Emitting Device by Localized Surface Plasmon Polaritons in Ag/SiO_x:a-Si QDs/Ag Sandwich Nanostructures

Tsung-Han Tsai, Ming-Yi Lin, Wing-Kit Choi, and Hoang Yan Lin

Graduate Institute of Photonics and Optoelectronics and Department of Electrical Engineering, National Taiwan University, No. 1, Section 4, Roosevelt Road, Taipei 106, Taiwan

Correspondence should be addressed to Hoang Yan Lin; hoangyanlin@ntu.edu.tw

Received 19 December 2014; Accepted 30 March 2015

Academic Editor: Jun Zhu

Copyright © 2015 Tsung-Han Tsai et al. This is an open access article distributed under the Creative Commons Attribution License, which permits unrestricted use, distribution, and reproduction in any medium, provided the original work is properly cited.

We investigated experimentally the plasmon-enhanced photoluminescence of the amorphous silicon quantum dots (a-Si QDs) light-emitting devices (LEDs) with the Ag/SiO_x:a-Si QDs/Ag sandwich nanostructures, through the coupling between the a-Si QDs and localized surface plasmons polaritons (LSPPs) mode, by tuning a one-dimensional (1D) Ag grating on the top. The coupling of surface plasmons at the top and bottom Ag/SiO_x:a-Si QDs interfaces resulted in the localized surface plasmon polaritons (LSPPs) confined underneath the Ag lines, which exhibit the Fabry-Pérot resonance. From the Raman spectrum, it proves the existence of a-Si QDs embedded in Si-rich SiO_x film (SiO_x:a-Si QDs) at a low annealing temperature (300°C) to prevent the possible diffusion of Ag atoms from Ag film. The photoluminescence (PL) spectra of a-Si QDs can be precisely tuned by a 1D Ag grating with different pitches and Ag line widths were investigated. An optimized Ag grating structure, with 500 nm pitch and 125 nm Ag line width, was found to achieve up to 4.8-fold PL enhancement at 526 nm and 2.46-fold PL integrated intensity compared to the a-Si QDs LEDs without Ag grating structure, due to the strong a-Si QDs-LSPPs coupling.

1. Introduction

Silicon quantum dots (Si QDs) light-emitting devices (LEDs) have been intensively investigated as a promising light source in recent years, for the next generation of Si-based optoelectronic integrated circuits (OEICs) [1–4]. The advantage of Si QDs LEDs lies in the compatible fabrication process with complementary metal-oxide-semiconductor (CMOS) and the low cost fabrication. However, realizing practical applications for Si QDs LEDs in OEICs requires high emission intensity, narrow spectral band, and low-temperature synthesis of Si QDs. Recently, surface plasmons (SPs), both surface plasmon polaritons (SPPs) and localized surface plasmon polaritons (LSPPs), have attracted a great deal of attention for their significant enhancements of photoluminescence (PL) intensity by coupling Si QDs into the near-field of SPs [5–8]. Meanwhile, the modified electromagnetic response of SPs in metal-insulator-metal (MIM) sandwich nanostructures

through the coupling of SPs has been widely studied [9–16]. The coupling interaction via near-fields strongly depends on the thickness of the insulator and the structure parameter of texturing metallic surfaces. According to Fermi's golden rule, the electrical field intensity and the density of states of the LSPPs mode at the emitter position are directly related to the radiative recombination rate (Γ_{rad}) for exciton dipoles of a-Si QDs [17, 18]:

$$\Gamma_{\text{rad}} = \frac{2\pi}{\hbar} \left| \langle f | \vec{\mu} \cdot \vec{E} | i \rangle \right|^2 \rho(\omega), \quad (1)$$

where μ denotes the exciton dipole moment of a-Si QDs, E is the electrical field intensity, and $\rho(\omega)$ is the density of states of the LSPPs mode. The radiative recombination rate of a-Si QDs can be greatly enhanced by a-Si QDs-LSPPs coupling, resulting in an increase in the PL intensity of a-Si QDs. Although the enhancement of PL intensity of crystalline Si QDs (c-Si QDs) has been reported through SPs coupling

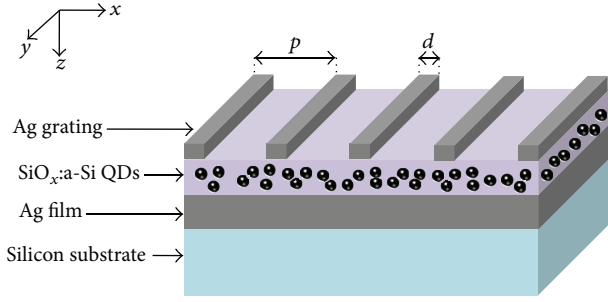


FIGURE 1: Schematic view of a-Si QDs LEDs with a Ag/SiO_x:a-Si QDs/Ag sandwich nanostructures.

TABLE 1: The structural parameters of samples A–E, and the Ag grating with Ag line width d and pitch p on the SiO_x:a-Si QDs film. Sample A is the reference sample without Ag grating structure.

Sample	d	p	d/p
A	—	—	—
B	100 nm	400 nm	0.25
C	125 nm	500 nm	0.25
D	150 nm	600 nm	0.25
E	175 nm	700 nm	0.25

effect [5–8], there has been no previous report concerning the enhanced PL intensity of a-Si QDs LEDs through a-Si QDs-LSPPs coupling, within the MIM sandwich nanostructures. In this paper, we report the enhanced PL integrated intensity and the narrower full width at half-maximum (FWHM) of the PL spectra for a-Si QDs LEDs, with the Ag/SiO_x:a-Si QDs/Ag sandwich nanostructures relative to the a-Si LEDs without Ag grating, resulting from the strong coupling between a-Si QDs and LSPPs. The maximum 4.8-fold PL enhancement factor and 246% enhancement of PL integrated intensity have been observed, for an optimized Ag grating structure by a strong a-Si QDs-LSPPs coupling. We also prove the formation of a-Si QDs embedded in Si-rich SiO_x film (SiO_x:a-Si QDs) with low annealing process (300°C) and that the measured PL spectra of SiO_x:a-Si QDs originate from the quantum confinement effect (QCE) [19–22].

2. Experiments

The fabrication process of the trilayer Ag/SiO_x:a-Si QDs/Ag sandwich nanostructures is described as follows. Silicon substrate was first coated with a 100 nm-thick Ag film using thermal evaporation. Then, the 100 nm-thick Si-rich SiO_x (SRO, $x < 2$) film was deposited on the Ag film by using plasma enhanced chemical vapor deposition (PECVD) system at the pressure of 67 Pa with nitrogen-diluted 5% SiH₄ and N₂O as the reactant gas sources. The flow rate of N₂O gas was maintained at 30 sccm and the SiH₄/N₂O flow rate ratio of 5.53:1. The sample was heated to 350°C and the radio frequency power was kept at 30 W during the SRO film growth. After the deposition, the SRO film was annealed at 300°C for 1 hr in a quartz furnace with flowing N₂ gas, to form a SiO_x:a-Si QDs film. Then, a 1D periodic Ag grating was fabricated on

the top of SiO_x:a-Si QDs film using electron-beam (e-beam) lithography (Elionix ELS-7500) and liftoff process. First, a 300 nm-thick positive-type e-beam resist (Nippon Zeon ZEP-520A) is spun on the top of sample followed by the subsequent e-beam lithography to define the grating pattern with the pitch p and line width d . The duty cycle (d/p) of Ag grating is fixed at 25%. Second, a 50 nm-thick Ag film is deposited onto the patterned e-beam resist and the Ag grating is fabricated by liftoff process in an exclusive remover (Nippon Zeon ZDMAC). Figure 1 shows the schematic representation of device with Ag/SiO_x:a-Si QDs/Ag sandwich nanostructures. The structural parameters of devices (samples A–E) are listed in Table 1. Scanning electron microscopy (SEM) images of Ag gratings (samples B–E) are shown in Figure 2. The room-temperature photoluminescence (PL) spectra were acquired under the excitation from a He-Cd laser operating at $\lambda_{\text{excitation}} = 325$ nm and with an average power of 50 mW. The PL intensity within 350 nm and 750 nm was recorded using a monochromator (CVI DK240) in conjunction with a photomultiplier (Hamamatsu R928) and a digital multimeter (HP 34401A). The reflection spectra were measured in an optical microscope consisting of a monochromator (Horiba Jobin Yvon iHR 320) and a broadband halogen lamp as a white light source incident through a 20x objective (NA = 0.75) to the normal of the metal surface (z -axis). And the reflected light was collected with the same objective. The refraction index of Si-rich SiO_x film was determined by an ellipsometer (JA Woollam M-2000DI). The thickness of each Ag film and SiO_x:a-Si QDs film was measured by an atomic force microscope (AFM, Veeco D5000). The Si/O composition ratio and concentration-depth profile of SRO film were measured by X-ray photoelectron spectroscopy (XPS, Thermo Fisher Scientific Theta probe). The existence and the size of a-Si QDs were measured by a Raman spectroscopy (Horiba Jobin Yvon T64000).

3. Results and Discussions

3.1. Material Analysis of SiO_x:a-Si QDs Film. Figure 3(a) shows that the concentration-depth profiles of the SiO_x:a-Si QDs film were performed by using Si 2p, O 1s, and Ag 3d peaks from XPS analysis. The average Si concentration of the SiO_x:a-Si QDs film is about 48.27 at. %. High Si/O composition ratio for the SiO_x:a-Si QDs film is observed, due to the high SiH₄/N₂O flow rate ratio of 5.53:1 during the PECVD growth. Since there are excessive Si atoms and insufficient O atoms, the Si atoms could move simply and accumulate to form a-Si QDs, without being restrained by Si-O bonds of the SiO_x film during the annealing process [23, 24]. Hence, we conclude that the a-Si QDs can be synthesized at a low annealing temperature (300°C). The Ag atoms did not diffuse into the SiO_x:a-Si QDs film from bottom Ag film after annealing process, as shown in Figure 3(a). Raman spectroscopy was used to analyze the size of Si QDs through the energy shift of the Raman peak and the correspondent line broadening [25]. Figure 3(b) shows that the Raman spectrum of SiO_x:a-Si QDs film can be separated into two components. One component corresponds to the a-Si QDs, exhibiting a

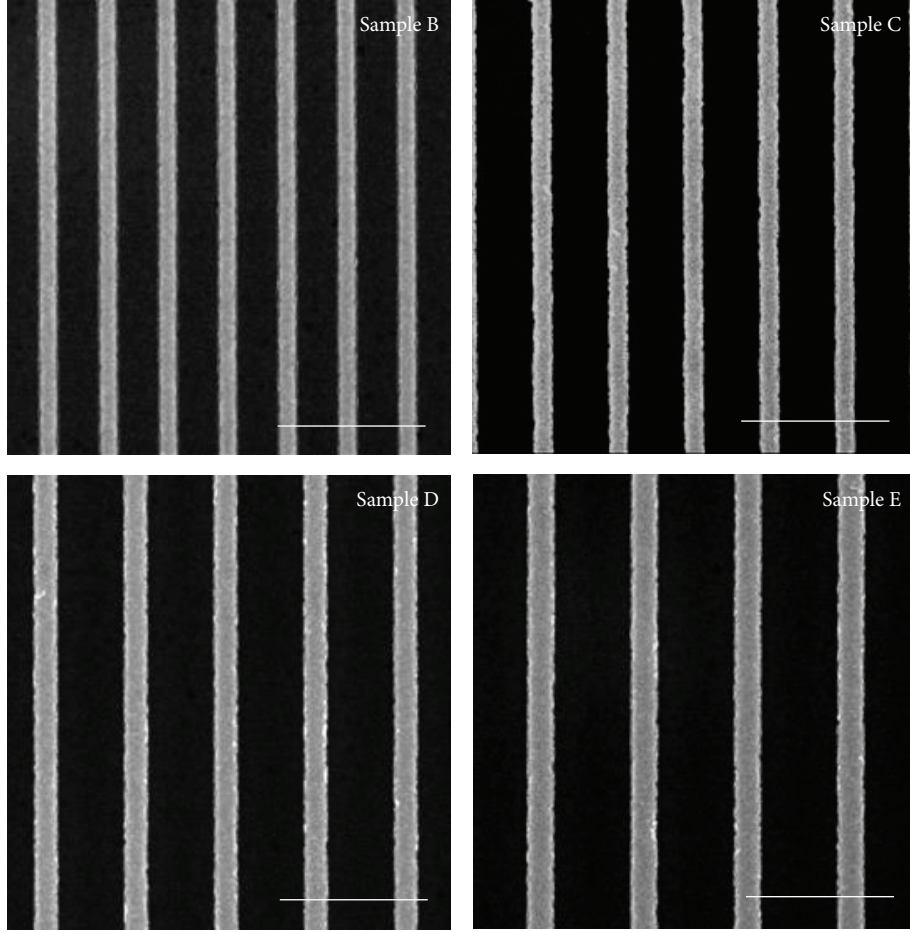


FIGURE 2: SEM images of a series of Ag gratings (samples B–E). Scale bar is $1\ \mu\text{m}$.

peak at $490\ \text{cm}^{-1}$ with a FWHM of $33\ \text{cm}^{-1}$. The Raman downshift and FWHM value show that the sizes of a-Si QDs are about 1.7 nm. Figure 3(c) presents the room-temperature PL spectrum of a-Si QDs LEDs without Ag grating structure (sample A), showing that the center emission wavelength is about 510 nm. The center emission wavelength of our 1.7 nm-sized a-Si QDs shows a good agreement with the theoretical study of light emission properties of SiO_x :a-Si QDs film [20]. Hence, the existence of a-Si QDs embedded in the SiO_x matrix with the low annealing process (300°C) is hereby proved by the Raman spectrum. Also, the main PL peak of a-Si QDs does not overlap with the PL spectrum from the oxygen related defects [26–28]. On the other hand, the smaller the a-Si QDs ($\sim 1.7\ \text{nm}$) are, the stronger the QCE is to surpass the interface state recombination [22, 29]. Hence, we conclude that the measured PL spectrum originates from the QCE of the a-Si QDs.

3.2. Optical Property Analysis (Sample A–D). The reflection spectra of samples B–E are shown in Figure 4 which exhibited reflection dips that can be attributed to the extinction due to the excitation of LSPs confined at the top Ag/SiO_x :a-Si QDs interface. It is because when the SiO_x :a-Si QDs film is thin enough, the SPPs excited at the top Ag/SiO_x :a-Si QDs

interface by TM-polarized light emitted by the a-Si QDs will couple with the SPPs at the bottom Ag/SiO_x :a-Si QDs interface via evanescent fields [11–16]. The strong coupling effect causes the excitation of LSPs, which exhibits the Fabry-Pérot resonance in the x direction between the two sidewalls of the Ag line [11–15]. It is found that the LSPs resonances satisfy this equation:

$$d \approx \frac{m\lambda}{2n_{\text{eff}}(\lambda)}, \quad (2)$$

where d is the Ag line width, λ is the resonance wavelength of the LSPs (the wavelength of the minimum reflection), n_{eff} is the effective refractive index of the SiO_x :a-Si QDs film at λ , and m is an integer (LSPs modes). The observed resonance wavelengths for each sample are 425 nm (sample B, $m = 1$), 526 nm (sample C, $m = 1$), 629 nm (sample D, $m = 1$), 731 nm, and 380 nm (sample E, $m = 1$ and $m = 2$), respectively. The LSPs resonance wavelength increases with the Ag line width. The original refraction indices of the SiO_x :a-Si QDs film that were determined by ellipsometer at 425, 526, 629, 731, and 380 nm are $n = 1.97, 1.95, 1.94, 1.93,$ and 1.99 , respectively. In our Ag/SiO_x :a-Si QDs/Ag sandwich nanostructures, the effective refraction index of SiO_x :a-Si QDs film increased to 1.076–1.083 times of the original values,

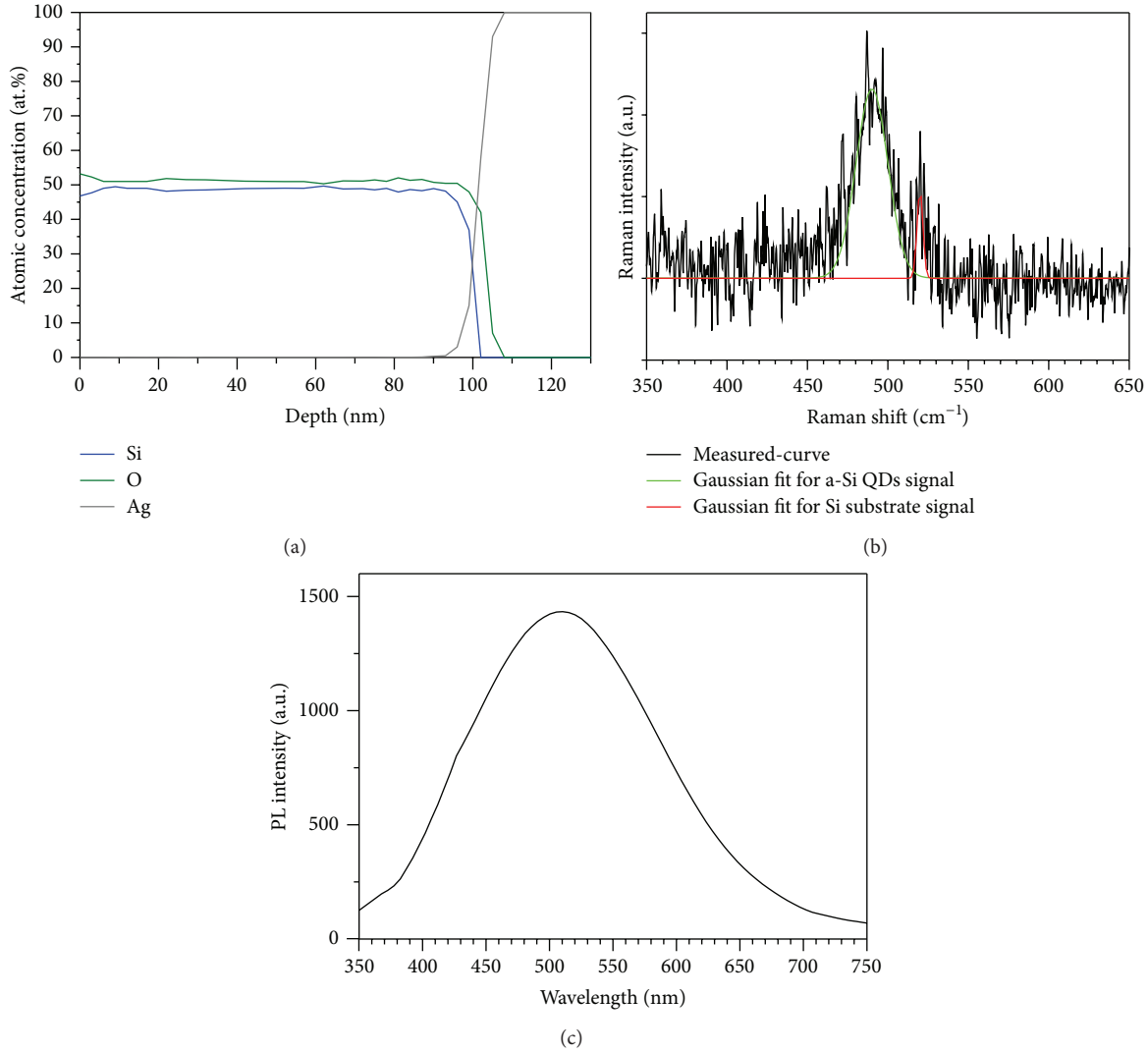


FIGURE 3: (a) XPS depth profiles for Si, O, and Ag elements in SiO_x :a-Si QDs film and at SiO_x :a-Si QDs film/Ag film interface. (b) Raman spectrum of SiO_x :a-Si QDs film. The spectrum is separated into two components corresponding to the a-Si QDs and the Si substrate (by Gaussian fit). (c) PL spectrum of sample A.

due to the interaction between LSPs and the induced image dipole (which has the opposite orientation) [30]. Figure 5 shows the measured room-temperature PL spectra of samples A–E. The PL integrated intensity of samples B–E has been enhanced compared to sample A as a reference sample by increasing the radiative recombination rate of a-Si QDs due to the coupling with LSPs mode. According to Fermi's golden rule [18], when the exciton dipole moments (μ) of a-Si QDs strongly couple to the near-field of LSPs, the radiative recombination rate of a-Si QDs can be enhanced by the large density of states of LSPs, resulting in an increase in emission intensity. The largest enhancement of the PL integrated intensity reaches 246% and the narrowest FWHM of 67 nm for sample C, due to the close match between the original center emission wavelength of a-Si QDs (510 nm) and the LSPs resonance wavelength (526 nm). Sample C shows the strongest a-Si QDs-LSPs coupling among samples

B–E. The mismatch between the original center emission wavelength of a-Si QDs and LSPs resonance wavelength for samples B, D, and E results in not only the lower enhancement of PL integrated intensity and broadened FWHM than sample C, but also the distorted emission spectra. Hence, the PL integrated intensities for samples B, D, and E are only enhanced by 172%, 161%, and 132%, respectively. For samples B, D, and E, the multiplexes in the PL spectra observed in Figure 5 correspond to the original emission peak of a-Si QDs and the respective excited LSPs modes as shown in Figure 4. The phenomenon is attributed to the increase in the electric field intensity and the density of states of the LSPs mode at the emitter position as the wavelength is near the LSPs resonance, resulting in the enhancements of the radiative recombination rate and the emission intensity. Also, the main PL peaks of samples B, D, and E were shifted from the original center emission wavelength of a-Si QDs towards

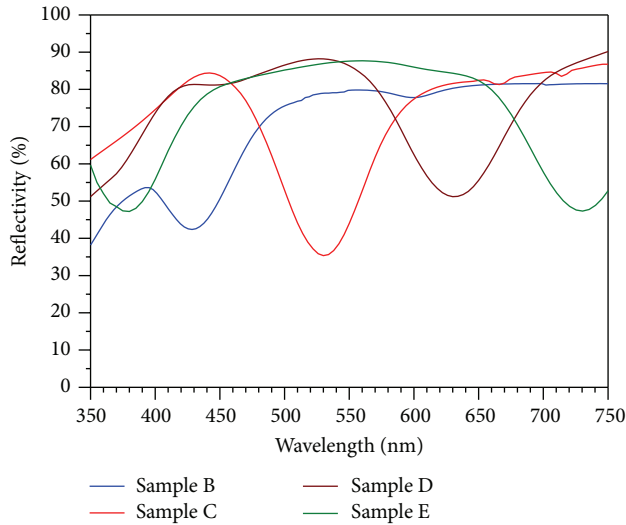


FIGURE 4: Reflection spectra of samples B–E.

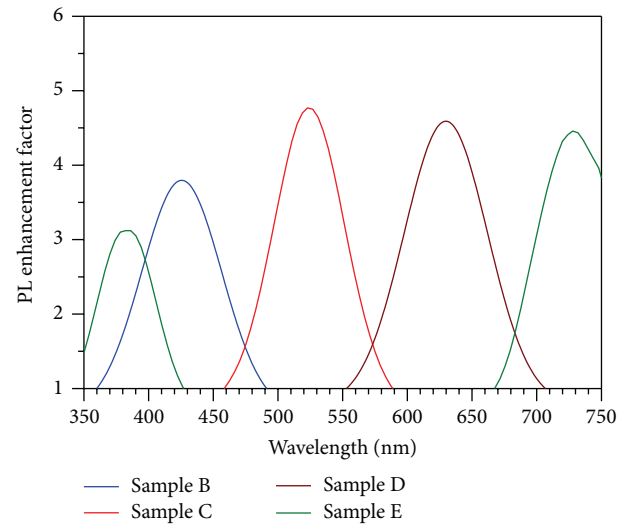


FIGURE 6: The plots of the PL enhancement factor of samples B–E.

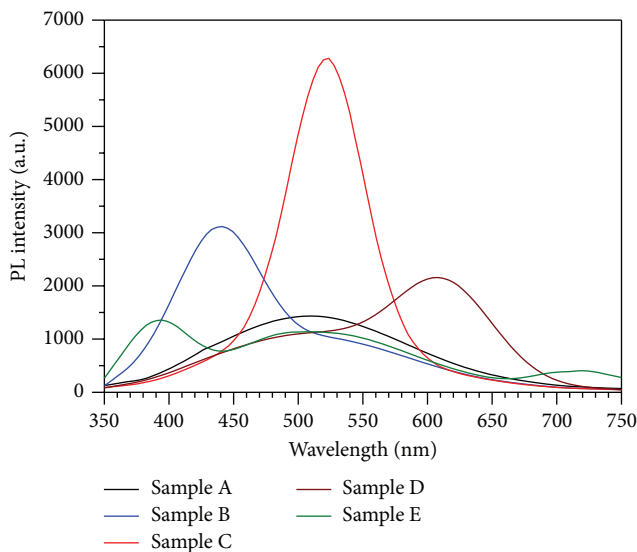


FIGURE 5: PL spectra of samples A–E.

the respective LSPRs resonance wavelengths. Figure 6 shows the plots of the PL enhancement factor, $I_{\text{grating}}(\lambda)/I_{\text{ref}}(\lambda)$, where $I_{\text{grating}}(\lambda)$ and $I_{\text{ref}}(\lambda)$ are the PL intensities for the samples with and without Ag grating. The plots of the PL enhancement factor show a redshift with an increase in the Ag line width that is similar to the tendency of reflection dips, and it indicates that the PL enhancement factor strongly corresponds with the LSPRs modes. From the results, a maximum PL enhancement factor of 4.8 was observed at 526 nm for sample C due to the strong a-Si QDs–LSPRs coupling. Therefore, it is worthwhile noticing the improved design of Ag grating structure by tuning the pitch and Ag line width for the largest PL integrated emission through the strong a-Si QDs–LSPRs coupling.

4. Conclusions

In conclusion, we proposed the plasmon-enhanced PL intensity of a-Si QDs LEDs with Ag/SiO_x:a-Si QDs/Ag sandwich nanostructures resulting from the strong coupling between a-Si QDs and LSPRs modes. It was found that the LSPRs were excited underneath the Ag lines, which exhibit the Fabry–Pérot resonance resulting from the coupling of SPPs between the top Ag grating and bottom Ag film. A narrowest 67 nm FWHM of PL spectrum, a maximum of 4.8-fold PL enhancement factor, and the largest 2.46-fold PL integrated intensity, compared to the a-Si QDs LEDs without Ag grating structure, have been observed for an optimized Ag grating structure by the strong a-Si QDs–LSPRs coupling.

Conflict of Interests

The authors declare that there is no conflict of interests regarding the publication of this paper.

Acknowledgments

The authors would like to acknowledge the Ministry of Science and Technology of Taiwan for the financial support of this research under Contracts nos. MOST 102-2221-E-002-205-MY3 and MOST 104-3113-E-155-001 and National Taiwan University under the Aim for Top University Projects 104R7607-4 and 104R8908.

References

- [1] D. A. B. Miller, "Silicon sees the light," *Nature*, vol. 378, no. 6554, p. 238, 1995.
- [2] L. Pavesi, L. Dal Negro, C. Mazzoleni, G. Franzò, and F. Priolo, "Optical gain in silicon nanocrystals," *Nature*, vol. 408, no. 6811, pp. 440–444, 2000.
- [3] P. M. Fauchet, "Light emission from Si quantum dots," *Materials Today*, vol. 8, no. 1, pp. 26–33, 2005.

- [4] G. Y. Sung, N.-M. Park, J.-H. Shin et al., "Physics and device structures of highly efficient silicon quantum dots based silicon nitride light-emitting diodes," *IEEE Journal on Selected Topics in Quantum Electronics*, vol. 12, no. 6, pp. 1545–1554, 2006.
- [5] B.-H. Kim, C.-H. Cho, J.-S. Mun et al., "Enhancement of the external quantum efficiency of a silicon quantum dot light-emitting diode by localized surface plasmons," *Advanced Materials*, vol. 20, no. 16, pp. 3100–3104, 2008.
- [6] J. S. Biteen, N. S. Lewis, H. A. Atwater, H. Mertens, and A. Polman, "Spectral tuning of plasmon-enhanced silicon quantum dot luminescence," *Applied Physics Letters*, vol. 88, no. 13, Article ID 131109, 2006.
- [7] J. S. Biteen, L. A. Sweatlock, H. Mertens, N. S. Lewis, A. Polman, and H. A. Atwater, "Plasmon-enhanced photoluminescence of silicon quantum dots: simulation and experiment," *The Journal of Physical Chemistry C*, vol. 111, no. 36, pp. 13372–13377, 2007.
- [8] H. Mertens, J. S. Biteen, H. A. Atwater, and A. Polman, "Polarization-selective plasmon-enhanced silicon quantum-dot luminescence," *Nano Letters*, vol. 6, no. 11, pp. 2622–2625, 2006.
- [9] S. A. Maier, "Plasmonic field enhancement and SERS in the effective mode volume picture," *Optics Express*, vol. 14, no. 5, pp. 1957–1964, 2006.
- [10] J.-J. Jiang, Y.-B. Xie, Z.-Y. Liu, X.-M. Tang, X.-J. Zhang, and Y.-Y. Zhu, "Amplified spontaneous emission via the coupling between Fabry–Perot cavity and surface plasmon polariton modes," *Optics Letters*, vol. 39, no. 8, pp. 2378–2381, 2014.
- [11] Y.-H. Ye, Y.-W. Jiang, M.-W. Tsai et al., "Localized surface plasmon polaritons in Ag/SiO₂/Ag plasmonic thermal emitter," *Applied Physics Letters*, vol. 93, no. 3, Article ID 033113, 3 pages, 2008.
- [12] Y.-H. Ye, Y.-W. Jiang, M.-W. Tsai et al., "Coupling of surface plasmons between two silver films in a Ag/SiO₂/Ag plasmonic thermal emitter with grating structure," *Applied Physics Letters*, vol. 93, no. 26, Article ID 263106, 2008.
- [13] S. Collin, F. Pardo, and J.-L. Pelouard, "Waveguiding in nanoscale metallic apertures," *Optics Express*, vol. 15, no. 7, pp. 4310–4320, 2007.
- [14] L. Martín-Moreno, F. J. García-Vidal, H. J. Lezec et al., "Theory of extraordinary optical transmission through subwavelength hole arrays," *Physical Review Letters*, vol. 86, article 1114, 2001.
- [15] C.-M. Wang, Y.-C. Chang, M.-W. Tsai et al., "Reflection and emission properties of an infrared emitter," *Optics Express*, vol. 15, no. 22, pp. 14673–14678, 2007.
- [16] S. A. Darmanyan and A. V. Zayats, "Light tunneling via resonant surface plasmon polariton states and the enhanced transmission of periodically nanostructured metal films: an analytical study," *Physical Review B*, vol. 67, no. 3, Article ID 035424, 7 pages, 2003.
- [17] J. Kümmerlen, A. Leitner, H. Brunner, F. R. Aussenegg, and A. Wokaun, "Enhanced dye fluorescence over silver island films: analysis of the distance dependence," *Molecular Physics*, vol. 80, no. 5, pp. 1031–1046, 1993.
- [18] E. Fermi, "Quantum theory of radiation," *Reviews of Modern Physics*, vol. 4, no. 1, pp. 87–132, 1932.
- [19] N.-M. Park, C.-J. Choi, T.-Y. Seong, and S.-J. Park, "Quantum confinement in amorphous silicon quantum dots embedded in silicon nitride," *Physical Review Letters*, vol. 86, no. 7, pp. 1355–1357, 2001.
- [20] K. Nishio, J. Kōga, T. Yamaguchi, and F. Yonezawa, "Theoretical study of light-emission properties of amorphous silicon quantum dots," *Physical Review B*, vol. 67, Article ID 195304, 2003.
- [21] G. G. Qin and Y. J. Li, "Photoluminescence mechanism model for oxidized porous silicon and nanoscale-silicon-particle-embedded silicon oxide," *Physical Review B*, vol. 68, no. 8, Article ID 085309, 7 pages, 2003.
- [22] C. Delerue, G. Allan, and M. Lannoo, "Theoretical aspects of the luminescence of porous silicon," *Physical Review B*, vol. 48, no. 15, pp. 11024–11036, 1993.
- [23] S. Mirabella, R. Agosta, G. Franzó et al., "Light absorption in silicon quantum dots embedded in silica," *Journal of Applied Physics*, vol. 106, no. 10, Article ID 103505, 2009.
- [24] B.-H. Lai, C.-H. Cheng, Y.-H. Pai, and G.-R. Lin, "Plasma power controlled deposition of SiO_x with manipulated Si quantum dot size for photoluminescent wavelength tailoring," *Optics Express*, vol. 18, no. 5, pp. 4449–4456, 2010.
- [25] G. Faraci, S. Gibilisco, P. Russo et al., "Si/SiO₂ core shell clusters probed by Raman spectroscopy," *The European Physical Journal B—Condensed Matter and Complex Systems*, vol. 46, no. 4, pp. 457–461, 2005.
- [26] G. H. Li, K. Ding, Y. Chen, H. X. Han, and Z. P. Wang, "Photoluminescence and Raman scattering of silicon nanocrystals prepared," *Journal of Applied Physics*, vol. 88, no. 3, pp. 1439–1442, 2000.
- [27] G.-R. Lin, C.-J. Lin, C.-K. Lin, L.-J. Chou, and Y.-L. Chueh, "Oxygen defect and Si nanocrystal dependent white-light and near-infrared electroluminescence of Si-implanted and plasma-enhanced chemical-vapor deposition-grown Si-rich SiO₂," *Journal of Applied Physics*, vol. 97, no. 9, Article ID 094306, 8 pages, 2005.
- [28] G.-R. Lin, C.-J. Lin, and K.-C. Yu, "Time-resolved photoluminescence and capacitance–voltage analysis of the neutral vacancy defect in silicon implanted SiO₂ on silicon substrate," *Journal of Applied Physics*, vol. 96, no. 5, article 3025, 3 pages, 2004.
- [29] X. X. Wang, J. G. Zhang, L. Ding et al., "Origin and evolution of photoluminescence from Si nanocrystals embedded in a SiO₂ matrix," *Physical Review B*, vol. 72, Article ID 195313, 2005.
- [30] A. Christ, G. Lévêque, O. J. Martin et al., "Near-field-induced tunability of surface plasmon polaritons in composite metallic nanostructures," *Journal of Microscopy*, vol. 229, no. 2, pp. 344–353, 2008.

Research Article

Fabrication of Hybrid Organic Photovoltaic Devices Using Electrostatic Spray Method

Zhe-Wei Chiu,¹ Yu-Jen Hsiao,² Te-Hua Fang,¹ and Liang-Wen Ji³

¹ Department of Mechanical Engineering, National Kaohsiung University of Applied Sciences, Kaohsiung 807, Taiwan

² National Nano Device Laboratories, National Applied Research Laboratories, Tainan 741, Taiwan

³ Institute of Electro-Optical and Materials Science, National Formosa University, Yunlin 632, Taiwan

Correspondence should be addressed to Te-Hua Fang; fang.tehua@msa.hinet.net

Received 29 April 2014; Revised 24 June 2014; Accepted 2 July 2014; Published 4 August 2014

Academic Editor: Ting-Jen Hsueh

Copyright © 2014 Zhe-Wei Chiu et al. This is an open access article distributed under the Creative Commons Attribution License, which permits unrestricted use, distribution, and reproduction in any medium, provided the original work is properly cited.

Hybrid organic photovoltaic devices (OPVDs) are fabricated using the electrostatic spray (e-spray) method and their optical and electrical properties are investigated. E-spray is used to deposit a hybrid film (P3HT:PCBM/nanodiamond) with morphology and optical characteristics onto OPVDs. The root-mean-square roughness and optical absorption increase with increasing nanodiamond content. The performance of e-spray is comparable to that of the spin-coating method under uniform conditions. The device takes advantage of the high current density, power conversion efficiency, and low cost. Nanodiamond improves the short-circuit current density and power conversion efficiency. The best performance was obtained with 1.5 wt% nanodiamond content, with a current density of 7.28 mA/cm² and a power conversion efficiency of 2.25%.

1. Introduction

Organic photovoltaic devices (OPVDs) have received attention for large-area manufacturing. The roll-to-roll printing process can be used to manufacture devices on flexible substrates with transparent electrode [1]. OPVDs can be fabricated using a solution-processed method, such as spin-coating (SC), gravure printing, dip-coating, screen printing, inkjet printing, and the electrostatic spray (e-spray) method. OPVDs with an efficiency of as high as 8.3% have been demonstrated [2].

The e-spray technique has been applied to OPVDs due to their high surface to volume ratio. Polymers [3], biomaterials [4], and metal oxides [5] with small feature sizes have been fabricated using this method. The morphology of e-spray droplets must be carefully controlled via several parameters, such as applied voltage, distance between nozzle and substrate, pressure, and solution injection rate. The performance of OPVDs is determined by the spray diameter and evaporation speed [6].

A solar cloth of P3HT:PCBM blend was fabricated using the electrospinning technique [7]. The power conversion

efficiency was up to 1.9% when the surface roughness was reduced by depositing a solvent consisting of o-dichlorobenzene and acetone via the e-spray method [6]. OPVDs with a power conversion efficiency that exceeds 3.25% have been produced using the e-spray method, which rearranges the boundaries and constructs more continuous interpenetrating networks by solvent vapor soaking treatment [8]. The e-spray method is a promising technique for the deposition of a polymer blend layer onto OPVDs with low cost, roll-to-roll processing, and large-area manufacturing. Nanodiamonds have received a lot of interest as a semiconductor material, due to their strong ultraviolet absorption and high thermal conductivity. Nanodiamonds (1.5 wt%) embedded in OPVDs via the spin-coating method can enhance efficiency and reliability [9]. The active layer of OPVDs doped with nanodiamond with a grain size of 50 nm was shown to have the highest efficiency [10].

The present study investigates P3HT:PCBM/nanodiamond hybrid film prepared for OPVDs using the e-spray method. The effects of nanodiamond content in OPVDs on the morphology, optical absorption, photoluminescence, and photovoltaic performance are determined.

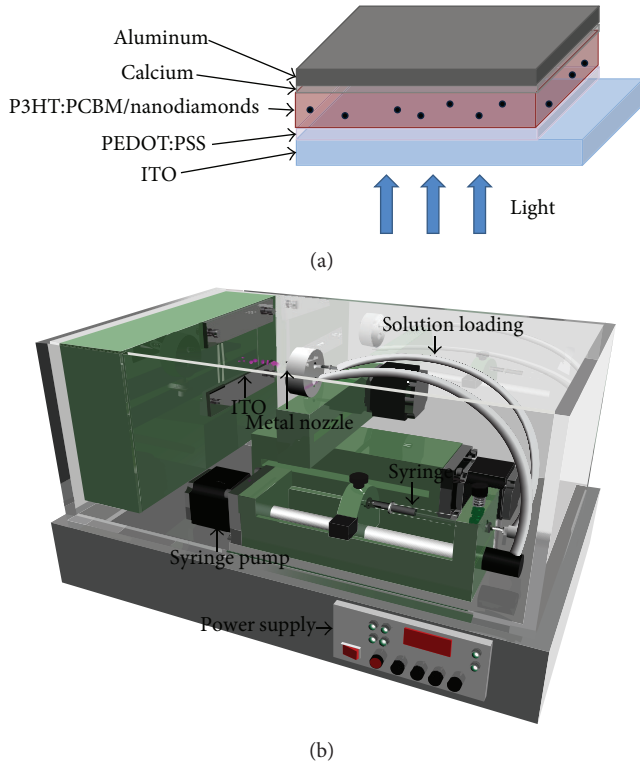


FIGURE 1: Schematics of (a) device structure with P3HT:PCBM/nanodiamond as the active layer and (b) e-spray method.

2. Experimental Procedure

Indium tin oxide (ITO) substrates were sequentially cleaned with acetone, isopropanol, and deionized water via ultrasonication for 10 min to remove contaminants and then etched with a pattern before being placed into a reactive ion etching system for oxygen plasma treatment to increase the ITO surface hydrophilicity. After PEDOT:PSS was spin-coated onto the substrates at 2600 rpm for 1 min, the samples were annealed at 120°C for 30 min. The active layer consisted of P3HT (FEM Inc.) and PCBM (Nano-C) (at a weight ratio of 1:0.8) dissolved in 1,2-dichlorobenzene (DCB) with various concentrations of nanodiamond (average grain size of about 50 nm). We have used nanodiamond (ND, ITRI Taiwan) of the sizes of about 50 nm, prepared by the detonation method. Figure 1(a) shows the device structure of the hybrid OPVDs in which the P3HT:PCBM/nanodiamond film was the active layer. A schematic of the e-spray method is shown in Figure 1(b). The distance between the metal nozzle and the substrate was 12 cm, the spray area was 6 cm², and the applied voltage was 10 kV. The hybrid solution was injected at a rate of 10 $\mu\text{L}\cdot\text{min}^{-1}$. The e-spray was applied to the substrate 12 times, each for 20 seconds. The active layer was annealed at 120°C for 15 min after being allowed to dry naturally. Then, a Ca buffer layer (25 nm) and an Al electrode (100 nm) were deposited onto the substrate via thermal evaporation. The active area was about 0.04 cm². All deposition processes were conducted at room temperature.

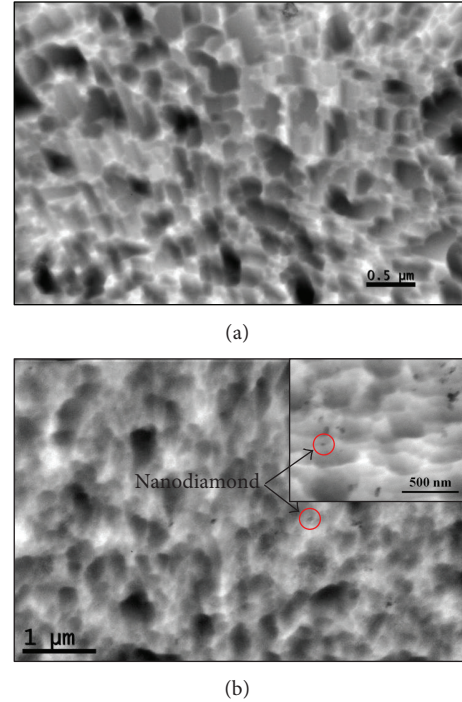


FIGURE 2: TEM images of films deposited by e-spray method: (a) P3HT:PCBM and (b) P3HT:PCBM doped with 1.5 wt% nanodiamond.

The morphology of the photoactive layer was measured with transmission electron microscopy (TEM) and atomic force microscopy (AFM). The absorption spectra were obtained using an ultraviolet-visible (UV-Vis) spectrometer (Hitachi, U-3010). The current-voltage measurements were obtained using a source meter (Keithley, 2410) and a solar simulator (TELTEC) with an AM1.5 filter under an irradiation intensity of 100 mW cm⁻². For external quantum efficiency (EQE) measurements, a xenon lamp (Oriel, 66150, 75 W) was used as the light source. All the samples were measured at room temperature.

3. Results and Discussion

The active layer was deposited via the e-spray method in a glove box and then annealed to reduce contact resistance with the electrodes. The crystallinity and hole transport of P3HT increased after annealing at 120°C [8]. By electrostatic spraying of the mixed liquid, the solution will be atomization form mutually exclusive electronic, the uniform surface on the substrate form atomized mixture. Spin-coating was used to form a smooth film surface. The surfaces of the films after e-spray deposition were quite rough, which is attributed to the evaporation of the solution and the solution injection rate. The morphology of the droplets was affected by the electron transfer of OPVDs. E-spray deposition must be determined before the film is already naturally dried because the performance of OPVDs would seriously be affected by morphology of the film surface. The parameters of the e-spray process must be carefully controlled. E-spray deposition uses

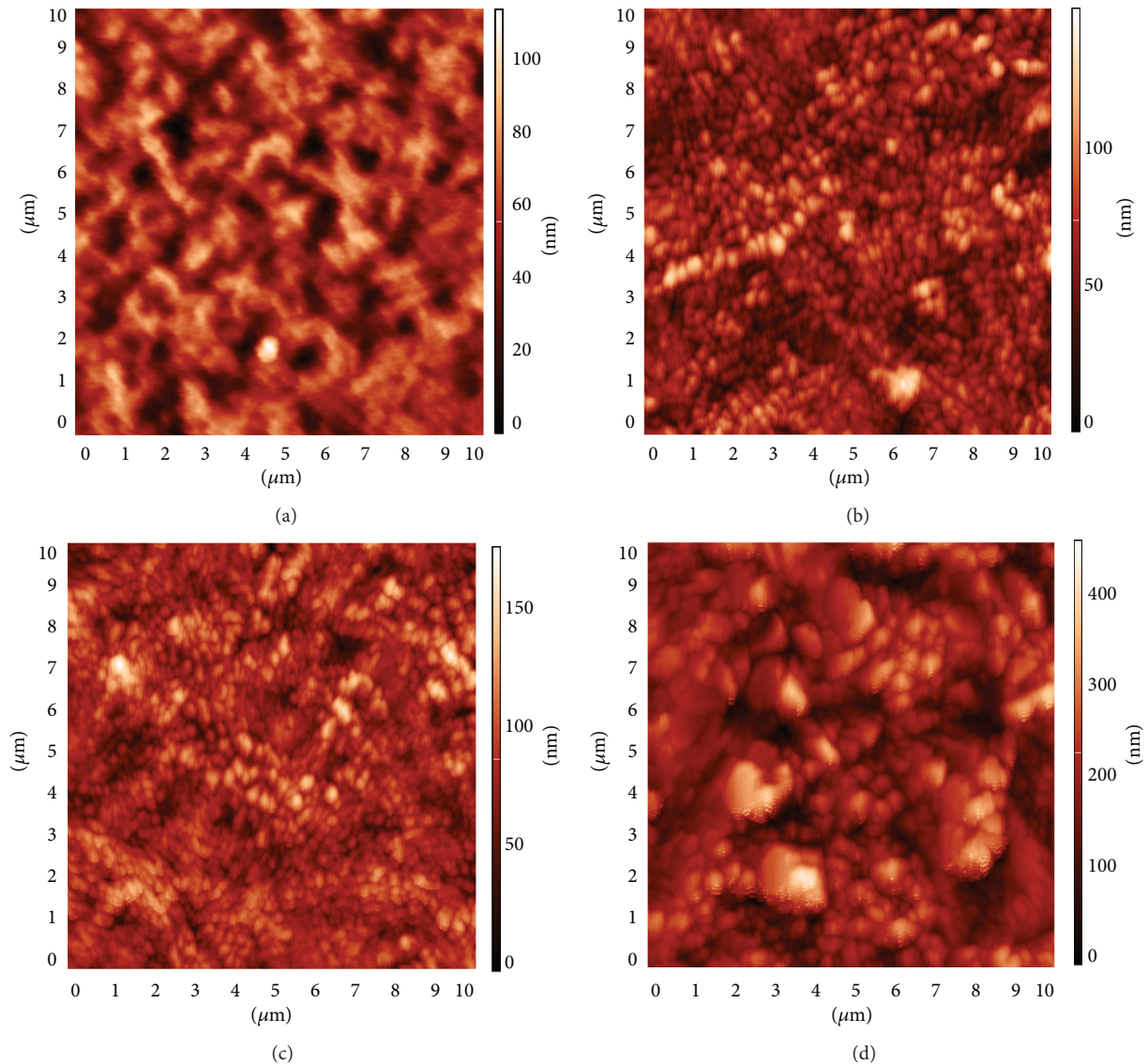


FIGURE 3: AFM images of P3HT:PCBM film doped with nanodiamond at concentrations of (a) 0, (b) 0.5, (c) 1.5, and (d) 3 wt%.

10% less polymer material than does the spin-coating method for a given film thickness. Using the e-spray method for the fabrication of the active layer of OPVDs thus reduces costs. The nanodiamond was dispersed in different film. The metal electrode has bad contact cause recombination of electrons and holes, this results induce e-spray has obvious irregular structure.

TEM images of PEDOT:PSS/P3HT:PCBM/nanodiamond film prepared via the e-spray method are shown in Figure 2. The grain size of P3HT:PCBM film (see Figure 1(a)) is about 200 nm. Particles aggregated to form large agglomerates, which then form the composite film with a continuous network structure. The surface area, number of donor/acceptor interfaces of the active layer, and thus charge generation were increased by the e-spray method. Figure 2(b) shows a TEM image of P3HT:PCBM/nanodiamond film. The nanodiamond was dispersed well and embedded in

the P3HT:PCBM (1:0.8) polymer quite uniformly. The average diameter of the nanodiamond was about 50 nm. OPVDs with this nanodiamond size exhibited highest power conversion efficiency in a previous study [10].

Figures 3(a)–3(d) show AFM images of P3HT:PCBM doped with nanodiamond at concentrations of 0, 0.5, 1.5, and 3 wt%, respectively. The e-sprayed films had root-mean-square (RMS) roughness values of 16.1, 17.3, 19.1, and 56.6 nm, respectively. The spin-coated film had an RMS roughness of 2.6 nm. The RMS roughness is higher for the e-sprayed films due to the stack deposition of spray droplets. The AFM surface morphology is shown high concentrations of nanodiamond induce the highest rougher surface.

Figure 4 shows optical absorption spectra for P3HT:PCBM doped with nanodiamond at concentrations of 0, 0.5, 1.5, and 3 wt%, respectively. The absorption in the range of 400 to 650 nm is attributed to the absorption of P3HT [11].

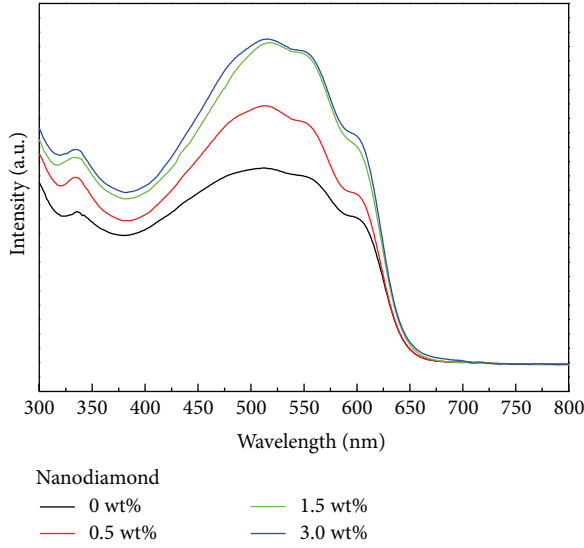


FIGURE 4: Absorption spectra of hybrid P3HT:PCBM film doped with nanodiamond at various concentrations.

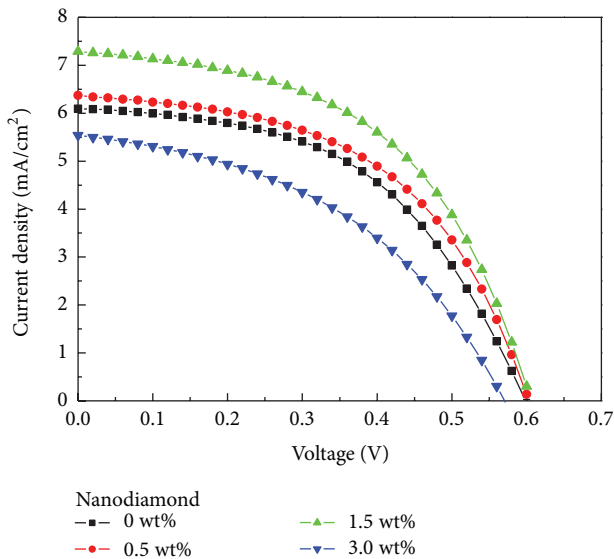


FIGURE 5: Current density-voltage characteristics of hybrid OPVDs doped with nanodiamond at various concentrations, under AM1.5G at $100 \text{ mW} \cdot \text{cm}^{-2}$ illumination.

The spectrum for the active film exhibited a small red shift when the nanodiamond concentration was increased from 0 to 3 wt%. The absorption intensity increased with increasing nanodiamond concentration. The nanodiamond created a scattering effect, which can lead to better absorption via the active layer. The doping nanodiamond in organic solar cell can increase the scattering effect of sunlight effectively. It could be attributed to the reflection and refraction of sunlight in organic hybrid active layer. The absorption intensity thus increased with increasing generation of electron-hole pairs by the nanodiamond, which enhances power conversion efficiency [12].

TABLE 1: Photovoltaic performance of investigated OPVDs doped with nanodiamond at various concentrations measured under AM1.5G at $100 \text{ mW} \cdot \text{cm}^{-2}$ illumination.

	V_{oc} (V)	J_{sc} (mA/cm^2)	FF (%)	η (%)
Standard	0.60	6.10	49.87	1.82
0.5%	0.60	6.37	51.33	1.96
1.5%	0.60	7.28	51.42	2.25
3.0%	0.58	5.54	43.04	1.38

The performance of OPVDs with active film doped with nanodiamond at various concentrations is shown in Table 1. Figure 5 shows the current density-voltage (J - V) characteristics of the e-sprayed hybrid OPVDs measured under an illumination intensity of $100 \text{ mW} \cdot \text{cm}^{-2}$. The photovoltaic performance of the 400 nm thick active layer spin-coated at 600 rpm was very similar to that of the e-sprayed layer. The open-circuit voltage, short-circuit current density, fill factor, and power conversion efficiency values of the OPVD obtained using the spin-coating method are 0.6 V, $5.4 \text{ mA} \cdot \text{cm}^{-2}$, 56.27%, and 1.82%, respectively. The short-circuit current density for the e-sprayed active layer is higher than that of the spin-coated layer. The fill factor of the e-sprayed active layer is lower because the active layer/metal electrode has imperfect contact with the roughness surface.

Hybrid OPVDs with P3HT:PCBM/nanodiamond films with nanodiamond levels of 0, 0.5, 1.5, and 3 wt% have power conversion efficiency values of 1.82%, 1.96%, 2.25%, and 1.38%, respectively. Nanodiamond improves the current density for concentrations up to 1.5 wt%, which is attributed to the absorption increase by the e-spray active layer. The results reveal that 1.5 wt% nanodiamond doping into OPVDs increases the short-circuit current density from 6.1 to $7.28 \text{ mA} \cdot \text{cm}^{-2}$. The power conversion efficiency of the hybrid OPVDs improved from 1.82% to 2.25%. However, when the concentration of nanodiamond exceeds 3 wt%, the efficiency decreases due to an increase in leakage current [13, 14]. In this study, we have achieved the performance $2.25 \pm 0.1\%$. The difference may lie in preparation of OPV hybrid film (e.g., process condition, machine, and material differences).

Figure 6 shows the EQE spectra for hybrid OPVDs with various nanodiamond concentrations measured at room temperature. The EQE spectra of the P3HT:PCBM/nanodiamond show a high conversion efficiency in the range of 300 to 650 nm [15]. Although all EQE spectra are similar in shape, the EQE values for the OPVDs doped with 1.5 wt% nanodiamond are higher than those for OPVDs doped with 0, 0.5, and 3 wt% nanodiamond for all wavelengths. This difference is due to an increase in the rate of exciton generation and increased probability of exciton dissociation, which enhance the short-circuit current density for P3HT:PCBM doped with 1.5 wt% nanodiamond.

4. Conclusion

E-sprayed P3HT:PCBM films doped with nanodiamond at various concentrations were investigated. Active layer has

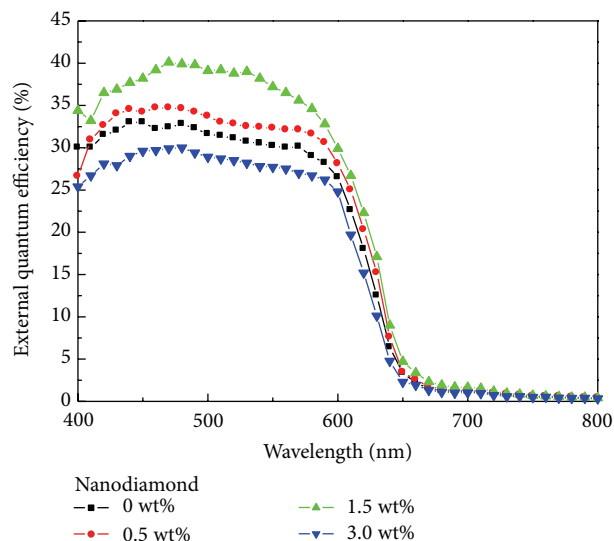


FIGURE 6: External quantum efficiency spectra of hybrid OPVDs doped with nanodiamond at various concentrations.

similarly stacked at e-spray method, AFM has the same trend when nanodiamond is over 1.5 wt%, and root-mean-square (RMS) roughness has significantly increased. Absorption spectra of both the intensities increase with the concentration being increased. The results reveal that 1.5 wt% nanodiamond doping into OPVDs increases the short-circuit current density from 6.1 to 7.28 mA·cm⁻² at e-spray method, which is due to e-spray increase interface with PEDOT:PSS and active layer. The e-spray is worse than spin-coating with fill factor, maybe the irregular structure form e-spray and metal electrode has bad contact cause recombination of electrons and holes. The best photovoltaic performance, in terms of short-circuit current density and power conversion efficiency, was obtained with 1.5 wt% nanodiamond doping. The e-spray method can possibly be used for flexible and large-area manufacturing.

Conflict of Interests

The authors declare that there is no conflict of interests regarding the publication of this paper.

Acknowledgment

The authors acknowledge the National Science Council of Taiwan for financially supporting this research under Grant NSC 100-2628-E-151-003-MY3.

References

[1] H. F. Dam and F. C. Krebs, "Simple roll coater with variable coating and temperature control for printed polymer solar cells," *Solar Energy Materials and Solar Cells*, vol. 97, pp. 191–196, 2012.

[2] B. Ratier, J. Nunzi, M. Aldissi, T. M. Kraft, and E. Buncel, "Organic solar cell materials and active layer designs—improvements with carbon nanotubes: a review," *Polymer International*, vol. 61, no. 3, pp. 342–354, 2012.

[3] Y. H. Lee, F. Mei, M. Y. Bai, S. Zhao, and D. R. Chen, "Release profile characteristics of biodegradable-polymer-coated drug particles fabricated by dual-capillary electrospray," *Journal of Controlled Release*, vol. 145, no. 1, pp. 58–65, 2010.

[4] S. Guha, M. Li, M. J. Tarlov, and M. R. Zachariah, "Electrospray-differential mobility analysis of bionanoparticles," *Trends in Biotechnology*, vol. 30, no. 5, pp. 291–300, 2012.

[5] L. Wang, H. W. Xu, P. C. Chen, D. W. Zhang, C. X. Ding, and C. H. Chen, "Electrostatic spray deposition of porous Fe₂O₃ thin films as anode material with improved electrochemical performance for lithium-ion batteries," *Journal of Power Sources*, vol. 193, no. 2, pp. 846–850, 2009.

[6] T. Fukuda, K. Takagi, T. Asano et al., "Bulk heterojunction organic photovoltaic cell fabricated by the electrospray deposition method using mixed organic solvent," *Physica Status Solidi—Rapid Research Letters*, vol. 5, no. 7, pp. 229–231, 2011.

[7] S. Sundarajan, R. Murugan, A. S. Nair, and S. Ramakrishna, "Fabrication of P3HT/PCBM solar cloth by electrospinning technique," *Materials Letters*, vol. 64, no. 21, pp. 2369–2372, 2010.

[8] J. Kim, W. Chung, K. Kim et al., "Performance optimization of polymer solar cells using electrostatically sprayed photoactive layers," *Advanced Functional Materials*, vol. 20, no. 20, pp. 3538–3546, 2010.

[9] Y. J. Hsiao, T. H. Fang, L. W. Ji, Y. C. Lee, and B. T. Dai, "Size effect of nanodiamonds on P3HT:PCBM heterojunction solar cells," *Electrochemistry Communications*, vol. 18, no. 1, pp. 4–7, 2012.

[10] Y. Hsiao, T. Fang, L. Ji, Y. Lee, and B. Dai, "Nanodiamonds embedded in P3HT:PCBM for enhancing efficiency and reliability of hybrid photovoltaics," *Electrochemical and Solid-State Letters*, vol. 15, no. 4, pp. K27–K30, 2012.

[11] F. Wang, Z. Chen, L. Xiao, B. Qu, and Q. Gong, "Enhancement of the power conversion efficiency by expanding the absorption spectrum with fluorescence layers," *Optics Express*, vol. 19, no. S3, pp. A361–A368, 2011.

[12] V. Kruefu, E. Peterson, C. Khantha, C. Siriwong, S. Phanichphant, and D. L. Carroll, "Flame-made niobium doped zinc oxide nanoparticles in bulk heterojunction solar cells," *Applied Physics Letters*, vol. 97, no. 5, Article ID 053302, 2010.

[13] Z. W. Chiu, Y. J. Hsiao, T. H. Fang, and L. W. Ji, "Morphology and optical performance of graphene-doped organic photovoltaic cells," *Microsystem Technologies*, vol. 19, pp. 1781–1785, 2013.

[14] S. H. Wang, Y. J. Hsiao, T. H. Fang, M. H. Lin, and S. H. Kang, "Enhancing performance and nanomechanical properties of carbon nanotube doped P3HT:PCBM solar cells," *ECS Journal of Solid State Science and Technology*, vol. 2, no. 11, pp. M52–M55, 2013.

[15] E. Voroshazi, B. Verreet, T. Aernouts, and P. Heremans, "Long-term operational lifetime and degradation analysis of P3HT:PCBM photovoltaic cells," *Solar Energy Materials and Solar Cells*, vol. 95, no. 5, pp. 1303–1307, 2011.

Research Article

Using Pre-TMIn Treatment to Improve the Optical Properties of Green Light Emitting Diodes

Bing Xu,^{1,2} Hai Tao Dai,¹ Shu Guo Wang,¹ Fu-Chuan Chu,² Chou-Hsiung Huang,² Sheng-Fu Yu,³ Jun Liang Zhao,⁴ Xiao Wei Sun,⁵ and Ray-Ming Lin²

¹ Tianjin Key Laboratory of Low Dimensional Materials Physics and Preparing Technology, School of Science, Tianjin University, Tianjin 300072, China

² Graduate Institute of Electronic Engineering and Green Technology Research Center, Chang Gung University, Taoyuan 333, Taiwan

³ Institute of Microelectronics and Department of Electrical Engineering, Center for Micro/Nano Science and Technology, Advanced Optoelectronic Technology Center, National Cheng Kung University, Tainan 70101, Taiwan

⁴ Shanghai Juntech Co. Ltd., 1378 Xingxian Road, Shanghai 201815, China

⁵ Centre of Excellence for Semiconductor Lighting and Displays, School of Electrical and Electronic Engineering, Nanyang Technological University, 50 Nanyang Avenue, Singapore 639798

Correspondence should be addressed to Ray-Ming Lin; rmlin@mail.cgu.edu.tw

Received 16 April 2014; Revised 6 June 2014; Accepted 24 June 2014; Published 10 July 2014

Academic Editor: Sheng-Po Chang

Copyright © 2014 Bing Xu et al. This is an open access article distributed under the Creative Commons Attribution License, which permits unrestricted use, distribution, and reproduction in any medium, provided the original work is properly cited.

We investigated the effects of pre-TMIn treatment on the optical properties of green light emitting diodes (LEDs). Although pre-TMIn treatment did not affect the epitaxial structure of quantum wells, it significantly improved the quality of the surface morphology relative to that of the untreated sample. Indium cluster can be seen by high-resolution transmission electron microscopy (HR-TEM), which is the explanation for the red-shift of photoluminescence (PL). Time-resolved photoluminescence measurements indicated that the sample prepared with pre-TMIn treatment had a shorter radiative decay time. As a result, the light output power of the treated green LED was higher than that of the conventional untreated one. Thus, pre-TMIn treatment appears to be a simple and efficient means of improving the performance of green LEDs.

1. Introduction

Group III-nitride materials have attracted much interest for their use in optoelectronic applications because their emission spectra cover a wide range from the infrared to the deep ultraviolet [1–3]. Among them, indium gallium nitride (InGaN) is the most promising material for the preparation of high-efficiency, high-power light emitting diodes (LEDs), which are employed widely in backlighting, traffic lights, headlights, and general illumination [4]. Although InGaN-based blue LEDs are well established, the InGaN-based green LEDs continue to suffer from low efficiency, which limits their further applications in white lighting devices.

V-shaped defects [5–7] readily form at InGaN/GaN quantum wells (QWs) having high indium mole fractions, triggered by threading dislocations in the buffer layer. Several

factors can lead to a low-quality InGaN layer, including lattice mismatch between InN and GaN [8], low miscibility of InN [9, 10], phase separation [11], indium surface segregation [12], and V-shaped defects [5–7]. A growth interruption technique [13, 14] can be used to improve the quality of InGaN layers and to enhance the luminescence intensity of LED devices. By applying growth interruption at a high growth temperature, the atoms in the InGaN layer can migrate to their minimum energy sites to approach thermal equilibrium and decomposition of In-rich regions, leading to a flat InGaN surface. Another growth method in which trimethylindium (TMIn) is employed during the growth interruption process is known as “TMIn treatment” [15]; it can suppress InGaN decomposition and indium aggregation to achieve a more homogeneous indium composition, a lower density of V-shaped defects, higher energy states, stronger photoluminescence intensity,

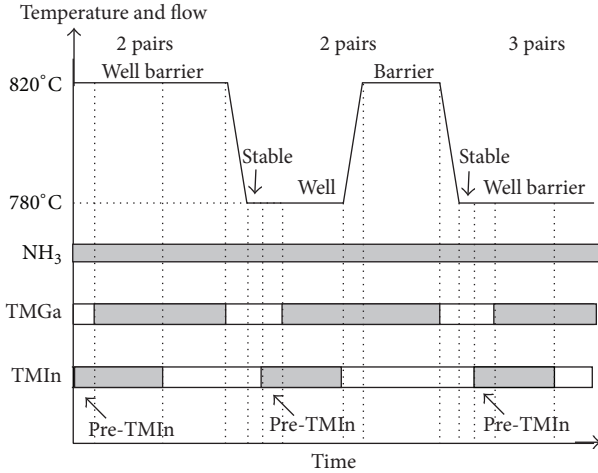


FIGURE 1: Growth conditions for pre-TMIn treatment in InGaN/GaN MQW.

and shorter decay times. In this study, we examined the effects of pre-TMIn treatment prior to QW growth on the output power of InGaN-based green LEDs. Our experimental results revealed that the light output intensity from a sample subjected to pre-TMIn treatment exceeded that of conventional LEDs at a quite high injection level, a result of stronger quantum confinement ability arising from indium-rich sites. Time-resolved photoluminescence (TRPL) revealed that the radiative recombination effect of the TMIn-treated sample was better than that of its untreated counterpart.

2. Experimental Methods

InGaN/GaN multiple quantum well (MQW) samples were grown on a (0001) sapphire substrate using an atmospheric pressure metal-organic chemical vapor deposition system. Trimethylgallium, trimethylindium, trimethylaluminum, and ammonia (NH_3) are used as precursors of the Ga, In, Al, and N atoms, respectively. Bicyclopentadienyl and silane are used as the p- and n-type dopant precursors. The substrates were first heated in H_2 ambient to remove any contaminants prior to performing the growth process. The LED structures comprised a 25 nm low-temperature GaN nucleation layer; a 1 μm unintentionally doped GaN buffer layer; a 3 μm n-GaN layer; seven periods of MQW layers featuring 2.7 nm InGaN well layers and 8 nm GaN barrier layers; a 10 nm AlGaIn electron blocking layer; and a 100 nm p-GaN layer. There are two samples which are without and with pre-TMIn flow and each sample has three sets of MQW layers. The detail of pre-TMIn flow condition is (i) two pairs of InGaN QWs and GaN barriers grown at 820°C with a TMIn preflow temperature of 820°C; (ii) three pairs of InGaN QWs and GaN barriers grown at 780 and 820°C, respectively, with a TMIn preflow temperature of 780°C; and (iii) three pairs of InGaN QWs and GaN barriers grown at 780°C with a TMIn preflow temperature of 780°C. Before the deposition of the InGaN QW layers, only TMIn and NH_3 were flowed into the reactor. For easy understanding, the details are schematically

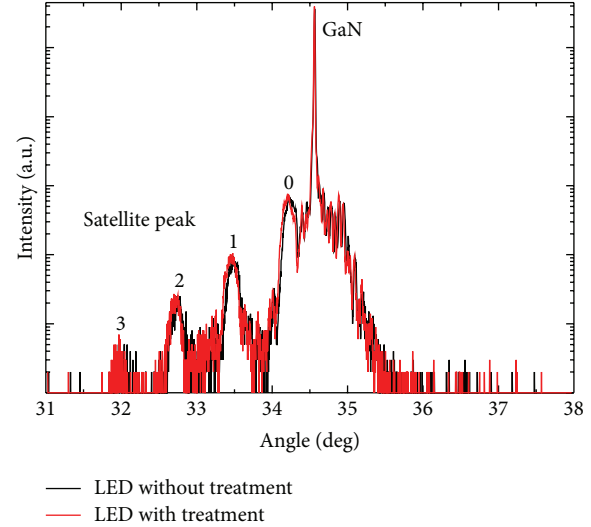


FIGURE 2: XRD spectra for the LEDs prepared with and without TMIn treatment.

represented in Figure 1. The final LEDs were fabricated, by means of standard LED process technology, to have an active area of $1 \times 1 \text{ mm}^2$.

The epitaxial wafers were subjected to analysis through high-resolution X-ray diffraction (HR-XRD), high-resolution transmission electron microscopy (HR-TEM), atomic force microscopy (AFM), TRPL, and room-temperature photoluminescence; the light output power was measured to characterize the optical properties of the LED devices.

3. Results and Discussion

Figure 2 displays the HR-XRD spectra of the LEDs prepared with and without pre-TMIn treatment. The diffraction peak of GaN is identified and marked in the curve; it arose from the buffer and the n- and p-type contact layers. We used Vegard's law to calculate the indium composition from the lattice parameters determined through XRD. The XRD curves of the two samples are almost identical, implying that the structure of the MQWs did not change as a result of TMIn treatment, except for a slight increase in the indium content in the InGaN layer. The indium compositions are 24.5% and 25% for the samples without and with pre-TMIn treatment, respectively. The satellite peaks suggested good quality interfaces for the MQW structures. Our results confirm that indium diffusion into the barrier could be suppressed and that the indium composition became homogeneous after TMIn treatment [15].

We used AFM and SEM to observe the surface morphologies of the two samples (Figure 3). The surface morphology of the sample that had experienced pre-TMIn treatment was better than that of the untreated sample, with the root-mean-square (RMS) surface roughness observed decreasing from 0.819 to 0.708 nm. Figures 3(c) and 3(d) show the surface morphology of InGaN QWs layer etched by phosphoric acid (H_3PO_4) for 30 s at 220°C. The etch pits density is about $1.1 \times 10^9 \text{ cm}^{-2}$ and $7.3 \times 10^8 \text{ cm}^{-2}$ for the sample without and

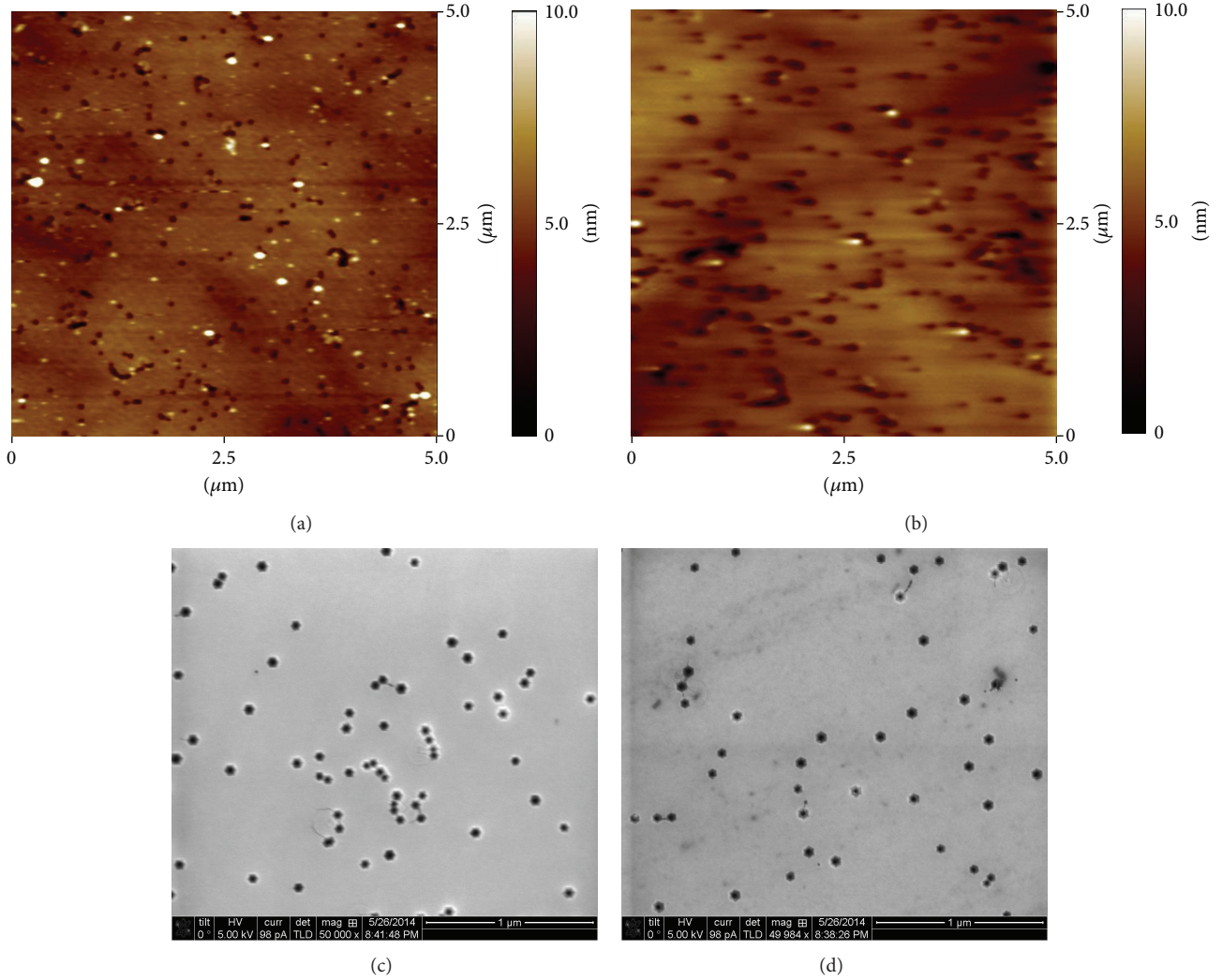


FIGURE 3: AFM and SEM images of the surface morphologies of the (a), (c) sample without TMIn treatment and (b), (d) sample with TMIn treatment.

with TMIn treatment, respectively. This finding suggested that TMIn treatment could improve the quality of the InGaN-GaN interface, thereby potentially improving the optical properties of green LEDs.

We used room-temperature photoluminescence to determine the center wavelengths of the two samples; Figure 4 displays their spectra. Photoluminescence peaks for the untreated and treated samples appeared at 520 and 535 nm, respectively; that is, a red-shift in the signal occurred after TMIn treatment. In general, such a red-shift occurs upon increasing the mole fraction of indium. Our XRD profiles in Figure 2 reveal, however, that the indium content increased only slightly. Considering the material properties of indium, we believe that the red-shift was related to aggregation of indium atoms in the QW during TMIn treatment [15, 16]. The action of TMIn and NH_3 could not form a continuous InN film, but rather InN islands, during the short treatment time and under the high growth temperature. In order to prove our thought, HR-TEM measurement was employed. Figure 5 presents the cross section HR-TEM images for two samples

(a) without TMIn treatment, (b) with TMIn treatment. From Figures 5(a) and 5(b), the barriers and wells can be easily distinguished. As we can see, the dark dots in Figure 5(b) are much more than in Figure 5(a). These dark points are In-rich cluster and their formation can be explained by pre-TMIn flow treatment, which is the main reason for the red-shift of PL.

We employed TRPL to examine the recombination rate of green LEDs that had been prepared with pre-TMIn treatment. We fitted the PL decay profiles in Figure 6 with the following double-exponential equation to obtain the decay time:

$$I(t) = A_1 \exp\left(-\frac{t}{\tau_r}\right) + A_2 \exp\left(-\frac{t}{\tau_{nr}}\right), \quad (1)$$

where $I(t)$ is the PL intensity, A_1 and A_2 are the decay parameters, and τ_r and τ_{nr} are the decay times for radiative and nonradiative recombination [17]. For the treated sample, the values of τ_r and τ_{nr} were 6.2×10^{-12} and 3.6×10^{-9} s, respectively; for the untreated sample, they were 9.1×10^{-12}

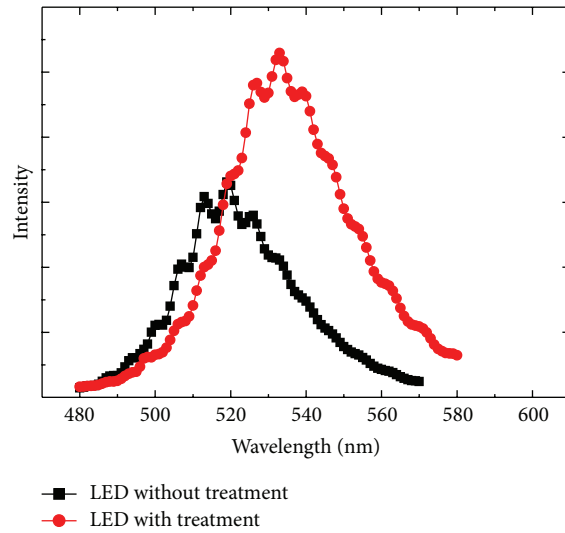


FIGURE 4: Room-temperature photoluminescence spectra for the LEDs prepared without and with TMIn treatment, with central peaks located at 520 and 535 nm, respectively.

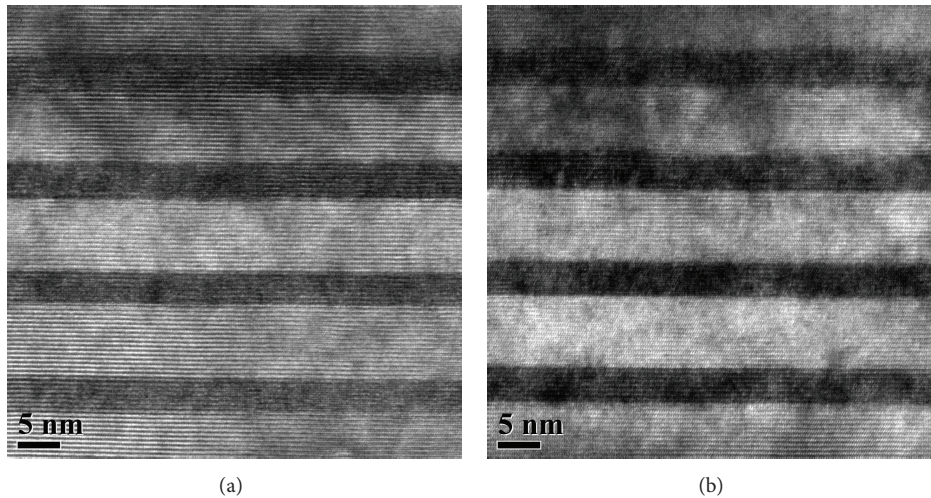


FIGURE 5: HR-TEM images of MQWs for two samples, (a) without TMIn treatment and (b) with TMIn treatment.

and 3.4×10^{-9} s, respectively. Thus, the radiative decay time decreased as a result of pre-TMIn treatment, leading to a greater radiative recombination effect. Because carrier transport into weakly localized states requires a certain energy to overcome a potential barrier, it is more difficult for carriers to transfer into weakly localized states [17, 18]. In the localized exciton model, trap centers are originated from a spatial disorder such as the fluctuation of indium within InGaN/GaN MQWs. Using TMIn treatment, the decay time becomes shorter, because treatment leads to more strongly localized states due to the indium cluster [18].

Figure 7 plots the light output power (L) and the voltage (V) with respect to the injection current (I) for the pre-TMIn-treated and untreated LEDs. The treated sample exhibited higher output power throughout the whole injection current density. At an injection current of 350 mA, the light output

power of the treated LED was 59% higher than that of the untreated LED and the forward voltages are 3.66 and 3.68 V for the samples without and with pre-TMIn treatment. We attribute this enhancement in light output power to the presence of In-rich clusters in the pre-TMIn-treated sample; these clusters could confine electrons and holes efficiently. As a result, indium treatment plays an important role in improving the luminescence of green LEDs.

4. Conclusion

Pre-TMIn treatment of the InGaN layer appears to be an efficient means of improving the luminescence performance of an InGaN green LED because it leads to a smoother surface and a shorter radiative decay time. XRD revealed that pre-TMIn treatment did not change the structure of the

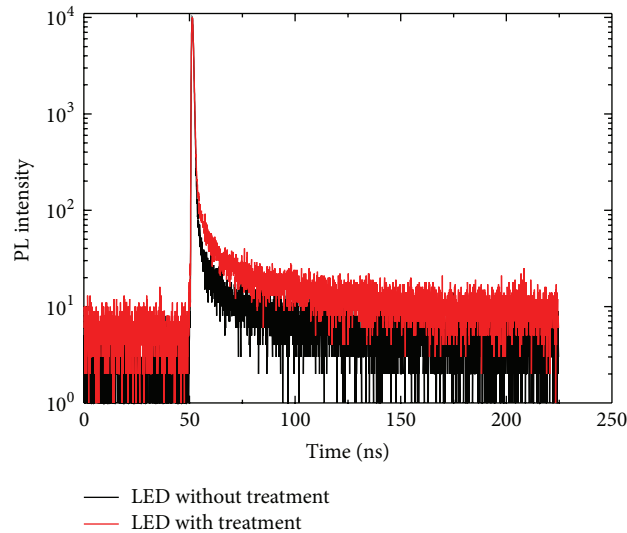


FIGURE 6: Time-resolved photoluminescence decay profiles of the LEDs prepared with and without TMIn treatment.

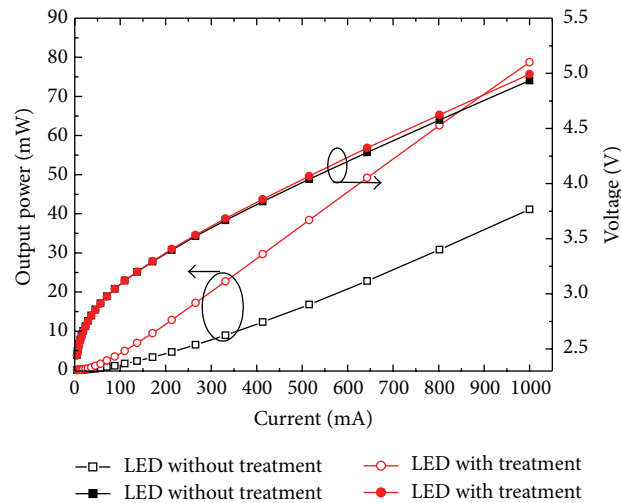


FIGURE 7: Plots of light output power and forward voltage with respect to injection current for the LEDs prepared with and without TMIn treatment.

MQWs and only slightly increased the indium concentration. Photoluminescence spectra of the treated sample featured a red-shifted peak wavelength, due to enhancement of the indium-cluster, which can be seen by HR-TEM. In addition, the light output power improved significantly when the LED was prepared with pre-TMIn treatment of the InGaN layer.

Conflict of Interests

The authors declare that there is no conflict of interests regarding the publication of this paper.

Acknowledgments

This study was supported by the National Natural Science Foundation of China (NSFC; Project nos. 61177061, 61177014, and 61076015), the Tianjin Natural Science Foundation (Project nos. 11JCZDJC21900 and 11JCYBJC25800),

the Research Fund for the Doctoral Program of Higher Education of China (New Teacher) (under Grant no. 20110032120070), the Special Foundation for Nanotechnology of the Shanghai Committee for Science and Technology (no. 11nm0501500), the Shanghai Pujiang Program (no. 12PJ1431000), and the Open Project Program of State Key Laboratory of Precision Measuring Technology and Instruments (Tianjin University).

References

- [1] S. C. Jain, M. Willander, J. Narayan, and R. van Overstraeten, "III-nitrides: growth, characterization, and properties," *Journal of Applied Physics*, vol. 87, no. 3, pp. 965–1006, 2000.
- [2] S. Nakamura, M. Senoh, S. Nagahame et al., "InGaN/GaN/AlGaIn-based laser diodes with modulation-doped strained-layer superlattices," *Japanese Journal of Applied Physics*, vol. 36, no. 12, pp. L1568–L1571, 1997.

- [3] R. M. Lin, M. J. Lai, L. B. Chang, C. H. Huang, and C. H. Chen, "Effect of trapezoidal-shaped well on efficiency droop in InGaN-based double-heterostructure light-emitting diodes," *International Journal of Photoenergy*, vol. 2012, Article ID 917159, 5 pages, 2012.
- [4] T. Erdem, S. Nizamoglu, X. W. Sun, and H. V. Demir, "A photometric investigation of ultra-efficient LEDs with high color rendering index and high luminous efficacy employing nanocrystal quantum dot luminophores," *Optics Express*, vol. 18, no. 1, pp. 340–347, 2010.
- [5] T. Hino, S. Tomiya, T. Miyajima, K. Yanashima, S. Hashimoto, and M. Ikeda, "Characterization of threading dislocations in GaN epitaxial layers," *Applied Physics Letters*, vol. 76, no. 23, pp. 3421–3423, 2000.
- [6] S. F. Yu, S. P. Chang, S. J. Chang, R. M. Lin, H. H. Wu, and W. C. Hsu, "Characteristics of InGaN-based light-emitting diodes on patterned sapphire substrates with various pattern heights," *Journal of Nanomaterials*, vol. 2012, Article ID 346915, 6 pages, 2012.
- [7] H. Saijo, J. T. Hsu, R. C. Tu et al., "Mapping of multiple-quantum-well layers and structure of V defects in InGaN/GaN diodes," *Applied Physics Letters*, vol. 84, no. 13, pp. 2271–2273, 2004.
- [8] T. Takeuchi, C. Wetzel, S. Yamaguchi et al., "Determination of piezoelectric fields in strained GaInN quantum wells using the quantum-confined Stark effect," *Applied Physics Letters*, vol. 73, no. 12, pp. 1691–1693, 1998.
- [9] Y. Lin, K. Ma, C. Hsu et al., "Dependence of composition fluctuation on indium content in InGaN/GaN multiple quantum wells," *Applied Physics Letters*, vol. 77, no. 19, pp. 2988–2990, 2000.
- [10] S. F. Chichibu, A. Uedono, T. Onuma et al., "Origin of defect-insensitive emission probability in In-containing (Al,In,Ga)N alloy semiconductors," *Nature Materials*, vol. 5, no. 10, pp. 810–816, 2006.
- [11] Y. Narukawa, Y. Kawakami, M. Funato, S. Fujita, and S. Nakamura, "Role of self-formed InGaN quantum dots for exciton localization in the purple laser diode emitting at 420 nm," *Applied Physics Letters*, vol. 70, no. 8, pp. 981–983, 1997.
- [12] H. K. Cho, J. Y. Lee, G. M. Yang, and C. S. Kim, "Formation mechanism of V defects in the InGaN/GaN multiple quantum wells grown on GaN layers with low threading dislocation density," *Applied Physics Letters*, vol. 79, no. 2, pp. 215–217, 2001.
- [13] S. Y. Kwon, H. J. Kim, H. Na et al., "Effect of growth interruption on In-rich InGaN/GaN single quantum well structures," *Physica Status Solidi (C)*, no. 7, pp. 2830–2833, 2003.
- [14] H. K. Cho, J. Y. Lee, N. Sharma, J. Humphreys, G. M. Yang, and C. S. Kim, "Structural and optical characteristics of InGaN/GaN multiple quantum wells with different growth interruption," *physica Status Solidi (b)*, vol. 228, no. 1, pp. 165–168, 2001.
- [15] M. Senthil Kumar, J. Y. Park, Y. S. Lee, S. J. Chung, C. Hong, and E. Suh, "Improved internal quantum efficiency of green emitting InGaN/GaN multiple quantum wells by in preflow for InGaN well growth," *Japanese Journal of Applied Physics*, vol. 47, no. 2, pp. 839–842, 2008.
- [16] S. Leem, M. H. Kim, J. Shin, Y. Choi, and J. Jeong, "The effects of in flow during growth interruption on the optical properties of InGaN multiple quantum wells grown by low pressure metalorganic chemical vapor deposition," *Japanese Journal of Applied Physics*, vol. 40, no. 2, pp. L371–L373, 2001.
- [17] Y. B. Tao, Z. Z. Chen, T. J. Yu et al., "Improvement of structural and luminescence properties in InGaN/GaN multiple quantum wells by symmetrical thin low temperature-GaN layers," *Journal of Crystal Growth*, vol. 318, no. 1, pp. 509–512, 2011.
- [18] S. Feng and J. Chyi, "Carrier transport study of TMIn-treated InGaN LEDs by using quantum efficiency and time-resolved electro-luminescence measurements," *Journal of the Electrochemical Society*, vol. 159, no. 3, pp. H225–H229, 2012.